Revista Brasileira de Ciências Mecânicas

4

REVISTA BRASILEIRA DE CIÊNCIAS MECÂNICAS
JOURNAL OF THE BRAZILIAN SOCIETY OF MECHANICAL SCIENCES

A REVISTA BRASILEIRA DE CIÊNCIAS MECÂNICAS
publica trabalhos que cobrem os vários aspectos da
ciência e da tecnologia em Engenharia Mecânica,
incluindo interfaces com as Engenharias Civil, Elétrica,
Química, Naval, Nuclear, Aeroespacial, Alimentos,
Agrícola, Petróleo, Materiais, etc., bem como aplicações
da Física e da Matemática à Mecânica.

Computational Aspects of Wing Vortex Wake Roll-Up

Renato S. Ribeiro
EMBRAER - Empresa Brasileira de Aeronáutica S.A.
12227-901 São José dos Campos, SP, Brazil

Abstract

The roll-up process of vortex wakes generated by wings (with a straight trailing edge) is computed, with the aid of two and three-dimensional vortex-in-cell methods. Results and computational effort of the two approaches are compared, and the accuracy of traditional assumptions made to allow the solution of the problem in the two-dimensional domain is investigated.
Keywords: Wing Vortex Roll-Up, Vortex-in-Cell Method

Introduction

The computation of wing-roll-up is of importance in several aircraft analysis problems, like canard-wing interference, induced downwash determination, and the interference suffered by an aircraft taking off shortly after another. Early attempts to solve the problem separated the wake in portions near and far from the wing, and adopted different simplifying assumptions for each region (Spreiter and Sacks, 1951). A widely studied two-dimensional model solves the problem in the Trefftz plane, using point vortices. This model, although simple, provides good insight into the wake roll-up dynamics. The inclusion of 3-d effects is essential when two or more lifting surfaces interact, or the influence of the wake shape in the wing circulation is important. Three-dimensional computations have largely used singularity and panel methods to represent wings and wakes. Sarpkaya (1989) and Hoeijmakers (1983) present a thorough review of 2-d and 3-d vortex methods applied to problems in fluid dynamics.

The vortex-in-cell methodology can improve the computational efficiency of 2-d and 3-d vortex methods. Its advantages are greater when a large number of singularities is used, since it reduces computational times and removes large scale instabilities. Therefore, vortex-in-cell methods are especially suitable for computation of detailed wake shapes.

This study applies 2-d and 3-d wake roll-up methods based in the vortex-in-cell approach to several wing geometries, in order to investigate some aspects of wing wake dynamics. These include the simplifying assumptions made in 2-d models, downwash distribution, and wing aspect-ratio effect.

Basic Equations and Numerical Method

Consider a wing in steady, low-subsonic flow. A coordinate system is attached to it, with the x axis aligned with the undisturbed flow velocity, U_∞, y placed along the span and z pointing upward. Lengths are made non-dimensional relative to the semi-span s, and velocities are relative to U_∞. For a thin wing at low angle of attack, the flow can be considered inviscid and incompressible, so that it respects the incompressible potential equation. Since the problem is linear, a solution can be obtained by the superposition of fundamental singular solutions, placed on the flow internal boundaries. The solutions chosen here are vortex points in two dimensions, and straight vortex segments in three dimensions.

As the wing generates lift, it creates behind it a thin sheet of vorcity, which can be modeled as a surface of discontinuity in potential. In a further simplification, the sheet is represented by a set of vortex lines that start at the trailing edge of the wing and proceed downstream towards infinity. The vortex theorems of Helmholtz and Kelvin state that free vortex lines embedded in potential flow move with the local velocity. This non-linear boundary condition ensures that the wing wake is not subjected to forces, and produces rolled-up wake shapes.

Three-Dimensional Formulation. The wing is represented by a network of vortex segments, i.e., a vortex lattice. The present method (Ribeiro, 1992; Ribeiro and Kroo, 1992) employs vortex rings in order to easily conserve total circulation. The boundary condition of zero normal flow is enforced at control points on the center of the wing vortex rings. The wake filaments are supposed to be initially straight and aligned with the direction of U_∞. The vortex-lattice solution for this starting geometry provides the wing and wake circulation distributions, which are kept fixed throughout the roll-up process. A sub-vortex technique creates additional vortices on the wake, filling the space between the vortex lines that originate at vortex ring segments. This technique distributes better the wake vorticity along the span, in preparation for the vortex-in-cell calculation. The wake vortex-segments are created so that their extremities, or nodes, lie in $x = $ const cross-flow planes. This is solely a choice of construction of the wake, not a restriction of the method. The wake is cut-off at a certain distance X_{cutoff} downstream of the wing.

After velocities are determined on the wake, a relaxation procedure changes the wake geometry, aligning its segments with the local flow velocity. If u_i^n indicates the velocity at the upstream node of a wake segment, and r_i^n its position, both at relaxation iteration n, the new position of the segment's downstream node is given by

$$r_{i+1}^n = r_i^n + \Delta\tau_i u_i^n \tag{1}$$

$$\Delta\tau_i = \Delta x / u_{xi}^n \tag{2}$$

Δx is the x distance between the wake cross-flow planes that maintains the wake nodes always at the same cross-flow planes. At each relaxation iteration, the vortex-in-cell method computes the velocities u_i^n induced by all the vortex segments on the wake nodes, and then all wake nodes are moved. The process is repeated until the maximum node displacement is smaller than a specified convergence factor.

The vortex-in-cell method solves the following vector Poisson equation:

$$\nabla^2\psi = -\omega \tag{3}$$

where ψ is the vector potential of the perturbation velocity field u, and is defined by $u = \nabla\times\psi$. Vorticity, ω, is defined by $\omega = \nabla\times u$. The method has basically three phases. First, a Cartesian mesh is superimposed over the wing and wake vortex network. The vorticity concentrated in the vortex segments is then distributed to the grid, so as to produce a discrete representation ω_{ijk} of the singular field, $\omega(x,y,z)$. The spreading of the vorticity in one segment is performed by applying a three-dimensional spreading function on all of its points. That generates a line integral, which can be approximated by Gauss-Legendre two-point quadratures. The spreading function is now applied to the portion of vorticity allocated to each quadrature point. The spreading function is assembled through the product of three one-dimensional functions. These are quadratic splines that span 3 grid-cell lengths in each Cartesian direction. A quadrature point distributes vorticity to the closest 27 grid-cells.

The second phase is the solution of the second-order discrete versions of the three scalar Poisson equations in (3). A Fast Poisson Solver, based on Fast Sine and Cosine Transforms, is used. A fast convolution procedure is introduced in order to satisfy the boundary condition of vanishing perturbations at infinity. The influence of a portion of the wake that extends beyond the computational box (i.e., $x > X_{cutoff}$) is taken into account by an artifice introduced in the convolution scheme. This artifice effectively doubles the wake length in the x direction for calculation purposes, with negligible increase in computational time. Velocities on grid points are computed from the solution ω_{ij} by second-order central finite-differences.

In the final phase, velocities at points of interest (wake segments nodes, in this case) are interpolated from grid point values. The interpolation procedure uses the same quadratic splines of the spreading scheme. The application of the vortex-in-cell method presents two basic advantages. The

effect of the spreading/interpolation procedure is analogous to the introduction of a viscous core for the vortex segments. The velocity singularity at the segment position is removed, and the effective core has a radius of about 1.5 grid-cell lengths. The second advantage appears when detailed descriptions of the wake are desired. The method has computational time of the order $M \log_2 M$, where M is the number of grid cells, while the interpolation and spreading schemes have times of the order of the number of vortex segments, N. Therefore, the N^2 dependence of traditional vortex methods is removed, and wakes with a large number of vortices can be computed much faster.

Two-Dimensional Formulation. The roll-up process of wing wakes can be simulated approximately by disregarding the wing influence and the wake curvature in the streamwise direction. Such hypotheses permit the representation of the discretized wake by straight, parallel infinite vortices, which move under their induced velocities. These velocities have components only in the yz plane and can be computed from a corresponding set of 2-d point vortices, in cross-flow planes of the wake. Although these simplifications are valid only at far distances downstream (i.e., at the Trefftz plane), a first approximation of the wake shape can be obtained by using the 2-d model as soon as the wake leaves the wing. In the 2-d limit, the x coordinate is identified with a pseudo-time variable t, so that $U\infty t$. When t is made non-dimensional relative to s/U_∞, one has simply $x = t$.
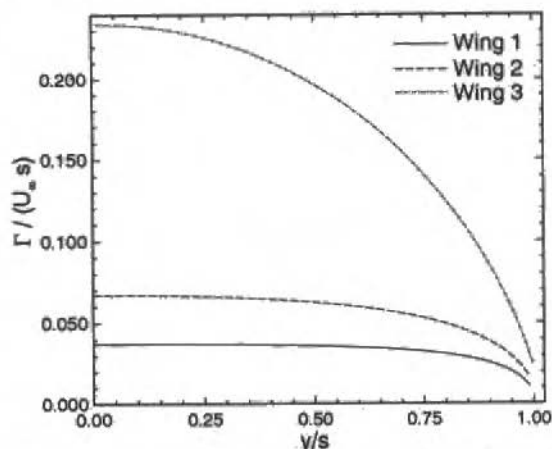
Fig. 1 Bound circulation distribution for the computed wings

The 2-d computation starts with the 3-d wake at the wing trailing-edge cross-flow, which provides the starting positions and the circulations for the 2-d point vortices. The wake roll-up method in 2-d is a pseudo-time integration, and a simple Euler scheme is employed here. In analogy to the 3-d relaxation scheme, the position of vortex i at time $(n + 1)\Delta t$ is given by

$$r_i^{n+1} = r_i^n + \Delta t \, u_i^n \tag{4}$$

r denotes now the position of a point vortex on the yz plane. The velocities u_i^n are computed by a 2-d version of the vortex-in-cell method described above, which solves the scalar Poisson equation given by

$$\nabla^2 \psi_x = -\omega_x \tag{5}$$

Observe that only the x components of vector potential and vorticity are needed. In fact, ψ_x is identified as the 2-d stream function in this case.

Results

Both wake roll-up methods were applied to three wings with decreasing aspect-ratio and no twist, all at 5° angle-of-attack. Wing 1 was rectangular and had aspect-ratio, AR, equal to 10. Wing 2 was also rectangular, and had AR = 5. Wing 3 was a delta wing with AR = 2. Figure 1 shows the circulation distribution for the three wings. The lift coefficient for Wings 1, 2 and 3 was 0.33, 0.28 and 0.18 respectively.

All 3-d wake roll-up computations used grid-cell lengths equal to $0.1 \times 0.04 \times 0.04$ for the vortex-in-cell method. The x-direction length of the wake segments, Δx, was equal to 0.1. All 2-d computations used the same grid-cell sizes for the y and z directions, and a pseudo-time increment (Δt) equal to 0.1, to maintain correspondence to the 3-d calculations. The wake length in the x direction was 5 wing spans ($X_{cutoff} = 10s$). In the 3-d case, the convergence factor for the wake was 0.05% of s. Symmetry was not explored in the computations, so that the whole wing and wake were modeled. The coordinate system origin was placed at the trailing edge of the root chord.

Wings 1 and 2 had 111 panels along the span, only one panel along the chord, and the wake was formed by 1000 vortex lines. Wing 3 had 102 panels along the span, 2 along the chord, and 919 vortices in the wake.

Fig. 2   Comparison of computed wake shapes for Wing 1

Fig. 3   Path of the 2-d center of gravity of vorticity for Wing 1

Fig. 4   Downwash distribution at the wing trailing edge for Wing 1

Fig. 5   Comparison of computed wake shapes for Wing 2

Fig. 6   Path of the 2-d center of gravity of vorticity for Wing 2
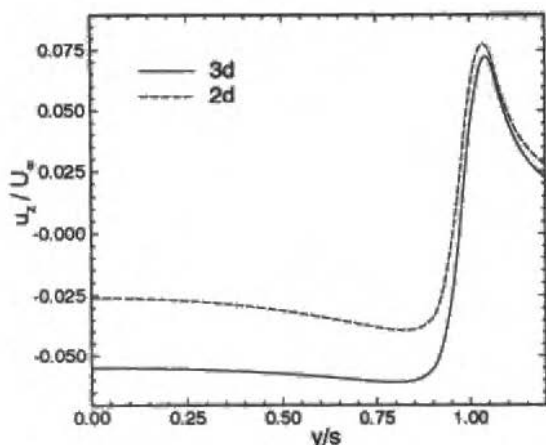
Fig. 7 Downwash distribution at the wing trailing edge for Wing 2

Observe in Fig. 2 that the wake shapes computed for Wing 1 by the 2-d and 3-d methods were practically identical for all cross-flow planes shown, except for small downward shifts for the 3-d wake. Figure 3 shows the position of the center of gravity of vorticity in the cross-flow planes. Notice that the y position of the c.g. remained essentially constant for both computations, in agreement with theoretical 2-d wake roll-up considerations (Spreiter and Sacks, 1951). The vertical position of the c.g. of the 3-d wake departed markedly from the 2-d wake position as soon as the wakes left the wing trailing edge. However, at a distance of about one span behind the wing, the downward shift had essentially reached a constant value. The reason for this difference in wake displacement close to the wing is illustrated in Figure 4, that shows downwash distributions at the wing trailing edge. The 3-d values were in average 4 times those of the 2-d calculation. This shows that, for this high-aspect wing, the decrease in downwash due to the removal of the wing effect is much larger than the increase due to the addition of the upstream semi-infinite wake extension in the 2-d formulation.
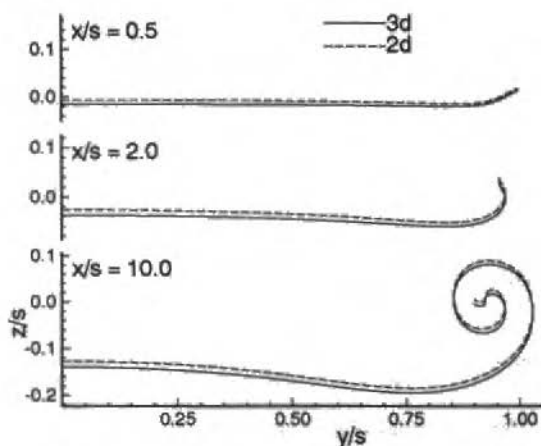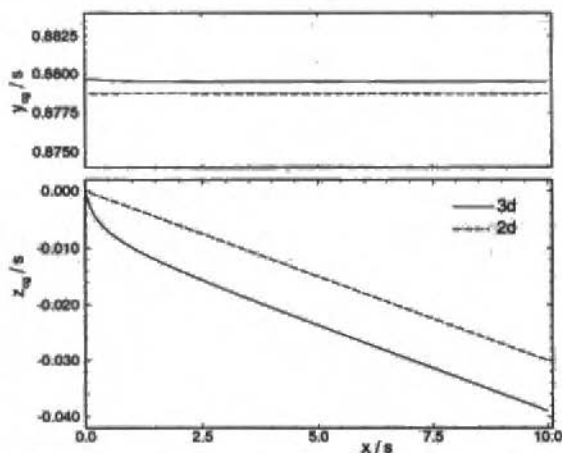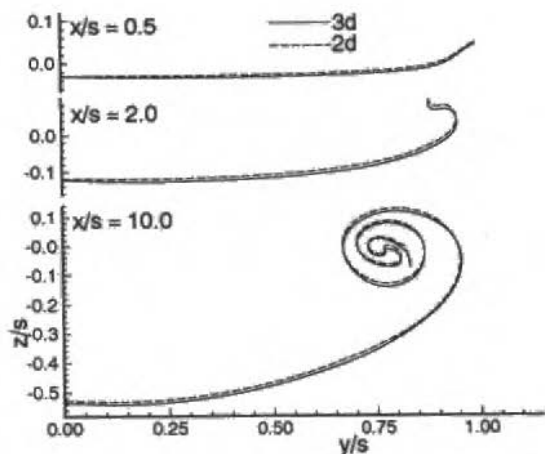

Fig. 8 Comparison of computed wake shapes for Wing 3
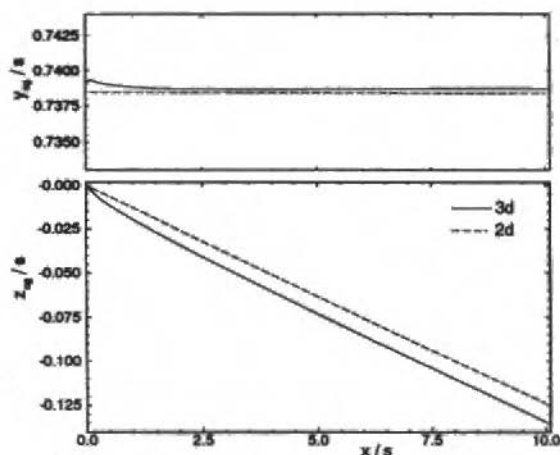
Fig. 9   Path of the 2-d center of gravity of vorticity for Wing 3

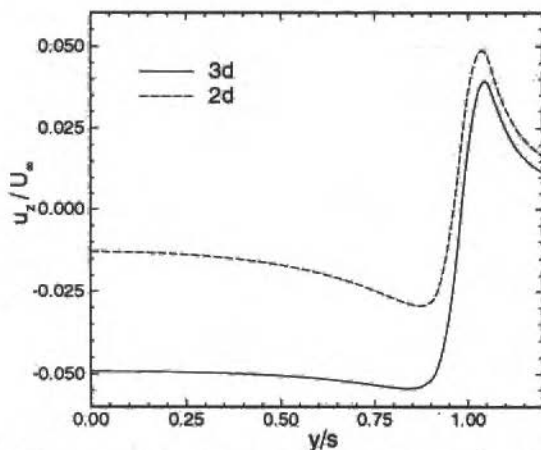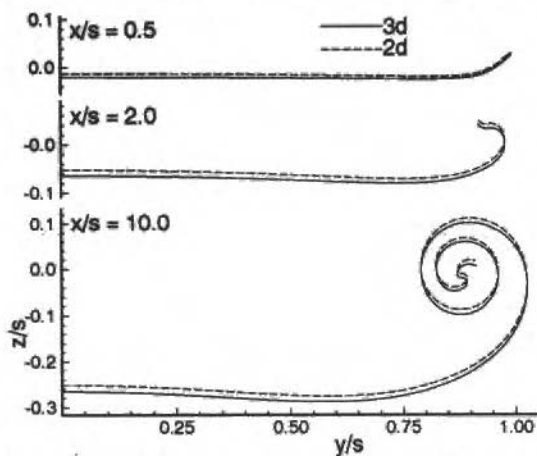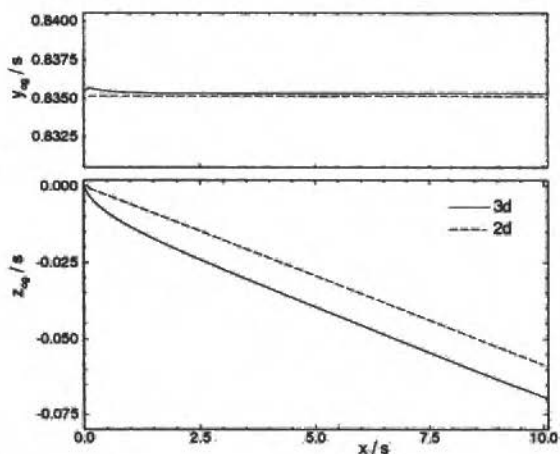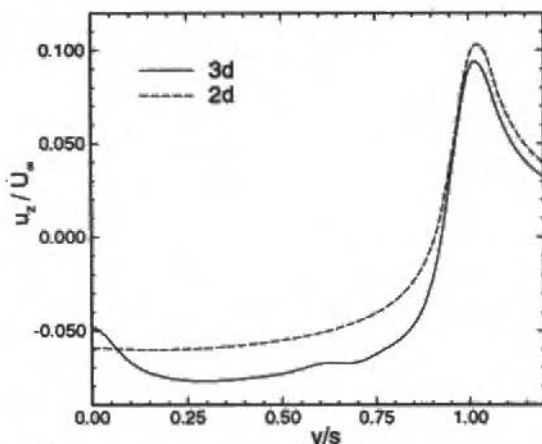Fig. 10   Downwash distribution at the wing trailing edge for Wing 3

Figures 5 to 10 show results for Wings 2 and 3. Notice the increasing degree of roll-up of the wakes, due to the higher circulation of the wake vortices. The same observations concerning wake shapes and vorticity c.g. position apply here. For Wing 2 (Fig. 7), the 3-d downwash values were still larger than the 2-d ones, but the difference decreased. The discrepancy in downwash magnitude decreased even further for Wing 3, but the distributions had differences in shape close to the wing root.

The last grid used by the 3-d vortex-in-cell method for Wing 3 had dimensions equal to 129 x 5 x 33. Wake convergence was reached after 203 relaxation iterations. The 3-d computation took 3.83 CPU hours in an IBM-RISC6000/340 workstation. In contrast, the 2-d computation used only 10 seconds.

Conclusions and Comments

The wake shapes computed by the 2-d and 3-d approaches were surprisingly similar. The 3-d wakes presented a downward shift due to the higher downwash in the proximity of the wing. However, as showed by the vertical position of the center of gravity of vorticity, the vertical shift remained essentially the same after about one span behind the trailing edge. The magnitude of this shift reached from 0.9 to 1.1% of the semi-span, where the higher values occurred for the wings with lower aspect

ratio. On the other hand, the horizontal position of the c.g. could be considered constant for both computations. Such small differences between the results of the two methods reaffirm the applicability of the 2-d approach for these wings with straight trailing edges. The speed of the 2-d method largely compensates for its inaccuracies, especially if one is interested in wake shapes at distances of more than one semi-span behind the trailing edge. This suggests that a 2-d roll-up method that includes 3-d effects, like the one by Nikolic et al. (1992), which takes into account the influence of the wing bound vorticity, should provide very accurate results for such wings. Further studies should investigate the case of wings with swept trailing edges.

Acknowledgement

References

Spreiter, J.R., and Sacks, A.H., 1951, "The Rolling Up of the Trailing Vortex Sheet and Its Effect on the Downwash Behind Wings," Journal of the Aeronautical Sciences, Vol. 18, pp. 2-32.
Sarpkaya, T., 1989, "Computational Methods with Vortices - The 1988 Freeman Scholar Lecture," Journal of Fluids Engineering, Vol. 111, .
Hoeijmakers, H.W.M., 1983, "Computational Vortex Flow Aerodynamics," AGARD CP-342.
Ribeiro, R.S., 1992, Analysis of Wing Wake Roll-Up Using a Vortex-in-Cell Method, Ph.D. Thesis, Stanford University, Stanford, CA, USA.
Ribeiro, R.S., and Kroo, I., 1992, "Vortex-in-Cell Analysis of Wing Wake Roll-Up," 10th AIAA Applied Aerodynamics Conference - A Collection of Technical Papers (AIAA Paper 92-2703), Palo Alto, CA, USA, pp. 753-763.
Nikolic, V. et al., 1992, "'WINGWAKE' - A Computational Model for Preliminary Assessment of Vortex Attenuation Schemes," AIAA Paper 92-4209, Washington, DC, USA.

Exergetic and Thermoeconomic Analysis of Industrial Processes in the Basque Country (Spain)

Santiago Baeza Aguado
José María Sala Lizarraga
Victor de La Peña Aranguren
Antonio José Mitre Ropero
Applied Thermodynamics Department
Universidad del País Vasco-Escuela Técnica Superior de Ingenieros Industriales
427 80 55 Bilbao-Spain

Abstract

There has been carried out a work consisting in the application of the System Theory and the Exergy Analysis Method, including Thermoeconomic Techniques, to the industrial processes in the Basque Country (Spain). In this analysis, the irreversibilities in each basic operation have been quantified and the energetic and exergetic efficiencies have been evaluated. The exergetic costs have been also calculated for every energy and material flow, as well as their corresponding economic costs. Besides, there is intended to value the effects on the consumption of energy and materials when new technologies are introduced.

The basic aims of this study are, on the one hand, to develop a system of strategic planning in the field of energetic technologies and, on the other hand, to define a strategy plan for equipments, processes, technologies and areas (industrial, services and residential sectors), consuming energy and/or materials, referred to the Basque Country as a framework. The above-mentioned study has been applied, as an example, to the green glass manufacturing area.

Keywords: Energetic Analysis, Thermoeconomic Analysis, Industrial Processes, Green Glass Manufacturing

Introduction

Efficiency on the use of energy is being constantly analysed. The depth of these studies is certainly variable by always aiming to evaluate the specific consumptions in the different processes and uses.

A few years ago, these analysis restricted their field to relate the useful energy at the output of an equipment with the energy supplied to it, in order to show the possible improvements to increase that quotient. Together with these studies, an idea is emerging and its development is becoming more and more necessary: the quality of the energy and the differentation of the energetic flows, not only because of its energetic content but also because of its exergetic content.

This other type of analysis, carried out from the view of the Second Principle of Thermodynamics, intends to evaluate with a greater scientific rigour the efficiency in the use of energy.

Objectives

Every year, since 1982, the Energy Department of the Basque Government picks up information about the consumptions of energy and raw materials in the more representative industrial areas, what affects in whole to 320 enterprises, 21 subsectors, 50 processes, 3,800 raw materials and 4,400 basic operations, involving 960 furnaces and 400 boilers. This informations, stored in suitable data bases, is the starting point of the project whose main lines are next presented.

This project has a double objective:

- To develop a system of strategic planning in the field of energetic technologies; and
- To define a strategy plan for equipments, processes, technologies and sectors consuming energy and/or raw materials, analysing the effects of introducing new systems and disposing, in

short term, of an specific methodology to follow the actual levels evolution.

There has been necessary, in order to reach this double aim, to develop a software package with a modular structure which allows to manage different tasks such as:

- Simple updating of auxiliary files concerning raw materials, energies, equipments, and so on;
- Homogeneous and integrated evaluation of selected processes, in such a way that different pointers can easily be obtained (i.e., mean efficiency of a basic operation, mean efficiency of a process, etc.);
- Quick estimation of the effect of innovation of equipments and processes on the consumptions of raw materials and energy as well as on the different efficiencies; and
- Inclusion of a system of graphic support consisting on tables and drawing which aid to systematize the results.

Methodology

There has been calculated, for each one of the 320 plants being analysed, the values of the energetic and exergetic efficiencies and the exergy destruction in every basic operation, as well as the energetic, exergetic and economic costs of the different flows. So, we have followed these steps:

Definition of the Logical Structure of the Plant. The structure of an industrial plant is shown as a series of blocks, each one representing a basic operation involving exchange flows of materials and energies and whose aim is the transformation of some functional products (Fuels) into others with a higher added-value (Products).

The relation between flows and basic operations is established through the incidence matrix, $A(n,m)$. The elements of such matrix, a_{ij}, come to $+1$ if flow j enters the basic operation i, to -1 if it leaves and to 0 if no physical relation exists between them.

Calculation of the Energy and Exergy of Each Flow. Starting from the data supplied by the inquests fulfilled every year for each plant, it is possible to get the values of the physical and chemical enthalpies, as well as the physical and chemical exergies of the different flows. The calculations are carried out according to the method of Szargut (1986).

Mass, energy and exergy balances. These balances consist on the establishment and the solving of the next system of matrix equations:

$$A \times M = 0 \tag{1}$$

$$A \times E = 0 \tag{2}$$

$$A \times B = D \tag{3}$$

where M, E and B are the column-vectors (dimension mx1) whose elements correspond to the mass, respectively, to the mass, energy and exergy of the different flows, and D is the column vector (dimension nx1) representing the exergy destructions.

The matrix Eqs. (1) and (2) are the basis of the method of traditional analysis. However, Eq. (3) allows the calculation of the diagnostic vector D, that is, the exergy destruction in each basic operation as a result of the irreversibilities.

Definition of Fuel-Product-Loss. Any industrial plant can be considered as a series of subsystems mutually related through mass, energy and exergy flows, aiming to reach a determined productive objective. Applying this functional analysis to each basic operation belonging to a given process, we define the fuel (F), products (P) and losses (L) through the equation

$$F - P = L + D = I \tag{4}$$

where D is already known and I represents the total irreversibilities.

Starting with the definition of F, P and L, the matrices A_F, A_P and A_L (dimension n x m) are built, what allows the determination of the fuel and product exergies for each basic operation.

Calculation of Efficiencies. Next step is to proceed to estimate the values of the energetic efficiencies (conventional values) and the exergetic efficiencies for each basic operation. So, we have referred to the operation i:

$$\eta_{bi} = \frac{P_i}{F_i} = 1 - \frac{I_i}{F_i}$$ (5)

If F_T means the total fuel used in the plant, and P_T refers the whole product, the efficiency of the plant will be

$$\eta_T = \frac{P_T}{F_T} = 1 - \frac{\Sigma I_i}{F_T}$$ (6)

Exergetic Costs of the Flows. The energy of any flow does not depend on the process followed to obtain that flow, but the exergy varies according with the process particularly followed. The exergy amount necessary to generate a determined flow is just its exergetic cost, B^*.

For each basic operation in an industrial plant, the following balance of exergetic costs is satisfied:

$$\sum_i^e B_i^* = \sum_j^s B_j^*$$ (7)

where e and s represent, respectively, the number of input and output flows. So, for the whole process (n basic operations) the next matrix equation comes true

$$A \times B^* = 0$$ (8)

Taking into account that the number of unknown quantities (m) is greater than that of the basic operations (n), m-n additional equations are required. Valero (1986) shows that these equations are obtained through the establishment of a series of proposals. Once the matrix B^* is known, the exergetic costs of the fuels (F^*) and products (P^*) are inmediatly found, since

$$F^* = A_F \times B^*$$ (9)

$$P^* = A_P \times B^*$$ (10)

Technological innovations and operational improvements. One of the objectives of this study is to evaluate the savings in materials and energies which are reached either when introducing improvements in the equipments involved in any basic operation or when incorporating technological innovations.

Thermoeconomics states that there is no equivalence between different basic operations irreversibilities. This means that, for a given operation, the greater the exergetic cost of the fuel is, the greater the repercussion on the fuel consumption are.

Thermoeconomics shows that when a basic operation i is modified so that its efficiency improves, the corresponding fuel saving (A_i) can be evaluated through the expression

$$A_i = K_{F_i}^* \cdot P_i \cdot \frac{\Delta\eta_{b_i}}{\eta_{b_i}^2} \tag{11}$$

where K_{F_i} is the exergetic cost of the fuel for that basic operation, P_i is the corresponding product, and $\Delta\eta_b$ represents the variation of the exergetic efficiency. The above expression is only valid when $\Delta\eta_b$ neither implies any modification in the rest of basic operations of the current process nor in the exergetic relations concerning possible recirculations.

For each industrial process there has been defined:

- The minimum exergy, that is, the exergy of the product;
- The ideal similar process. These ideal processes are established for the different physical-chemical transformations. In such processes all the lost energies are recoverable and there is no exergy destruction in the equipments;
- The theoretical technical process. The minimum exergy loss and destruction are viewed both in the process and the equipments; and
- The reference process. It corresponds to the equivalent industrial process performed with the highest efficiency among all those from which there is information in the different countries.

Economic Costs of the Flows. We have associated to each flow of an industrial process its economic cost, which represents the number of monetary units per second that are required to produce that flow. This value will be the result of two contributions, one of them coming from the monetary cost of the input exergy in the plant (fuel, electricity and materials) and the order one including the paying-off costs and the maintenance costs.

The economic balance for a whole process can be stated as the following matrix equation

$$(A \times \Pi) + Z = 0 \tag{12}$$

where A is the incidence matrix (already referred), Π is the matrix containing the economic costs of each flow, and Z represents the economic matrix concerning the paying-off an maintenance costs.

Application to the Glass Industry

Next we represent the results we got through the application of the above methodology to the glass industry, specifically to the green glass area.

Raw Materials and Productions. According with the available information corresponding to 1992, the amounts of raw materials consumed and green glass produced for that year are shown in the following table.

Table 1

Raw Material	t	kg/prod.t
Green sand	34,906	483.2
Felspar sand	7,046	97.5
NaOH	21,915	303.4
Sulphates	794	11.0
Dolomite	7,211	99.8
Gree glass fragments	9,685	134.1
Glass fragments	6,779	93.8
Recycled glass	7,200	99.7
Total	95,536	1,322.5
Production	72,239	

Flow Diagram. Eight basic operations have been considered in the production process as well as a whole of forty flows. Therefore, an incidence matrix of dimension 8 x 40. Figure 1 represents the flow diagram. There have supposed that main flow conditions at the output of each basic operation are the one corresponding to the input to next operation. Eight residuary heat flows have also been included (one for each basic operation).
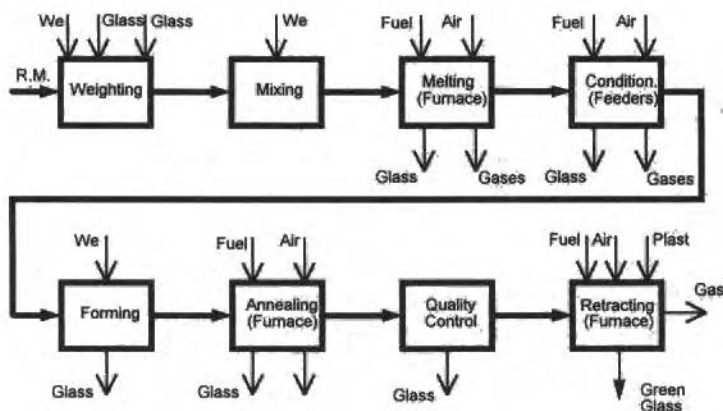
Fig. 1

Melting Model. A series of chemical reactions occur during melting in which different kind of silicates are formed. When producing these silicates, the solution of siliceous acid in excess begins as well as the mutual solution of the different silicates until the whole melting is reached.

The main chemical reactions which typify the melting operation in our reference process are the following:

$$Al_2O_3 + SiO_2 \rightarrow Al_2SiO_5$$
$$Fe_2O_3 + 2SiO_2 \rightarrow 2FeSiO_3 + \frac{1}{2}O_2$$
$$K_2O + SiO_2 \rightarrow K_2SiO_3$$
$$CaO + SiO_2 \rightarrow CaSiO_3 \qquad\qquad\qquad (13)$$
$$2NaOH + SiO_2 \rightarrow Na_2SiO_3 + H_2O$$
$$BaSO_4 + SiO_2 \rightarrow BaSiO_3 + SO_2 + \frac{1}{2}O_2$$
$$Na_2SO_4 + SiO_2 \rightarrow Na_2SiO_3 + SO_2 + \frac{1}{2}O_2$$
$$CaCO_3 + MgCO_3 + 2SiO_2 \rightarrow CaSiO_3 + MgSiO_3 + 2CO_2$$
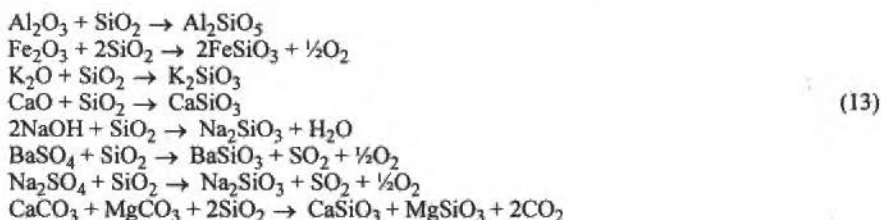
Thermodynamic Data. The values of the formation enthalpy are obtained from Perry (1992). With regard to the standard chemical exergy either we have referred to the values furnished by Szargut (1986) or we have directly proceeded to calculations when missing.

Mass, Energy and Exergy Balances. Table 2 shows the mass, energy and exergy of the different flows belonging to the reference process.

Table 2

Flow	Mass (t)	Energy (GJ)	Energy (GJ)
Raw materials (W)	78,651	16,102	45,514
Bottle gl. frag. (w)	9,685	4,146	2,934
Recycled glass (w)	7,200	3,082	2,178
Electricity		negligible	negligible
Electricity		negligible	negligible
Fuel (melting)	625	33,225	31,076
Air (melt.)	13,094	0	0

Flow	Mass (t)	Energy (GJ)	Energy (GJ)
Gases (melt.)	22,166	11,919	4,792
Glass frag. (melt.)	7,650	3,365	2,391
Fuel (cond.)	18	933	873
Air (cond.)	377	0	0
Gases (cond.)	395	212	85
Glass frag. (cond.)	negligible	negligible	negligible
Electricity		54,929	54,929
Glass frag. (form)	negligible	negligible	negligible
Fuel (anneal)	28	1,452	1,358
Air (ann.)	586	0	0
Gases (ann.)	614	330	133
Glass frag. (ann.)	negligible	negligible	negligible
Glass frag. (q.c.)	7,200	3,082	2,183
Fuel (retrac.)	3	197	184
Air (retrac)	63	0	0
Plastic (retrac.)	negligible	negligible	negligible
Gases (retrac.)	66	36	14
GREEN GLASS	72,239	30,918	21,897
Output-1 (weig)	95,536	23,330	50,626
Output-2 (mix)	95,536	24,233	50,626
Output-3 (melt.)	79,439	34,929	24,831
Output-4 (cond.)	79,439	34,929	24,831
Output-5 (form.)	79,439	34,040	24,095
Output-6 (ann.)	79,439	34,000	24,080
Output-7 (q.c.)	72,239	30,918	21,897
Heat Loss-3		7,245	5,992
Heat Loss-4		721	585
Heat Loss-5		55,818	34,282
Heat Loss-6		1,162	866
Heat Loss-8		161	negligible

Table 3 indicates the exergy destructions in each basic operation.

Table 3

Basic Operation	Exergy Destruction (GJ)
Weighing	0
Mixing	0
Melting	43,696
Conditioning	203
Forming	19,742
Annealing	374
Quality Control	0
Retracting	170

Energetic and Exergetic Efficiencies. Once the functional analysis has been performed and the Fuels and Products have been defined for each basic operation, the efficiencies can be calculated. Table 4 shows these values.

Table 4

Basic Operation	η_{en}	η_{ex}
Weighing	1	1
Mixing	1	1
Melting	0,723	0,341
Conditioning	0,993	0,991
Forming	0,382	0,305
Annealing	0,987	0,983
Quality Control	1	1
Retracting	0,995	0,993

As a consequence of the starting hypothesis, the operations of Weighing, Mixing and Quality Control turn to reach unitary efficiencies.

The lesser efficiency operations are Forming and Melting . Concerning the operation of Forming, that is due to the fact that in such an action the consumption of electricity coincides with the destruction of exergy, since all the electric power becomes lost heat, whose exergy is a part of the total losses, L. On the other hand, the low melting operation exergetic efficiency is a consequence of the important irreversibilities inherent to both the combustion and silicate formation reactions and, besides, to the heat transfer processes.

Exergetic Costs. By using the eight equations, resulted from the application of exergetic cost balance to each operation, and the additional thirty two relations, obtained through an exergetic cost assignment method based on Thermoeconomics, we can calculate the exergetic cost of each flow, as well as their unitary costs (see Table 5).

Table 5

Flow	Exergetic Cost (GJ)	Unit. Exergetic Cost	Economic Cost $(x10^{-6}$ ptas 1992)
Raw materials	41,312	1	538.9
Bottle frag. gl.	15,653	5.908	107.4
Electricity (w)	~0	~1	~0
Elect. (mix)	~0	~1	~0
Fuel (melting)	22,301	1	106,8
Fuel (cond.)	203	1	1.1
Elect. (form)	49,436	1	131,4
Fuel (ann.)	360	1	1,8
Fuel (retr.)	170	1	0,7
Plastic	~0	~0	~0
Output (weigh)	56,965	1.2954	646.3
Output (mix)	56,965	1.2954	646.3
Output (melt.)	79,266	3.5105	753.1
Output (cond.)	79,469	3.5195	754.2
Output (form.)	128,905	5.8832	885.6
Output (ann.)	129,265	5.9034	887.4
Output (q.c.)	129,265	5.9034	887.4
Output (retr.)	129,435	5.911	888.1

Table 5 makes clear that as we go ahead through the process, unitary exergetic cost becomes greater, since exergetic contribution to produce a determined flow is all the greater because the flow is more ahead in the process flow diagram.

So, as an example, the exergetic cost of the scrap glass in melting is about 4.54, whereas the exergetic cost of the scrap glass in the quality control turns to be 7.05. The unitary exergetic cost of the green glass (final product) is about 7.06, this is, to produce 1 kJ of exergy there has been necessary to use 7.06 kJ along the process.

Saving Measures and Technological Innovation. There has been also evaluated the effect on the Fuel consumption (energy and raw materials) derived from both the application of saving measures and technological innovations. Table 6 picks up the results obtained when improvements in basic operations lead to increases of the global exergetic efficiency of 3%, 5% and 9%.

Table 6

Basic Operation	K_i	$K_{Fi}P_i$ (GJ)	$\Delta\eta_{bi} = 3\%$	$\Delta\eta_{bi} = 5\%$	$\Delta\eta_{bi} = 9\%$
Weighing	1	92530,3	-	-	-
Mixing	1	92645,6	-	-	-
Melting	3	41105,2	10171,6	16075,3	28450,1
Conditioning	1,03	109753,0	2851,8	-	-
Forming	3,31	50140,4	15148,0	23848,8	41813,1
Annealing	1,06	159891,2	5661,7	-	-
Quality Control	1	170004,8	-	-	-
Retracting	1,01	153279	-	-	-

As it can be easily observed, for a given increase of the process energetic efficiency, the best result is reached when the improvement occurs in the operations of Melting, Annealing and Conditioning (in this order).

Flows Economic Costs. Economic cost of each flow has been estimated, just taking into account the monetary costs of the fuels, raw materials and electricity. This calculation has been performed in such a way since we have not been able to get any information on the money costs, maintenance costs and so on. Last column on Table 5 presents the values into 1992 pesetas.

Conclusions

There has been developed a useful implement for technological evaluation, making feasible different technological improvement in equipment, basic operations and processes possibilities assessment. We are in front of a system, open and integrated, which allows us to plan and establish global strategies in the field of the technological development.

Such a system is based on the use of the System Theory and the incorporation of both the Exergetic Analysis Method and the Thermoeconomics, what leads to the determination of exergetic efficiencies in basic operations as well as the estimation of exergetic and economic costs of the different flows taking part in each production process.

As an example, we have offered the results obtained when applying the above-explained methodology to the green glass industrial area. This application more outstanding points are:

- Greatest exergy destructions occur in melting operation (93,696 GJ) and Forming operation (21,062 GJ).
- Main flow unitary exergetic costs gradually increase in following basic operations (from a value of 1.83 in the first operation up to a value of 7.06 in last operation); and
- Green glass economic cost (without considering money and maintenance costs) goes up to 14.5 pts/kg (about 0.11 U.S. $/kg).

We can finally conclude that there has been developed a system being able to give priority to the basic directives concerning energetic innovation, raw materials and environment.

References

Kotas, T.J., 1985, "The Exergy Method of Thermal Plant Analysis", Butterworths, London.

Perry, R.H., et al., 1992, " Manual del Ingeniero Quimico", McGraw Hill, Mexico D.F.

Szargut, J., and Morris, D.R., 1986, "Standard Exergy of Some Elements of the Planet Earth", Energy, Vol. 11, pp 733-755.

Sala, J.M., 1987, "Termodinámica de Fluidos y el Método del Análisis Exergético", Servicio Editorial de la Universidad del País Vasco, Bilbao.

Tsatsaronis, G., 1987, "A Review of Exergoeconomic Methodologies. Second Law Analysis of Thermal Systems", ASME Book 100236, pp 81-87.

Tribus, M., and El-Sayed, Y.M., 1980, "Thermoeconomic Analysis of an Industrial Process", Center for Advanced Engineering Study, MIT.

Valero, A., Lozano, M.A.,and Muñoz, M., 1986, "A General Theory of Exergy Saving", ASME, WAM, AES-vol 2-3, pp 1-21.

Application of Comprehensive Simulation of Fluidized-Bed Reactors to the Pressurized Gasification of Biomass

Marcio L. de Souza-Santos
IPT - Instituto de Pesquisas Tecnológicas do Estado de São Paulo
Department of Mechanical Engineering, Group of Thermal Engineering
Av. Prof. Almeida Prado, C. Universitária, São Paulo, SP 05508-901, Brazil

Abstract

The first attempt to apply a previously developed computer program to simulate a pressurized fluidized-bed gasifier for wood is described. The experimental tests were reported by the Institute of Gas Technology (U.S.A.), which developed the process and the equipment. Among the overall and internal characteristics of the equipment operation obtained by simulation, the paper illustrates various aspects of temperature, composition, particle size distribution profiles throughout the bed and freeboard. The average deviations between these values are relatively small and allow the use of the program to call attention over possible improvements in the process.
Keywords: Fluidized-Bed Raactors , Biomass, Pressurized Gasification

Introduction

An increasing pressure toward the rational and environment minded use of biomass reserves for power generation has increased all over the world. Wood, forest and agriculture residues are the primary target for this utilization. In the particular case of Brazil, this application is even more pressing due to the exhaustion of the sources for hydroelectric generation.

High injection temperature and high efficiency gas turbine systems are the most attractive processes for that application. At the same time, the pressurized Fluidized-bed process is the most suitable process for the gas generation. Among other aspects, this is mainly due to its superior degree of controllability, lower rates of pollutant emissions (NO_x and Tar), high turn-down ratios, when compared to other processes.

Due to great amount of variables and parameters to be optimized for each specific application, the use of comprehensive simulation programs is a necessity.

The present mathematical model and simulation for Fluidized-Bed reactors were previously developed (de Souza-Santos, 1987, 1991) having in the mind that application. Although the program reproduced, within small deviations, data obtained from operations of boilers using bituminous and sub bituminous coals, no test was made for pressurized biomass gasification.

Due to the necessity of our work at IGT, the simulation program was improved, and greatly rewritten, to be able of simulating the RENUGAS pilot unit. The final objective was to use the program for process optimization and to help during the scaling-up to large industrial size units.

The Mathematical Model

The basic hypothesis and equation of the model can be found in de Souza-Santos (1987, 1981). The computer program has been improved to allow the application to carbonaceous and other particles with geometry other than spherical or near-spherical (de Souza-Santos, 1992).

As a first approximation, the production of hydrocarbons other than CH_4 and C_2H_6 were taken from the Tar fraction in the devolatilization process. Although these components do not represent a major part of the produced gas, some more work is needed here to improve the evaluation of their contribution.

The IGT Pilot Unit and Experimental Tests

The basic characteristics and input conditions for test T12-1 are presented in Evans et al. (1986) and reproduced here under the form required by the simulation program.

Table 1   Proximate analysis of the wood feeding

Fraction of the carbonaceous solid	Mass percentage (wet basis)
Moisture	4.94
Volatile	79.39
Fixed carbon	14.90
Ash	0.77
High Heat Value (Dry)	19.14 MJ/Kg

Table 2   Ultimate analysis of the wood feeding

Component of the carbonaceous solid	Mass fraction (dry basis)
C	0.4840
H	0.0631
O	0.4423
N	0.0021
S	0.0003
Ash	0.0082

Table 3   Other characteristics of the wood feeding

Property	Value
Bulk density of the carbonaceous solid	160 kg/m^3
Apparent density of the carbonaceous solid particle	720 kg/m^3
True density of the carbonaceous solid	1750 kg/m^3

Sand was used during the test to control the temperature and 130 kg was fed just once. Therefore, it is a batch operation regarding this solid. Its particle density was 3560 kg/m^3.

Table 4   Other conditions during test T12-1

Condition	Value
Mass flow of carbonaceous feeding	8.113E-2 kg/s
Mass flow of the O_2 + steam mixture injected near the bottom	4.033E-2 kg/s
Temperature of the O_2 + steam injected near bottom	
Composition of the O2 + steam injected near the bottom	

Component	Mass fraction (wet basis)
O_2	0,5102
H_2O	0,4898
Mass flow of steam injected just below the O_2 + steam injection point	2,946E-2 kg/s
Temperature of the steam	672K
Mass flow of nitrogen injected (a)	4,379E-2 kg/s
Pressure of gases injected into the bed	2,17E+6 Pa

(a): Nitrogen was used for sealing and, as a simplification, it has been assumed that all injection entered the bed at 0.381 m from the bed base.

Results

The experimental and simulation results are presented in the Tables 6 and 7. More properties of the produced gas are presented in Table 8.

Table 5   Basic geometry of the gasification unit

Dimension or condition	Value
Bed equivalent hydraulic diameter	0,292 m
Bed dynamic height	1,585 m
Freeboard equivalent hydraulic diameter	0,451 m
Position of thhe top of the freeboard (measured from he bed base)	6,147 m
Position of the carbonaceous solid feeding point (measured from the bed base)	0,381 m

Table 6   Composition (vol. %) of the produced gas from test T12-1

Components	Experimental	Simulation
CO_2	17,06	17,01
H_2O	35,82	35,91
CO	8,00	6,88
H_2	12,05	14,58
CH_4	7,37	5,68
N_2	19,18	19,37
H_2S	n.d.	0,53E-6
C_2H_4	0,03	0,03
C_2H_6	0,22	0,20
C_3H_8	0,00	0,42E-2
C_6H_6	0,27	0,11
SO_2	n.d.	0,55E-2
NO	n.d.	0,99E-7

n.d.: not determined or measured.

Table 7   Some conditions and parameters for test T12-1

Condition or parameter	Value	
	Experimental	Simulation
Total mass flow of produced gas	0,1843 kg/s	0.1837 kg/s
Mass flow of solid entrained at the top of freeboard	0,210E-4 kg/s	0.487E-3 Kg/S
Fluidization voidage (at the middle of the bed)	n.d.	0,886
Minimum fluidization velocity	n.d.	0.032 m/s
Superficial gas velocity (at the middle of the bed)	0,52 m/s	0.51 m/s
Average temperature at the middle of the bed	1105 K	1136 K
Circulation rate of carbonaceous particles (average)	n.d.	32.6 kg/m2/s

Table 7   Some conditions and parameters for test T12-1 (continued)

Circulation rate of inert particles (average)	n.d.	325.0 kg/m2/s
Average residence time of particles (based on the feeding rate)	n.d	1175 s
TDH (Transport Disengaging High)	n.d.	5.677 m
Mass of the bed	n.d.	95.3 kg
Stratic bed depth	n.d.	0.834 m
Pressure drop in the distributor	n.d.	12 Pa
Pressure drop in the bed	n.d.	6278 Pa
External wall temperature at the top of the bed	n.d.	360 K
External wall temperature at the top of the freeboard	n.d.	372 K
Percent of power input lost to external ambient	n.d	1.78%
Carbon conversion to gas	90.2 %	86,57 %
Combustion enthalpy of the produced gas (dry, clean, at 298K)	7.311 MJ/kg (a)	6.815 MJ/kg(b)

n.d.: not determined or measured or reported; (a) Calculated from the reported gas composition; (b) Carried with the produced gas stream.

Table 8   Some specific data, obtained by simulation, of the produced gas stream for test T12-1

Property or Condition	Value
Temperature	1089 K
Pressure (absolute)	2,164 MPa
Specific Heat	1884,2 J/kg/K
Density	5.449 kg/m^3
Viscosity	0,404E-4 kg/m/s
Thermal Conductivity	0,1104 W/m/K
Average Molecular Mass	22,74 kg/kmol
Density at standard condition (a)	1,017 kg/m^3
Volume flow	0,0337 m^3/s
Volume flow at standard condition (a)	0,1805 m^3/s
Adiabatic Flame Temperature in air (mixture originally at 298K)	1453 K
Adiabatic Flame Temperature in O_2 (mixture originally at 298 K)	2212 K

(a): 273.15 K, 101.325 kPa.

Discussion

The temperature profiles of the various phases in the bed and in the freeboard are presented in figs. 1 and 2. It should be noticed that the intermediate injection of cold (298 K) nitrogen provokes a sudden decrease in the bubble phase temperature. After that, the temperatures of all phases tend to a single value.
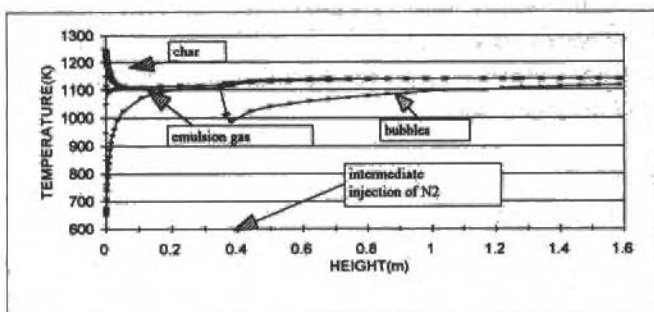
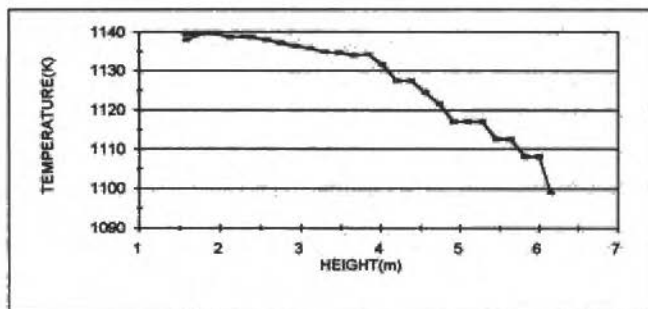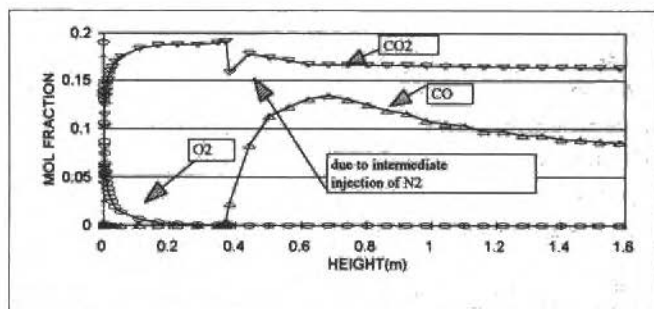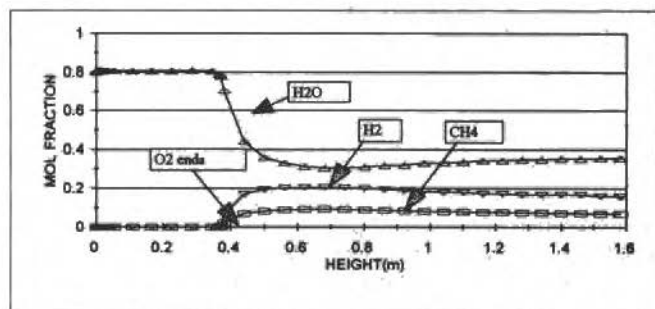Fig. 1   Temperature profiles in the bed

Fig. 2   Temperature profiles in the freeboard

Fig. 3   Concentration profiles of CO_2, CO, and O_2 in the emulsion

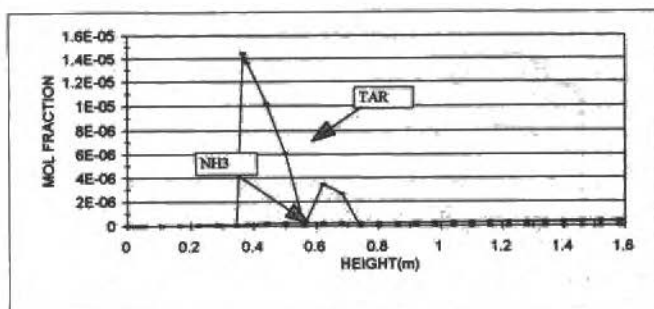Fig. 4   Concentration profiles of H_2O, H_2, and CH4 in the emulsion

Fig. 5 Concentration profiles of NH_3 and Tar in the emulsion

The most important concentration profiles of gases in the emulsion are presented in Figs. 3 to 5. The relative sudden decrease of Co_2 (Fig. 3) is mainly due to the intermediate injection of inert gas. Of course, no sealing gas will be used in the industrial size unit.

The decrease of H_2O, shown in Fig. 4, is due to the combined effects of intermediate injection of gas, devolatilization (wood feeding is made at 0.3 m) and the consumption by $C-H_2O$ reaction. Due to the relative high temperature of the bed, the fast devolatilization occurs near the wood feeding point, as shown in Fig. 5. Although the simulation shows that no tar can survive the cracking process - that takes place near the wood feeding point - during the experiments, some suspended liquid oil was observed in the gas stream leaving the freeboard. This may be caused by some degree of segregation of the lighter biomass particles from the average particles in the bed. The floating wood suffers devolatilization near the top of the bed. Therefore part of the released tar does not have sufficient residence time to be completely cracked.

Just as an illustration, the profiles of some gases in the bubble phase are presented in Fig. 6. The mass transfer between bubble and emulsion phases is exemplified by the CO Concentration profiles in those phases, as illustrated by Figs. 3 and 6. The expected much slower consumption of O2 in the bubble phase than in the emulsion can be observed. Therefore, it is necessary to provide enough space for complete transfer of oxygen from the bubbles to the emulsion. Added to that space, an extra bed height should be reserved to allow proper progress of the reducing reactions. The progress can be followed using the simulation which provides the profiles of the various gas components or by plotting the computed reaction rates. Of course, at the top of the freeboard, the compositions tend to those obtainable at the chemical equilibrium state at the exit temperature. On the other hand, the gas may leave the reactor before the equilibrium of all reactions is reached. The simulation can be used to verify these aspects.

The intermediate injection of gas led to the sudden increase on the superficial velocity and on the total void fraction, as shown in Fig. 7. Also, this leads to the sudden increases on the rates of particle circulations in the bed (Fig. 8).
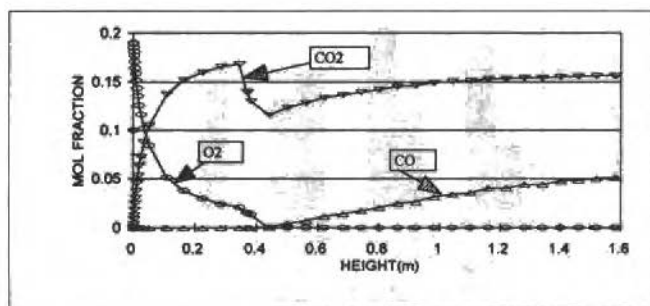

Fig. 6 Concentration profiles of CO_2, CO and O_2 in the bubble phase
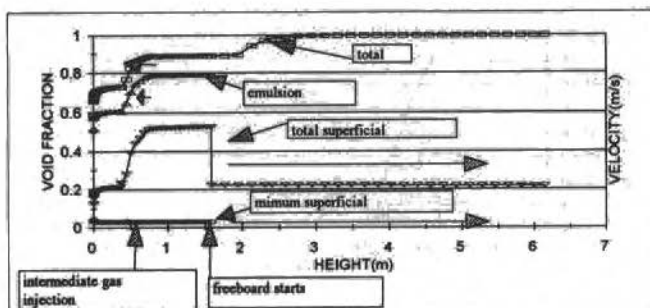
Fig. 7 Profile of void fractions and superficial velocities
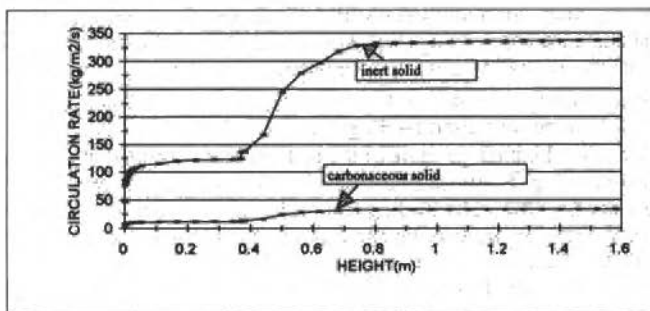

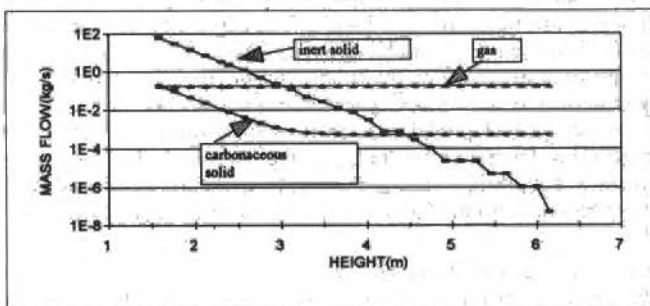Fig. 8 Profiles of circulations fluxes of particles in the bed

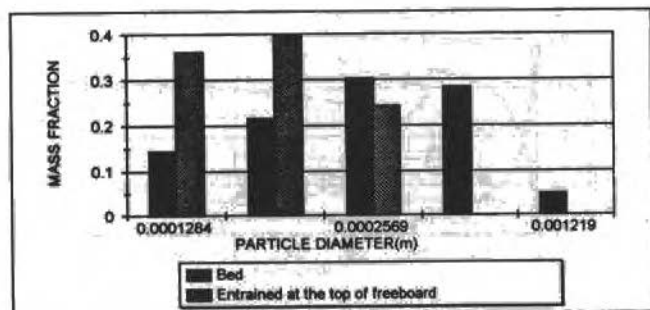Fig. 9 Mass flows of solid particles in the freeboard

Fig. 10 Particle size distributions of carbonaceous particles

Conclusions

As it could be verified, the simulation reproduced most of the important aspects of the experimental conditions within 5% deviations, specially for the total carbon conversion, produced gas composition, mass flow, and temperature.

Only a comprehensive simulation is capable of providing information on internal aspects of the process, for it can compute the average and individual phase composition and temperature profiles.

Additional work could be done regarding the stoichiometry of the tar decomposition to allow better predictions of some hydrocarbon productions. Also, some study should be carried on the rate of fine generation due to attrition of charcoal particles. This could improve the results of particle elutriation rates at the top of the freeboard.

Aside the underestimation of the elutriation rate, the simulation shows that some material should be continuously (or at intervals) withdrawn from the bed. Otherwise, the bed height would increase steadily. This may not constitute a problem for relatively short operation periods.

Despite these differences, the simulation is already useful to illustrate several aspects of the process and to indicate the path for improvements. For instance, the amount of injected steam, which caused relatively high concentrations of water in the produced gas, can be decreased. These excessive amounts were used to avoid temperatures above the ash softening point at the oxygen injection, which could lead to particle agglutination and bed collapsing due to loss of minimum fluidization conditions. A possible method to solve the problem could employ staged injections of oxygen. As the simulation computes the temperature of each solid and gas phase at all points of the system, the injection positions and conditions can be studied to avoid agglutinations. Once the objective is defined, the program can be used to find the best strategy, as well as to help during the search for an optimized design of an industrial size unit.

Acknowledgments

The author would like to express his gratitude to the colleagues Ronald Carty, Richard Knight, and Michael Onischak, for the information provided and interesting discussions during the work at IGT.

References

Evans, R.J., Knight, R.A., Onischak, M. and Babu, S.P., April 6-10, 1986, "Process and Environmental Assessment of the RENUGAS Process", Symposium on Energy from Biomass and Wastes X, Sponsored by Institute of Gas Technology, Washington, D.C., U.S.A.

de Souza-Santos, M.L., 1987, "Modeling and Simulation of Fluidized-Bed Boilers and Gasifiers for Carbonaceous Solids," Ph.D. Thesis, University of Sheffield, Sheffield, United Kingdom.

de Souza-Santos, M.L., 1989, "Comprehensive Modelling and Simulation of Fluidized Bed Boilers and Gasifiers," Fuel, Vol. 68, pp. 1507-1521.

de Souza-Santos, M.L., November 17-20, 1992, "Application of Comprehensive Simulation to Pressurized Fluidized-Bed Hydroretorting of Shale," 1992 Eastern Oil Shale Symposium, Lexington, Kentucky.

Escoamento Reativo em Desequilíbrio Químico através de Bocais Convergente-Divergente pelo Método das Características

Nonequilibrium Reactive Flows Through Convergent-Divergent Nozzle by the Method of Characteristics

José Eduardo Mautone Barros
Pedro Paglione
Universidade da Beira Interior - Portugal
Dordiane de Faria Alvim Filho
Instituto Tecnológico de Aeronáutica - Brasil

Abstract

A computational program to evalute nonequilibrium reactive flows of combustion products through convergent-divergent nozzle is developed. The basic assumptions are: two reactive systems [(H_2 and F_2) and H_2 and O_2)] and bidimensional flow. The results compare well to theorical and experimental data from the literature.
Keywords: Nonequilibrium Reactive Flows, Convergent-Divergent Nozzle, Method of Characteristics.

Resumo

Neste trabalho é apresentado um modelo para escoamento reativo em desequilíbrio químico através de bocais convergente-divergente.O método empregado para a solução numérica das equações é o método das características modificado para levar em conta os termos fontes resultantes da inclusão das reações químicas entre as espécies presentes. Consideraram-se dois sistemas reagentes H_2 e F_2 e H_2 e O_2, admitindo-se a hipótese bidimensional. Os resultados do programa computacional elaborado são comparados com outros trabalhos teóricos e experimentais mostrando uma boa concordância. São apresentadas também comparações entre o presente modelo e outros mais restritivos em termos de hipóteses.
Palavras-chave: Escoamento Reativo, Bocais Convergente-Divergente, Método das Características.

Introdução

Neste trabalho é estudado o escoamento reativo em desequilíbrio químico através de bocais convergente-divergente, visando coletar subsídios para um projeto ótimo destes bocais, os quais podem ser componentes de motores a jato (turboreatores, turbofans, estatoreatores e motores foguetes).

Procura-se aqui a implementação de modelos de escoamentos reativos bidimensionais, com a finalidade de prosseguir os trabalhos já realizados sobre a otimização do contorno destes bocais para a obtenção do empuxo máximo, onde o escoamento foi considerado congelado, Paglione et al. (1988), e onde o escoamento foi considerado em desequilíbrio químico unidimensional, Barros et al. (1990).

Utilizando-se as equações de conservação de massa e de energia e a equação da quantidade de movimento, estudou-se o comportamento dos produtos de combustão dos reagentes (H_2 e F_2) escoando através de um bocal, considerando-o, por hipótese, bidimensional. Compararam-se então os resultados obtidos com outros semelhantes encontrados na literatura, com a finalidade de validação do programa implementado. A seguir, analisou-se o sistema dos reagentes (H_2 e O_2), comparando-se os resultados com valores experimentais encontrados em Pavli et al. (1987), Smith et al. (1987), Kacynski et al. (1987).

Formulação Matemática do Problema

Conforme apresentado por Zucrow et al. (1977), o sistema de equações que descreve o escoamento reativo bidimensional em regime permanente é o seguinte:

$$\rho \frac{\partial u}{\partial x} + \rho \frac{\partial v}{\partial y} + u \frac{\partial \rho}{\partial x} + v \frac{\partial \rho}{\partial y} + \delta \rho v / y = 0 \tag{1}$$

$$\rho u \frac{\partial u}{\partial x} + \rho v \frac{\partial u}{\partial y} + \frac{\partial \rho}{\partial x} = 0 \tag{2}$$

$$\rho u \frac{\partial v}{\partial x} + \rho v \frac{\partial v}{\partial y} + \frac{\partial \rho}{\partial y} = 0 \tag{3}$$

$$u \frac{\partial p}{\partial x} + v \frac{\partial p}{\partial y} + - a_f^2 u \frac{\partial \rho}{\partial x} - a_f^2 v \frac{\partial \rho}{\partial y} = \psi \tag{4}$$

$$\rho u \frac{\partial C_i}{\partial x} + \rho v \frac{\partial C_i}{\partial y} = \sigma_i \; (i = 1,....,n) \tag{5}$$

Equações Características:

$$\left(\frac{dy}{dx}\right)_{o} = \lambda_o = \frac{v}{u} \quad \text{(Linha de corrente)} \tag{6}$$

$$\left(\frac{dy}{dx}\right)_{\pm} = \lambda_{\pm} = \tan(\theta \pm \alpha) \quad \text{(Linhas de Mach)} \tag{7}$$

Equações de Compatibilidade:

$$dp + \rho V dV = 0 \tag{8}$$

$$dp - a_f^2 d\rho = \frac{\psi}{u} dx \tag{9}$$

$$\rho u dC_i = \sigma_i dx \; (i=1,...,n) \tag{10}$$

$$\frac{\sqrt{M_f^2 - 1}}{\rho V^2} dp_{\pm} \pm d\theta_{\pm} + \left(\frac{\delta \sin\theta}{yM_f} - \frac{\psi}{\rho V^2 a_f}\right) \frac{dx_{\pm}}{\cos(\theta \pm \alpha)} = 0 \tag{11}$$

onde u e v são as componentes de velocidade nas direções x e y, respectivamente, ρ é a massa específica, C_i é a fração mássica da espécie química i, p é a pressão estática, x é a coordenada na direção paralela ao eixo do bocal, y é a coordenada radial do bocal, n é o número de espécies químicas envolvidas, λ são as inclinações das linhas características e (∘, +, -) indicam cada uma das três linhas características existentes. Os demais termos são definidos abaixo:

$$p = \rho t \sum_{i=1}^{n} C_i R_i \tag{12}$$

$$M_f = \frac{V}{a_f} = \text{número de Mach "congelado"} \tag{13}$$

$$a_f = \sqrt{\gamma_f R t} \tag{14}$$

$$\gamma_f = \frac{c_{pf}}{c_{pf - R}} \tag{15}$$

$$c_{pf} = \sum_{i=1}^{n} C_i c_{pi} \text{ ,onde } c_p \text{ é o calor específico do componente i} \tag{16}$$

$$R = \sum_{i=1}^{n} C_i R_i = \text{constante do gás} \tag{17}$$

onde R_i é a constante do gás para a espécie i.

$$\psi = \sum_{i=1}^{n} [\gamma_f R_i t - (\gamma_f - 1) h_i] \sigma_i \tag{18}$$

$$h_i = \int_{0}^{t} c_{pi} dt + h_i^{\circ} \tag{19}$$

onde h_i° é a energia de formação da espécie i por unidade de massa.

O termo σ_i é a função fonte da espécie i numa mistura de gases quimicamente reativa. Para esta mistura de gases, onde ocorrem simultaneamente várias reações, a equação geral da reação é:

$$\sum_{i=1}^{n} \upsilon_{ij} A_i \underset{k_{bj}}{\overset{k_{fj}}{\rightleftarrows}} \sum_{i=1}^{n} \upsilon_{ij}'' A_i \ (j=1,...m) \tag{20}$$

onde A_i é a espécie química i.

A partir da Eq. (20) e das leis de cinética química obtém-se a seguinte expressão:

$$\sigma_i = \overline{m}_i \sum_{j=1}^{m} \Delta \upsilon_{ij} \left[k_{fj} \prod_{i=1}^{n} \left(\frac{\rho C_i}{\overline{m}_i} \right)^{\upsilon'_{ij}} - k_{bj} \prod_{i=1}^{n} \left(\frac{\rho C_i}{\overline{m}_i} \right)^{\upsilon'_{ij}} \right] \tag{21}$$

onde K_{fj} e K_{bj} são as constantes das taxas de reação das equações químicas no sentido direto e inverso, m é o número de reações químicas do mecanismo cinético, $\overline{m}_j$ é o peso molecular da espécie i, υ'_i e υ''_i são os coeficientes estequiométricos da espécie i na reação j.

Para a solução do sistema acima apresentado (1 a 5) utilizou-se o método das características, o qual possibilita substituir este por um conjunto de equações características (6 e 7) e de compatibilidade (8 a 11).

Aspectos Numéricos

O método das características foi implementado usando técnicas de diferenças finitas. A fig. 1 mostra esquematicamente a malha usada para a determinação das propriedades em um novo ponto (4) a partir de três outros conhecidos (1, 2 e 3). A técnica consiste na determinação da posição deste ponto através da intersecção da linha de Mach a esquerda (C+) com a linha de corrente (Co). A linha de Mach a direita (C-) é então estendida para trás de modo a se localizar o ponto 5 entre 2 e 3, sendo que as propriedades de escoamento são calculadas por interpolação linear. As propriedades de escoamento do ponto 4 são obtidas pela integração das equações de compatibilidade ao longo da linha de corrente e das duas linhas de Mach.

Ao longo das linhas de Mach (C+ e C-) o método de integração utilizado foi o preditor-corretor (P(EC)^n), conforme Zucrow et al. (1977), por serem as equações mais simples do ponto de vista numérico. Sobre a linha de corrente foi adotado o método de multivalores de GEAR (1971) que é adequado à integração de equações tipo "stiff" encontradas no modelamento do mecanismo de reação do problema.

Como o método das características aqui usado está restrito ao escoamento supersônico, existe a necessidade de uma linha de partida de propriedades conhecidas localizada após a linha sônica do bocal. Esta linha é de Mach e composição química constante e foi obtida através da série de Kliegel et al. (1965).

1, 2 e 3 Pontos Iniciais
5 Ponto Interpolado
4 Ponto Solução
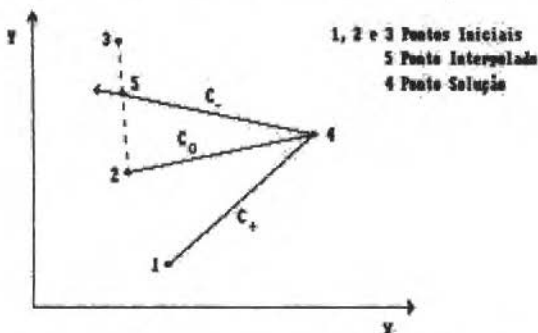
Fig. 1   Malha de diferenças finitas empregada

O programa de computador foi implementado num equipamento compatível com a linha IBM-PC 386. A linguagem de programação empregada foi TURBO PASCAL 5.5. O tempo de processamento neste equipamento varia conforme o bocal a ser calculado, mas para os casos aqui documentados este é inferior a 10 horas.

Análise dos Resultados

O primeiro bocal é um bocal de divergente cônico com as seguintes características: Posição da garganta: $x = 0,06$ m; Raio da garganta: $r_t = 0,0127$ m; Raio de curvatura da garganta circular: $r_{ct} = 0,0508$ m; Ângulo do convergente: $45°$; Ângulo do divergente cônico: $15°$; Razão de expansão: $50:1$.

Os reagentes são (H_2 e F_2) injetados a 298,15 K, numa razão de mistura por massa de oxidante/combustível igual a 12 e a pressão na câmara é de $6,895 \times 10^5$ Pa. As demais condições na câmara de combustão foram calculadas com o programa termoquímico NASA-SP-273 (Gordon et al., 1971). A composição química na garganta foi obtida com o programa reativo unidimensional elaborado por Barros et al. (1990). A Fig. 2 mostra as curvas de fração molar de alguns dos produtos de combustão, a Fig. 3 mostra o número de Mach "congelado" e a Fig. 4 mostra a temperatura e a velocidade, calculados para a parede e o eixo ao longo do bocal.

Fig. 2   Fração molar dos produtos de combustão H e H_2 para o sistema reativo H_2 e F_2 (Modelo 2D)
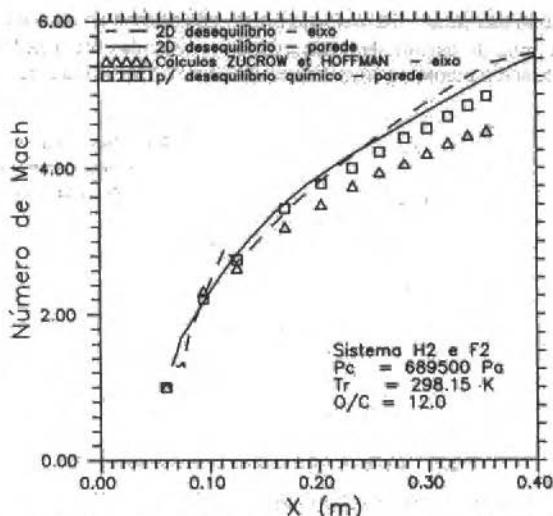
Fig. 3 Número de Mach ao longo do bocal para o sistema reativo H_2 e F_2 (Modelo 2D)
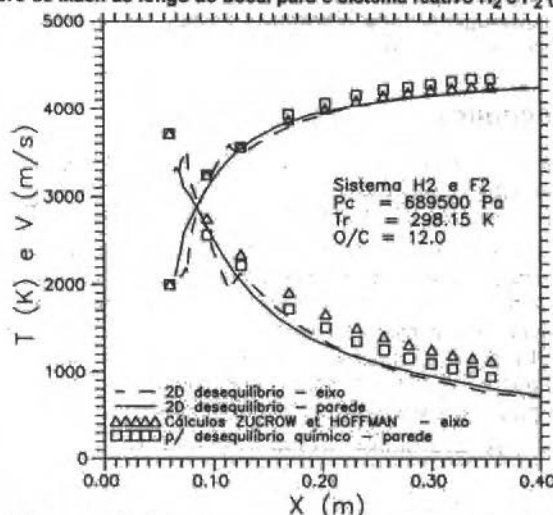
Fig. 4 Temperatura estática e velocidade do escoamento ao longo do bocal para o sistema reativo H_2 e F_2 (Modelo 2D)

Considerando F_2, H_2, H e F como produtos da combustão dos reagentes, o mecanismo de reação utilizado nos cálculos, proposto por Cherry, constante em Zucrow e Hoffman (1977), é apresentado a seguir, juntamente com as expressões para as constantes cinéticas (unidades em cm, mol, K e s):

$$2F + M \rightleftharpoons F_2 + M \qquad K_f = 1{,}10 \times 10^{18} \; t^{-1,5}$$

$$2H + M \rightleftharpoons H_2 + M \qquad K_f = 7{,}50 \times 10^{18} \; t^{-1,0}$$

$$F + H + M \rightleftharpoons HF + M \qquad K_f = 7{,}50 \times 10^{18} \; t^{-1,0}$$

$$F_2 + H \rightleftharpoons F + HF \qquad K_f = 5{,}28 \times 10^{12} \; t^{0,5} \exp(-4000/t)$$

$$F + H_2 \rightleftharpoons H + HF \qquad K_f = 5{,}00 \times 10^{12} \exp(-5700/t)$$

$$F_2 + H_2 \rightleftharpoons 2HF \qquad K_f = 1{,}75 \times 10^{10} \; t^{0,5} \exp(-19997/t)$$
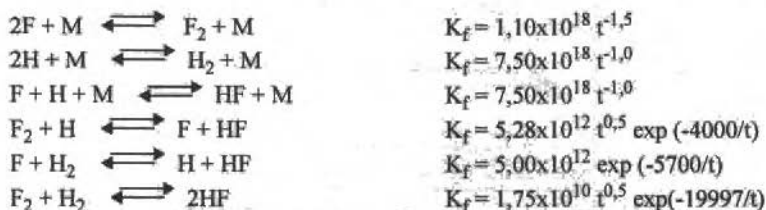
onde, M é um terceiro corpo participante das reações. Nos cálculos aqui apresentados a fração mássica de M é admitida igual a 1,0, sendo o seu peso molecular igual ao peso molecular médio da mistura, ou seja, todas as moléculas presentes foram consideradas como possíveis terceiros corpos com iguais eficiências, conforme recomendado por Montchilof (1963).

As propriedades dinâmicas de cada espécie química presente foram calculadas por meio de regressões polinomiais de quarta ordem dos dados publicados nas tabelas JANNAF (Gordon e McBride 1971), e atualizadas conforme Chase et al. (1982).

Alguns dos resultados encontrados estão mostrados nas Figs. 2 a 4 para escoamentos reativo, em desequilíbrio químico, unidimensional (1D) e bidimensional (ao longo da parede e do eixo do bocal). Estes resultados foram comparados com outros teóricos obtidos de Zucrow e Hoffman (1977), para o mesmo bocal. As diferenças encontradas nos dois cálculos, principalmente na parte final do divergente, são devidas às precisões diferentes entre os métodos e dos algoritmos de construção da malha empregados. A precisão deste trabalho (sexta ordem) é teoricamente superior a dos resultados apresentados por Zucrow e Hoffman (1977) (segunda ordem). O choque no eixo detectado pelo método aqui implementado, previsto teórica e experimentalmente, prova a melhor precisão do presente trabalho. Com isto o programa de computador elaborado foi considerado válido frente a dados teóricos. A seguir foi feita a validação do modelo em relação a resultados experimentais.

O segundo bocal calculado é apresentado na Fig. 5. Os reagentes (H_2 e O_2) são injetados a 285,6 K e 279,2 K, respectivamente, numa razão de mistura por massa de oxidante/combustível igual a 3,84, sendo a pressão na câmara de $24,82 \times 10^5$ Pa. As demais condições na câmara de combustão foram calculadas com o programa termoquímico NASA-SP-273, (Gordon e McBride 1971). A Fig. 6 mostra algumas curvas de fração molar dos produtos de combustão ao longo do eixo e da parede do bocal. Na Fig. 7 estão traçadas as curvas de pressão estática ao longo do bocal.

Fig. 5 Posição da garganta: x = 0,03435 m; Raio da garganta: r_t = 0,0172 m; Raio de curvatura da garganta circular: r_{ct} = 0,0254 m; Ângulo do convergente: 25°; Razão de expansão: 1030:1
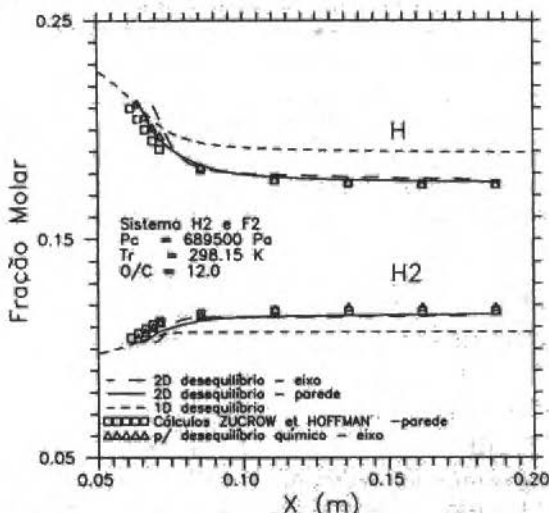

Fig. 6 Fração molar dos produtos de combustão H e H_2O para o sistema reativo H_2 e O_2 (Modelo 2D)

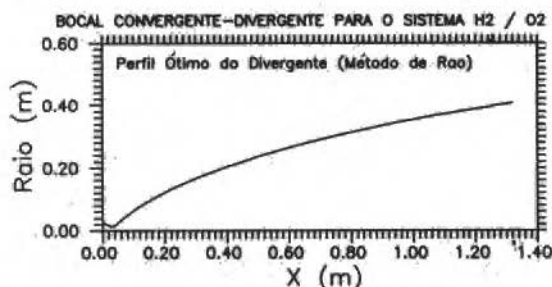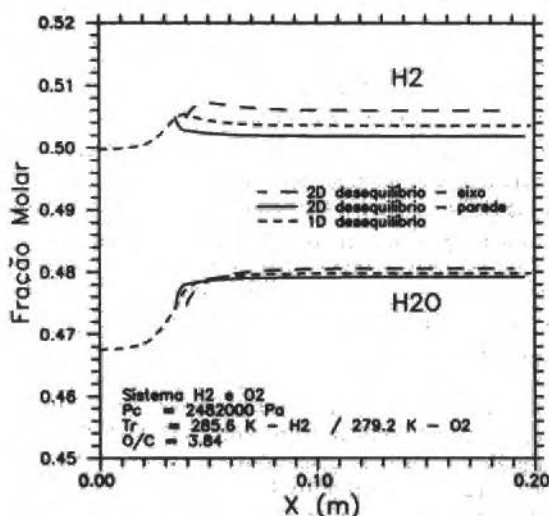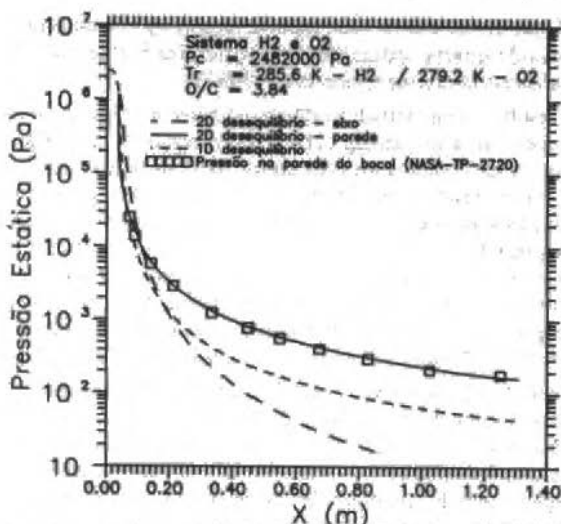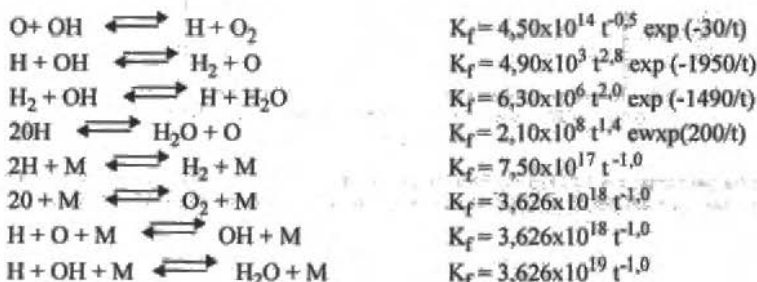Fig. 7   Pressão estática ao longo do bocal para o sistema reativo H_2 e O_2 (Modelo 2D)

Considerando H, H_2, H_2O, O, O_2 e OH como produtos da combustão dos reagentes, o mecanismo de reação utilizado nos cálculos é apresentado a seguir, juntamente com as expressões para as constantes cinéticas (unidades em cm, mol, K e s):

$$O + OH \rightleftharpoons H + O_2 \qquad K_f = 4,50 \times 10^{14}\, t^{-0.5} \exp(-30/t)$$

$$H + OH \rightleftharpoons H_2 + O \qquad K_f = 4,90 \times 10^3\, t^{2.8} \exp(-1950/t)$$

$$H_2 + OH \rightleftharpoons H + H_2O \qquad K_f = 6,30 \times 10^6\, t^{2.0} \exp(-1490/t)$$

$$2OH \rightleftharpoons H_2O + O \qquad K_f = 2,10 \times 10^8\, t^{1.4} \text{ewxp}(200/t)$$

$$2H + M \rightleftharpoons H_2 + M \qquad K_f = 7,50 \times 10^{17}\, t^{-1.0}$$

$$2O + M \rightleftharpoons O_2 + M \qquad K_f = 3,626 \times 10^{18}\, t^{-1.0}$$

$$H + O + M \rightleftharpoons OH + M \qquad K_f = 3,626 \times 10^{18}\, t^{-1.0}$$

$$H + OH + M \rightleftharpoons H_2O + M \qquad K_f = 3,626 \times 10^{19}\, t^{-1.0}$$

onde M é um terceiro corpo qualquer, sobre o qual foram feitas as mesmas considerações do sistema (H_2 e F_2). Deve-se observar que as 5 primeiras constantes Kr acima foram retiradas de Cohen e Westberg (1982) e as demais de Jensen e Kurzius (1965).

Também aqui as propriedades termodinâmicas de cada espécie química presente foram calculadas por meio de regressões polinomiais de quarta ordem dos dados publicados nas tabelas JANNAF, Gordon e McBride (1971), e atualizados conforme Chase et al. (1982).

As Figs. 6 e 7 mostram os resultados encontrados para escoamentos reativos, em desequilíbrio químico, unidimensional e bidimensional (ao longo da parede e do eixo do bocal). O cálculo da pressão estática foi comparado com medidas experimentais obtidas por Pavli et al. (1987) na Fig. 7. Pode-se ver que a concordância entre os dados é muito boa.

A tabela 1, a seguir, traz os valores de impulso específico no vácuo (Isp_v) calculados por diversos métodos, os quais são comparados com medidas experimentais (NASA-TP-2725), Smith et al. (1987). Os modelos usados nos cálculos são: unidimensional reativo em desequilíbrio químico, Barros et al. (1990), unidimensional em equilíbrio químico (NASA-SP-273), Gordon e McBride (1971), unidimensional e bidimensional em desequilíbrio químico (NASA-TP-2725), Smith et al. (1987) e do presente trabalho (2D Desequilíbrio). Uma correção de camada limite é aplicada aos resultados dos modelos 2D em desequilíbrio químico.

Tabela 1 Impulsos específicos previstos neste trabalho, por Smith et al. (1987) e o experimental, relativos ao sistema H_2 e O_2

	Isp_v (s)	
	NASA-TP-2725	Este trabalho
2D Desequilíbrio Camada Limite	482,7	467,5
2D Desequilíbrio	494,2	479,7
1D Desequilíbrio	498,5	498,5
1D Equilíbrio	504,8	504,8
NASA_TP-2725 (experimental)	468,9	

Dos métodos indicados na tabela 1 acima, aquele com menos hipóteses restritivas é o modelo bidimensional em desequilíbrio químico (presente trabalho e do NASA-TP-2725), segue-se o modelo unidimensional em desequilíbrio químico e o unidimensional em equilíbrio químico (NASA-SP-273). Pode-se notar que as previsões de impulso específico no vácuo são coerentes, pois o método menos restritivo possui os melhores resultados. A correção da camada limite melhora ainda mais as previsões.

Os resultados deste trabalho apresentaram os menores desvios percentuais em relação ao valor experimental. Após a correção de camada limite o desvio da previsão foi de apenas 0,3%, enquanto que o melhor resultado de Smith et al. (1987) apresenta um desvio de 3%.

Conclusão

A hipótese de escoamento bidimensional com reação química em desequilíbrio, mostrou-se bastante adequada para o cálculo dos parâmetros de escoamento e de desempenho de bocais convergente-divergente, numa ampla faixa de razões de expansão (utilizaram-se valores para bocais de 50:1 e 1030:1). Neste trabalho foram obtidos melhores resultados do que aqueles fornecidos por outros modelos unidimensionais e bidimensionais reativos (tabela 1).

O programa computacional elaborado possibilita encontrar resultados para sistemas reativos complexos, desde que seja conhecido o mecanismo das reações envolvidas. Cabe observar que, apesar de existir nas referências programas com as mesmas hipóteses deste trabalho (2D em deseql.), os mesmos não estão disponíveis na literatura.

Este estudo será usado para a otimização da configuração dos bocais por onde escoam fluidos reativos, visando melhorar ainda mais os projetos de motores a jato.

Referências

Barros, J.E., Alvim Filho, G.F. e Paglione, P., 1990, "Estudo de Escoamento Reativo em Desequilíbrio Químico Através de Bocais Convergente-Divergente", Anais do I Encontro Nacional de Ciências Térmicas, Vol. 2, pp. 771 a 776, Itapema, Brasil.

Chase, M.W. et alli, 1982, "JANNAF Thermochemical Tables, 1982 Supplement", Journal of Physical and Chemical Reference Data, Vol. 11, No. 3.

Cohen, N., e Westberg, K.R., 1982, "Chemical Kinetic Data Sheets for High-Temperature Chemical Reactions", Journal of Physical and Chemical Reference Data, Vol. 11, No. 3.

Gear, C.W., 1971, "Numerical Initial Value Problems in Ordinary Differential Equations", Prendice Hall Inc., New Jersey.

Gordon, S., e McBride, B.J., 1971, "Computer Program for Calculation of Complex Chemical Equilibrium Compositions, Rocket Performance, Incident and Reflected Shocks, and Chapman-Jouguet Detonations", NASA-SP-273.

Jensen, D.E., e Kurzius, S.C., 1965, "Rate Constant for Calculations on Nozzle and Rocket Exhaust Flow Fields", NASA-TP-149.

Kacynski, K.J., Smith, T.A., e Pavli, A.J., 1987, "Experimental Evaluation of Heat Transfer on a 1030:1 Area Ratio Rocket Nozzle", NASA-TP-2726.

Kliegel, J.R., e Levine, J.N., 1965, "Transonic Flow in Small Throat Radius Of Curvature Nozzles" In: AIAA Journal, Washington, American Institute of Aeronautics and Astronautics (AIAA), Vol. 7, No. 7, pp. 1375-1378, Jul..

Momtchiloff, I.N., 1963, "Kinectics in Hydrogen-Air Flow System. I. Calculation of Ignition Delays for Hypersonic Ramjets", 9th Symposium (International) on Combustion, pp. 220-230, Academic Press, New York.

Paglione, P., e Girardi. R.M., 1988, "Análise Teórica e Experimental para Bocais de Tração Máxima", Anais do II Encontro Nacional de Ciências Térmicas (ENCIT 88), pp.45-48, Águas de Lindóia, Brasil.

Pavli, A.J., Kacynski, K.J., e Smith, T.A., 1987, "Experimental Thrust Performance of a High-Area-Ratio Rocket Nozzle", NASA-TP-2720.

Smith, T.A., Pavli, A.J., e Kacynski, K.J., 1987, "Comparation of Theoretical and Experimental Thrust Performance of a 1030:1 Area Ratio Rocket Nozzle at a Chamber Pressure of 2413 kN/m^2 (350 psia)", NASA-TP-2725.

Zucrow, M.J., e Hoffman, J.D., 1977, "Gas Dynamics", John Wiley and Sons, New York, Vol. II.

An Integro-Differential Model for the Heat Transfer in Forest Fires

Antonini Puppin Macedo
Antonio C.P. Brasil Jr.
Universidade de Brasília
Departamento de Engenharia Mecânica
70910-900 Brasília, Brazil

Abstract

The influence of radiative changes between the flame and the forest material, at ground level, is given by integral models deriving from the radiosity balance between an emitting volume and the receiving surface. Thus, the heat transfer can be described by a convolution integral where the flame influence is quantified by a Green function that describes the heat exchange decay by the distance from the flame. From this approach, the formulation of an integro-differential model is proposed and numerically implemented by a Monte Carlo Integration / Explicit Euler propagation coupled method.

Keywords: Forest Fires, Radiative Heat Transfer, Monte Carlo Integration

Introduction

Physical phenomena involved in the combustion of forest biomass, during natural or accidental fires, are extremely complex and its behavior involves advanced knowledge related to fluid dynamics and heat transfer in reacting media. The current importance of the study of this kind of problems, within the scope of mathematical modelization and numerical simulation, as well as advanced experimentation, are justified by the growth of the international interests related to environmental questions. An important point of interest is the necessity of evaluation of the amount of emissions in atmosphere, specially CO, CO_2, and particulates, due to forest biomass burn.

Besides many environmental problems related to forest fires, one can list some of great importance: the after cutting burning in Amazon (Queimada), the natural fires in the Brazilian Cerrado, the pasture maintenance fires in Amazon and sugar cane culture burns. A priority might given to the Queimada due to its large amounts of CO_2 emissions involved. In this process, an area of the forest is cut during the beginning of the Amazon dry season (june to october). Two or three months later, when the forest material is dry, it is burned. Part of it is converted in combustion gases, and this way, spread into the atmosphere. Other part is laid on the ground in the form of char.

As this practice is very used during the dry season in Amazon, in recent years, several burns have been observed inducing many controversies about its rule in the increase of the Greenhouse effect. Some recent works such as Kirkchoff et al. (1989), Carvalho et al. (1993), Fearnside et al. (1993) and Kaulfman et al. (1992) show that the rates of CO_2 emissions in the atmosphere are less than the amount stated in several international works, and that new experimental and theoretical studies must be strongly encouraged.

Among some works related to the simulation and modelization of physical phenomena during forest fires, the Russian literature is specially rich. The works developed by Dorrer (1984a), (1984b) present models of propagation of forest fires that are adopted as a basis for the present work. The works of Brabander et al. (1989) e Grishin et al. (1985) use a mixture theory like approach that describes conveniently in situ observations of fires in homogeneous forest. Still on the Russian literature, the works of Konev (1984), on the propagation of flame fronts in surface fires, and Grishin et al. (1984), about the effects of thermals during forest fires are cited.

Some other works present relevant aspects of heat transfer in forest fires: The works from Rothermel (1972) and Albini (1976). In this last work, the heat transfer is quantified by a Green Function integral. This model is the basis of the works from Dorrer cited above. Anderson (1968) proposes a simplified model of forest fires propagation based on discrete convolution methods which were recently improved by Richards (1988).

Some combustion-fluid dynamics coupled approaches can also be found in the literature (Siqueira (1993)). In this work, the simplified model of Rothermel is coupled to a turbulent flow simulation code.

Mathematical Model

The propagation of the combustion in a general layer of forest fuel will be considered in a fixed cartesian coordinate system x, y, z. In two dimensions, a continuous layer **(x,y) can be considered for surface fires. In a generic point C(x,y) of this layer the potential forest fuel, in a time instant t, can be in one of three states defined by the function s(x,y,t):

$$s(x,y,t) = \begin{cases} 0, \text{ if there is potential fuel, but no combustion;} \\ \\ 1, \text{ if there is combustion (mass decay);} \\ \\ 2, \text{ if there is no pontential fuel and the combustion is impossible.} \end{cases} \qquad (1)$$

In $s(x,y,t) = 0$ generally the heating and evaporation are related only to the moisture, so it is a process involving only water. Therefore, a general equation for the enthalpy increase is valid.

In $s(x,y,t) = 1$ a biomass combustion model can be implemented by proposing a general rule to the chemical components of the combustion products. The combustion of forest fuels is quantified by the kinetics of the pyrolizis reaction.

In this process, reaction velocity is established for the formation of each of its products and also for each complete reaction stage. To evaluate a general description for a forest fire, a global reaction model is proposed for the decay in this point $C(x,y)$ at $s(x,y,t) = 1$ as follows:

$$\frac{\partial m(x,y,t)}{\partial t} = -K \qquad (2)$$

where K is the velocity rate of reaction that can be given by a Arrhenius term:

$$K = A\left(\left[O_2\right], T\right) \exp\left(-\frac{E}{RT}\right) \qquad (3)$$

In this equation, $[O_2]$ is the concentration of oxygen in the air layer in contact with the material in combustion. T is the gas temperature and R the gas constant. A and E are characteristics constants of the combustion of forest material (see Kaviani and Fatehi 1992). These constants can also be evaluate from the experimental exponential decay plots of Rothermel (1972).

The heat produced during the combustion is thus given by:

$$\Phi(x,y,t) = -K\Delta Hm \qquad (4)$$

where ΔH is the specific heat of the forest fuel.

Besides the complexities involving the heat transfer between the fire front (s = 1) and the region with no combustion (s = 0), a general equation, based on the previous work from Dorrer (1984) can be proposed for the variation of enthalpy:

$$\frac{\partial H(x,y,t)}{\partial t} = q_{rad} - q_c \qquad (5)$$

$H(x,y,t)$ is the enthalpy of the forest material, q_{rad} is the radiative heat flux and q_c is the convective one.

These terms are given by:

$$q_c = \bar{U}(T - T\infty) \tag{6}$$

$$q_{rad} = \iint \Phi(x',y',t)\,\xi(x-x',y-y')\,dxdy \tag{7}$$

In those equations, $\bar{U}$ is a convective heat transfer coefficient and $\xi(x-x',y-y')$ is a flame influence function proposed by Dorrer (1994) as (in polar coordinates):

$$(x-x',y-y') = \xi(r,\theta) = a_0\delta\left(1-\frac{\delta}{3h_f}\right)\exp\left(\frac{r\cos^2\alpha_f}{r_o(1+\sin^2\alpha_f\cos\theta)}\right) \tag{8}$$

The parameters in this equation are:

a_0: fraction of the heat spent in the propagation of the combustion.

δ: Thickness of the fuel bed.

h_f: flame height.

α_f: Flame inclination angle.

r_0: Effective flame effect radius.

As the function $\xi(x-x',y-y')$ is in polar coordinates, r and θ are the polar coordinates with origins in the point $C(x,y)$, and x' and y' are its neighbors.

Numerical Methods

The present model was implemented by means of an explicit time discretization for the entalphy variation, mass decay and heat produced.

$$H^{t+\Delta t} = H^t + \Delta t\,(q_{rad}^t - q_c^t) \tag{9}$$

$$m^{t+\Delta t} = m^t - K^t\Delta t \tag{10}$$

$$\Phi^{t+\Delta t} = -K^t\Delta H_m \tag{11}$$

Before the calculation of the enthalpy variation, it is necessary to calculate the heat accumulation given by q_{rad}. As this function is an undefined integral of a continuous function, it can not be calculated by a simple direct convolution. In later works from Puppin Macedo and Brasil Junior (1994), it was possible due to special discrete characteristics of the model. Some convolution matrices were defined giving good qualitative behaviour of the propagation but imposing some difficulties in their calibration from experimental and field information.

The use of a Green function gives good possibilities of calibration and comparisons with experiment and field information, but imposes the use of more refined integration techniques. Under this situation, the use of a Monte-Carlo method was chosen due to its facilities of implementation. Besides, it works very well with the Green function used, giving good precision.

The Monte Carlo Method is very well cited to smooth multidimensional functions in an easy to sample region. The Green Function used in this model has all these features.

The region of interest is defined by a flame influence parameter defined by the characteristics of the flame (height, intensity etc.). This parameter can be experimentally defined as the distance, from the flame front, for the decay of the temperature to a value close to the value of the unheated fuel bed. Thus, a simple Monte Carlo Method can be used.

To perform it, N random numbers are set uniformly distributed in a multidimensional volume V. These points are called $\{x1, ..., xn\}$. Then the basic theorem of Monte Carlo integration estimates that the integral of a function f over the multidimensional volume is given by:

$$\int f dV \approx V \langle f \rangle \pm V \sqrt{\frac{\langle f^2 \rangle - \langle f \rangle^2}{N}} \tag{12}$$

Here the angle brackets denote taking the arithmetic mean over the N sample points,

$$\langle f \rangle \equiv \frac{1}{N} \sum_{i=1}^{N} f(x_i) \tag{13}$$

$$\langle f^2 \rangle \equiv \frac{1}{N} \sum_{i=1}^{N} f^2(x_i) \tag{14}$$

The "plus or minus" term in Eq. (12) is a one standard deviation error estimate for the integral, not a rigourous bound; further, there is no guarantee that the error is distributed as a Gaussian, so the error term should be taken only as a rough indication of probable error. On the other hand, it is possible to infer that the error is inversely proportional to the square root of the number of points N by the Eq. (12) above.

The algorithm used was very straightforward due to characteristics of the flame effect function used. At each time step of the time propagation a random set of numbers (in polar coordinates) is set around the grid point in the space discretization grid. These points generate a random Monte Carlo sub-grid. As a large random sequence is needed, so the long period random number generator presented by Press et al. (1993) is used. After each time step a new sub-grid is generated in order to avoid conditioned propagation of the solutions.

The points in this sub-grid may lay on a region of several points in the main grid, thus an interpolation routine in performed for all variables envolved in the calculation of the integral.

To assure the precision of the integration routine implemented it was tested for a defined integral and an error of about 10% is usually observed for a set of 500 random points.

Results and Discussion

To perform initial tests on the model, some basic configurations were chosen. A square unitary grid of 50 x 50 points was used for the spatial discretisation. For the Monte Carlo integration 500 sample points were used. Thus, the total grid size can be considered as 50 x 50 x 500 (1250000 points).

Simulations were performed only in order to assure stable propagation of the solution. The parameters envolved in the calculations are presented in Table 1.

Table 1 Physical Parameters

Enthalpy	Dimensions	Others
H_o = 400 MJ/kg	Space = 5x5 m	Mass = 0,5 kg/m^2
H_∞ = 400 MJ/kg	Grid = 50x50 pts.	flame = 45°
H_{ig} = 800 MJ/kg	Sub-Grid = 500 pts.	---
H_{init} = 1100 MJ/kg	Time step = 0,01 sec	---

The flame inclination angle of 45° corresponds to a mid-flame wind velocity of about 2 m/s, as given by a Fr number relation from Ventura et al. (1989) and Albini (1981). A flame height of 0.7 m, as normally observed in surface fires, (Baines, 1990) was used here.

Two cases of interest were chosen for the initial simulations: a front evolution and a Queimada. In this second case, a square set of points is burned trying to reproduce this after cut burn technique in Amazon.

As an initial condition for the front evolution case, a line of several points in the grid were ignited, as show in Fig. 1.
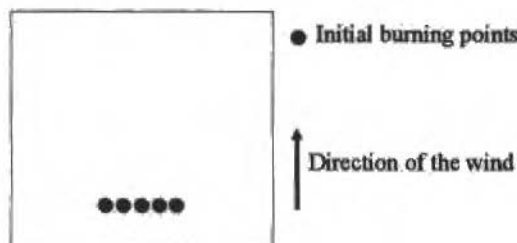

● Initial burning points

Direction of the wind

Fig. 1   Fire front initial condition

The time evolution of this front is shown in Fig. 2. As expected, the front evolutes regularly driven by the wind. The velocity of propagation in the direction of the wind is faster than in the opposite one. In the transition between ignited zones and non-ignited ones, the enthalpy do not reaches the ignition enthalpy and a small region of heating can be observed, as expected.
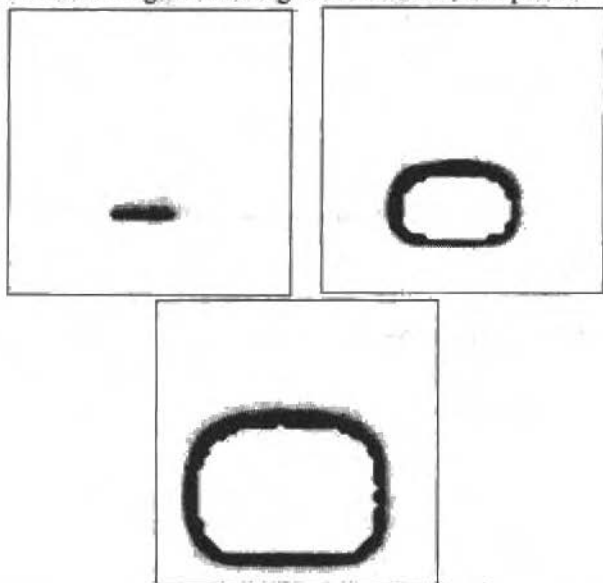

Fig. 2   Evolution of the front fire

The mass decay can be observed in the regions of the evolution of the burn as the fire consumes the forest fuel layer. In the implemented model an amount of residual forest material is allowed after the burn but, in the present case, it was not considered.

To perform the initialization of the Queimada case, a square set of points was ignited as shown in Fig. 3. In this case, the burn evolutes in a very efficient wa burning a large forest region in a small time interval (Fig. 4). Thus, the rates of combustion gases release are expected to be very high. The effect of adjacent small fire fronts usually make two different main fronts to evolute. One evolutes in the inside direction of the initial square burn set and other one in the outside direction. Between these fronts an expanding ring of burned material is formed, avoiding the propagation through it.
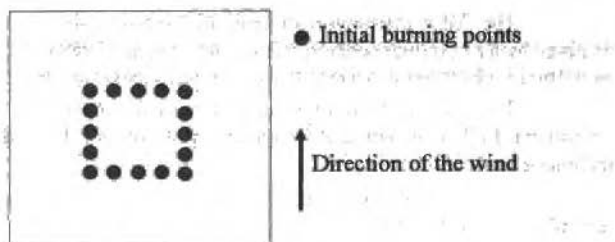
● Initial burning points

↑ Direction of the wind

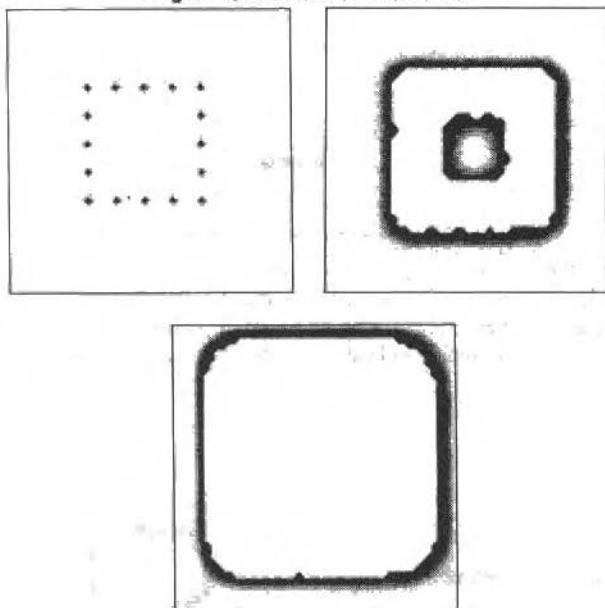Fig. 3   Queimada initial conditions

Fig. 4   Queimada evolution

Conclusions and Perspectives

As it can be seen from the results present here, the model has a good qualitative behavior and introduces a very useful approach to the numerical simulation of forest fires. The evolution of the propagation agrees very well with what was expected from previous works, as well as it allows the approach of many different situations.

The equations of the proposed model are based on many physical parameters easy to determine from experiments classically performed and usually found in the literature.

The radiative heat accumulation given by a convolution integral gives a straightforward way to approach the radiative changes in means of a partially-transparent radiative forest medium. On the other hand, the calibration of the flame effect function and convolution function coefficients must be carefully done in order to rigorously fit the physical characteristics of the phenomena.

The heat losses terms, nevertheless, are not very well modelizaded in the present work and new considerations must be done specially following related topics in previous works like: de Mestre et al. (1989), and Baines (1990). Some strong evidences showing the rule of the convective terms must also be taken into account in order to better characterize the phenomena.

By the results shown here, the stability of this approach is assured. The implementation of other different terms in the equations to deal with convective effects and others may not compromise its precision and stability.

This work gives the tools to the implementation of a new model in the forest fire heat transfer problem, making it also possible to be applyble to other situations. The qualitative physical behavior of the model is very satisfactory and its calibration parameters are general enough to deal with many different practical situations.

References

Albini, F.A. 1976, "Estimating Wildfire Behavior and Effects", USDA Forestry Service, Gen. Tech. Rep. INT-30.

Anderson, H.E. 1968, "Sundance Fires, an Analysis of Fire Phenomena", USDA Forestry, Paper INT-56.

Baines, P.G. 1990, "Physical Mechanisms for the Propagation of Surface Fires", Math. Comput. Modelling, 13, 12, 83-94.

Brabander, O.P. Vdovina, O.A. Grishin A.M. and Gruzin, A.D. 1989, "Investigation of the Conditions of Transition of a Surface Forest Fire to a Crown Fire", Comb. Expl. and Shock Waves, 24, 4, 435-440.

Carvalho Jr. J.A., Santos,J.M. Santos, J.C., Leitão M.M. and Higuchi, N. 1993, "Forest Cleaning Combustion experiment in Manaus Region", INPE Internal Repport.

Dorrer, G.A., 1984a, "A Model for Propagation of Curvilnear Forest Fire Fronts", Comb. Expl. and Shock Waves, 20, 1, 8-15.

Dorrer, G.A., 1984b, "A Model of the Spreading of a Forest Fire", Heat Tranfer - Soviet. Res., 16, 6, 39-52.

Fearnside, P.M. Leal Jr., N. e Fernandes, F.M. 1993, "Rainforest Burning and the Global Budget: Biomass, Combustion Efficiency and Charcoal Formation in Brazilian Amazon", J. of Geoph. Research, 98, 16733-16743.

Grishin, A.M., Alekseyev, N.A., Brabander O.P. and Zal'Mezh, V.F. 1984, "Propagation of Forest Fire-Induced Thermals in the Ground Layer of the Atmosphere", Heat Tranfer - Soviet Res., 16, 6, 28-38.

Grishin, A.M., Gruzin A.D. and Zverev, V.G. 1985, "Study of the Structure and Limits of Propagation of the Front of an Upstream Forest Fire", Comb. Expl. and Shock Waves, 21, 1, 9-18.

Kaufman, Y.J., Setzer, A. Ward, D., Tanre, D., Holben, B.N., Menzel, Pereira, P. M.C.and Rasmussen, R. 1992, "Biomass Burning Airborne and Spaceborne Experiment in Amazonas (BASE-A)", J. of Geoph. Research, 97, 14581-14599.

Kaviani, M. and Fatehi, M. 1992, "Combustion in Porous Media", Anais do IV ENCIT, p17-p38.

V.W.J.H.A. Kirkchhoff, A.W. Seter e M.C.P. Pereira, Biomass Burning in Amazonia, 1989, Seasonal Effect on Atmosphere O_3 and CO, Beophys. Res. Lett., 16, 459-472.

Kirkchhoff, V.W.J.H.A. 1993, "Queimadas na Amazonia e o Efeito Estufa", Ed. Contexto.

Konev, E.V. 1984, "Analysis of the Spreading of Natural and Intentionally Set Forest Fires", Heat Tranfer - Soviet Res., 16, 6, 1-27.

Mestre, N.J. de Catchpole, E.A., Anderson, D.H. and Rothermel, R.C., 1989, "Uniform Propagation of a Planar Fire Front Without Wind", Comb. Sci. and Tech., 65, 231-244.

Press et al., 1993, Numerical Recipes 2nd Ed., Cambridge Press.

Macedo, A. Puppin and Brasil Junior, A.C.P. 1984, "Numerical Simulation of Ground Forest", Anais do CBEM/NME 94.

Richards, G.D. 1988, "Numeical Simulation of Forest Fires", Int. J. of Num. Meth. Engineering, 25, 625-633.

Rothermel, R.C. 1972, "A Mathematical Model for Fire Spread Prediction in Wildland Fuels", USDA Forest Service Res. Paper INT-115.

Siqueira de, M.B.B. 1993, "Cálculo Numérico do Escoamento Tridimensional sobre Terreno Complexo e na Vizinhança de um Fogo Florestal", Dissertaçao de Mestrado, IST, Lisboa.

Inverse Heat Conduction Problem for the Estimation of the Temperature Dependence of Thermal Conductivity

H. R. B. Orlande
Programa de Engenharia Mecânica
COPPE/UFRJ, Cx. Postal: 68503
Rio de Janeiro, 21945-970

M. N. Ozisik
MAE Department
North Carolina State University
Raleigh, NC 27695-7910, USA

Abstract

In this paper we use the Conjugate Gradient Method with Adjoint Equation in order to estimate the temperature dependence of thermal conductivity. The accuracy of this method of inverse analysis is verified by using simulated measurements as the input data for the inverse problem. Functional forms containing sharp corners and discontinuities are generally very difficult to recover by an inverse analysis. The present approach is capable of handling such situations quite readily and accurately.
Keywords: Thermal Conductivity, Inverse Heat Conduction, Temperature Dependence

Introduction

A vast amount of literature exists on the analysis and solution of linear inverse heat conduction problems. In the case of nonlinear inverse heat conduction, the available works were mostly concerned with the estimation of thermophysical properties, where the dependence of the unknown quantity on temperature was approximated by a polynomial (Artyukhin, 1975), B-splines (Artyukhin, 1982, 1987, 1993) or piecewise linear continuous functions (Jarny et al., 1986 and Goryachev and Yudin, 1981). With such approaches, the inverse analysis was reduced to the determination of the constant coefficients of the functional form assumed for the unknown (i.e., a finite dimensional minimization problem). The steepest descent (Artyukhin, 1975 and 1987, and Jarny et al., 1986) or the conjugate gradient method (Artyukhin, 1982, and Goryachev and Yudin, 1981) have been used for the solution of such parameter estimation problems.

If no information is available on the functional form of the unknown quantity, the minimisation has to be performed on an infinite dimensional space of functions. Such novel approach for the determination of temperature-dependent quantities has been successfully applied to the estimation of the reaction function by Orlande and Ozisik (1993).

In this work we apply a function estimation approach based on the conjugate gradient method of inverse analysis with adjoint equation to estimate the unknown thermal conductivity in a non-linear transient heat conduction problem. It is assumed that no prior information is available on the functional form of the unknown quantity. The accuracy of the present method is examined under strict conditions, by using transient simulated measured data in the inverse analysis.

Inverse Analysis for Estimating Thermal Conductivity

The inverse analysis of function estimation approach, utilizing the conjugate gradient method with adjoint equation considered here, consists of the following basic steps (Jarny et al., 1991):

1. The direct problem;

2. The inverse problem;

3. The sensitivity problem;

4. The adjoint problem and the gradient equation;

5. The conjugate gradient method of minimization;

6. The stopping criterion; and

7. The computational algorithm.

We present below the salient features of each of these steps, as applied to the estimation of the unknown thermal conductivity.

The Direct Problem. For the present study, the direct problem is taken as:

$$C(T)\frac{\partial T(x,t)}{\partial t} - \frac{\partial}{\partial x}\left[k(t)\frac{\partial T}{\partial x}\right] - g(T) = 0 \text{ in } 0 < x < L; \text{ for } t > 0 \tag{1.a}$$

$$\frac{\partial T}{\partial x} = 0 \text{ at } x = 0; \text{ for } t > 0 \tag{1.b}$$

$$k(T)\frac{\partial T}{\partial x} = \phi_L(t) \text{ at } x = L; \text{ for } t > 0 \tag{1.c}$$

$$T(x,0) = F(x) \text{ for } t=0; \text{ in } 0 < x < L \tag{1.d}$$

The direct problem defined above by Eqs.s (1) is concerned with the determination of the temperature distribution $T(x,t)$ in the medium, when the physical properties $C(T)$ and $k(T)$, the boundary and initial conditions, and the reaction function $g(T)$ are known. In order to solve this direct problem, we used the combined method of finite differences with $\theta=2/3$ and the resultant nonlinear system of algebraic equations was linearized by the expansions:

$$k^{n+1} = k^n + \left(\frac{dk}{dT}\right)^n (T^n - T^{n-1}) \tag{2.a}$$

$$C^{n+1} = C^n + \left(\frac{dC}{dT}\right)^n (T^n - T^{n-1}) \tag{2.b}$$

$$g^{n+1} = g^n + \left(\frac{dg}{dT}\right)^n (T^n - T^{n-1}) \tag{2.c}$$

were the subscript "n" denotes the time step.

The Inverse Problem. For the inverse problem, the thermal conductivity $k(T)$ is regarded unknown but everything else in Eqs. (1) is known. In addition, temperature data are considered available at some appropriate locations within the medium at various time steps.

The inverse analysis utilizing the conjugate gradient method requires the solution of the direct, sensitivity and adjoint problems, together with the gradient equation. The development of sensitivity and adjoint problems are discussed next.

The Sensitivity Problem. The solution of the direct problem (1) with thermal conductivity $k(T)$ unknown, can be recast as a problem of optimum control, that is, choose the control function $k(T)$ such that the following functional is minimized:

$$J[k(T)] \equiv \frac{1}{2}\int_{t=0}^{t_f}\sum_{m=1}^{M}\{T[x_m,t;k(T)] - Y_m(t)\}^2 dt \tag{3}$$

where M is the number of sensors and $Y_m(t)$ and $T[x_m,t;k(T)]$ are the measured and estimated temperatures, respectively, at a location x_m in the medium. If an estimate is available for $k(T)$, the temperature $T[x_m,t;k(T)]$ can be computed from the solution of the direct problem given by Eqs. (1).

In order to develop the sensitivity problem, we assume that the thermal conductivity $k(T)$ is perturbed by an amount $\varepsilon\Delta k(T$. Then, the temperature $T(x,t)$ undergoes a variation $\varepsilon\Delta k(T (x,t)$, that is,

$$T_\varepsilon(x,t) = T(x,t) + \varepsilon\Delta T(x,t) \tag{4.a}$$

where ε is a real number.

Due to the nonlinear character of the problem, the perturbation of temperature causes variations on the temperature-dependent quantities including the thermal conductivity, that is,

$$k_\varepsilon (T_\varepsilon) = k(T + \varepsilon\Delta T) + \varepsilon\Delta k(T) \approx k(T) + \left(\frac{dk}{dT}\right)\varepsilon\Delta T + \Delta k(T) \tag{4.b}$$

$$C_\varepsilon (T_\varepsilon) = C(T + \Delta T) \approx C(T) + \left(\frac{dC}{dT}\right)\varepsilon\Delta T \tag{4.c}$$

$$g_\varepsilon (T_\varepsilon) = g(T + \varepsilon\Delta T) \approx g(T) + \left(\frac{dg}{dT}\right)\varepsilon\Delta T \tag{4.d}$$

For convenience in the subsequent analysis, the differential equation (1.a) of the direct problem is written in operator form as

$$D(T) \equiv C(T)\frac{\partial T(x,t)}{\partial t} - \frac{\partial}{\partial x}\left[k(T)\frac{\partial T}{\partial x}\right] - g(T) = 0 \tag{5.a}$$

and the perturbed form of this equation becomes

$$D_\varepsilon (T_\varepsilon) \equiv C_\varepsilon (T_\varepsilon)\frac{\partial T_\varepsilon(x,t)}{\partial t} - \frac{\partial}{\partial x}\left[k_\varepsilon (T_\varepsilon)\frac{\partial T_\varepsilon}{\partial x}\right] - g_\varepsilon (T_\varepsilon) = 0 \tag{5.b}$$

To develop the sensitivity problem, we apply a limiting process for the differential equations (5.a,b) in the form

$$\lim_{\varepsilon \to 0} \frac{D_\varepsilon (T_\varepsilon) - D(T)}{\varepsilon} = 0 \tag{6}$$

and similar limiting processes are applied for the boundary and initial conditions (1.b-d) of the direct problem. After some manipulations, the following sensitivity problem results for the determination of the sensitivity function $\Delta T(x,t)$:

$$\frac{\partial (C\Delta T)}{\partial t} - \frac{\partial^2 (k\Delta T)}{\partial x^2} - \frac{\partial}{\partial x}\left(\Delta k\frac{\partial T}{\partial x}\right) - \frac{dg}{dT}\Delta T = 0 \quad \text{in} \quad 0 < x < L; t > 0 \tag{7.a}$$

$$\frac{\partial (k\Delta T)}{\partial x} = 0 \quad \text{at } x=0; t>0 \tag{7.b}$$

$$\frac{\partial (k\Delta T)}{\partial x} = -\frac{\Delta k}{k}\phi_L \quad \text{at } x=L; t>0 \tag{7.c}$$

$$\Delta T = 0 \quad \text{for } t = 0; \text{in } 0 < x < L \tag{7.d}$$

where $C \equiv C(T)$, $k \equiv k(T)$, $\Delta T \equiv \Delta T(x,t)$, $g=g(T)$ and $\Delta K \equiv \Delta K(T)$.

The Adjoint Problem and the Gradient Equation. To derive the adjoint problem and the gradient equation, we multiply equation (1.a) by the Lagrange Multiplier $\lambda(x,t)$ and integrate over the time and space domains. The resulting expression is then added to the functional given by equation (3) to obtain

$$J[k(T)] = \frac{1}{2}\int_{x=0}^{L} \int_{t=0}^{t_f} \sum_{m=1}^{M} (T-Y)^2\delta(x-x_m)\,dtdx +$$

$$\int_{x=0}^{L} \int_{t=1}^{t_f} \left[C(T) \frac{\partial T(x,t)}{\partial t} - \frac{\partial}{\partial x}\left[k(T)\frac{\partial T}{\partial x}\right] - g(T)\right] \lambda(x,t)\, dtdx \tag{8}$$

where $\delta(\bullet)$ is the Dirac delta function.

The directional derivative of the functional $J[k(T)]$ in the direction of the perturbation $\Delta T(T)$, is defined as (Jarny et al, 1991):

$$D_{\Delta k} J[k(T)] = \lim_{\varepsilon \to 0} \frac{J[k_\varepsilon(T_\varepsilon)] - J[k(T)]}{\varepsilon} \tag{9}$$

where the term $J[k_\varepsilon(T_\varepsilon)]$ is obtained by writing Eq. (8) for the perturbed quantities given by Eqs. (4). This derivative is allowed to go to zero and after some manipulations, the following adjoint problem is obtained for the determination of the Lagrange multiplier $\lambda(x,t)$:

$$-C\frac{\partial \lambda}{\partial t} - k\frac{\partial^2 \lambda}{\partial x^2} - \frac{dg}{dT}\lambda + \sum_{m=1}^{M} (T-Y)\delta(x-x_m) = 0 \quad \text{in } 0<x<L; t>0 \tag{10.a}$$

$$\frac{\partial \lambda}{\partial x} = 0 \quad \text{at } x=0; t>0 \tag{10.b}$$

$$\frac{\partial \lambda}{\partial x} = 0 \quad \text{at } x=L; t>0 \tag{10.c}$$

$$\lambda = 0 \quad \text{for } t=t_f; \text{ in } 0<x<L \tag{10.d}$$

Such limiting process also gives the gradient equation for the functional which takes the form

$$J'[k(T)] = \frac{\partial T}{\partial x}\frac{\partial \lambda}{\partial x} \tag{11}$$

The sensitivity function $\Delta T(x,t)$ obtained from the solution of problem (7) and the gradient of the functional given by Eq. (11) are used in the conjugate gradient method of minimization as discussed next.

The Conjugate Gradient Method of Minimization. The iterative procedure for the determination of the thermal conductivity is taken as (Jarny et al., 1991):

$$k^{p+1}(T) = k^p(T) - \beta^p d^p(T) \tag{12}$$

and the direction of descent $d^p(T)$ is given by:

$$d^p(T) = J'[T, k^p(T)] + \gamma^p d^{p-1}(T) \tag{13}$$

where the superscript "p" denotes the number of iterations and the conjugation coefficient γ^p is determined from:

$$\gamma^p = \frac{\int_{x=0}^{L} \int_{t=0}^{t_f} \{J'[T; k^p(T)] - J'[T; k^{p-1}(T)]\}J'[T; k^p(T)]\, dtdx}{\int_{x=0}^{L} \int_{t=0}^{t_f} \{J'[T; k^{p-1}(T)]\}^2 dtdx} \tag{14}$$

for p=1,2,...with $\gamma^0 = 0$

The coefficient β^p, which determines the step size in going from iteration p to p+1 in Eq. (12), is obtained by minimizing $J[k^{p+1}(T)]$ given by Eq. (3) with respect to β^p. After some manipulations the following expression is obtained

$$\beta^p = \frac{\displaystyle\int_{t=0}^{t_f} \sum_{m=1}^{M} \left[T(x_m,t;k^p) - Y_m(t) \right] \Delta T(x_m,t;d^p)\, dt}{\displaystyle\int_{t=0}^{t_f} \sum_{m=1}^{M} \left[\Delta T(x_m,t;d^p) \right]^2 dt} \tag{15}$$

where $\Delta T(x_m, t; d^p)$ is the solution of the sensitivity problem at position x_m and time t, which is obtained from Eqs. (7) by setting $\Delta k(T) = d^p(T)$.

Once $d^p(T)$ is computed from Eq. (13) and β^p from Eq. (15), the iterative process defined by Eq. (12) can be applied to determine $k^{p+1}(T)$, until a specified stopping criterion based on the discrepancy principle described below is satisfied.

The Stopping Criterion. If the problem involves no measurements errors, the traditional check condition specified as

$$J[k^{p+1}(T)] < \varepsilon_J \tag{16}$$

where ε_J is a small specified number, can be used. However, the observed temperature data contains measurement errors; as a result, the inverse solution will tend to approach the perturbed input data and the solution will exhibit oscillatory behaviour as the number of iterations in increased. The computational experience shows that it is advisable to use the discrepancy principle to stop the iteration process. Thus, by assuming

$$T[x_m,t;k(T)] - Y_m(t) \approx \sigma = \text{constant} \tag{17}$$

ε_J is obtained from Eq. (3) as:

$$\varepsilon_J = \frac{M}{2}\sigma^2 t_f \tag{18}$$

where σ is the standard deviation of the measurement errors.

Hence, Eq. (16) with ε_J determined from Eq. (18) is used to stop the iterations.

The Computational Algorithm. The algorithm for the iterative scheme given the conjugate gradient method is summarized below.

Suppose $k^p(T)$ is available at iteration p, then:

Step 1. Solve the direct problem given by Eqs. (1) and compute $T(x,t)$;

Step 2. Check the stopping criterion given by Eq. (16) with ε_J determined from equation (18). Continue if not satisfied;

Step 3. Knowing $T(x_m,t;k^p)$ and $Y_m(t)$, solve the adjoint problem given by Eq. (10) to obtain $\lambda(x,t)$;

Step 4. Knowing $\lambda(x,t)$, compute the gradient of the functional from equation (11);

Step 5. Knowing $J'[T,k^p(T)]$, compute first the conjugation coefficient from Eq. (14) and then the direction of descent from equation (13);

Step 6. Solve the sensitivity problem given by Eqs. (7) by setting $\Delta k(T) = d^p(T)$, to determine $\Delta T(x,t)$;

Step 7. Knowing $\Delta T(x_m,t;d^p)$, compute the search step size β^p from Eq. (15);

Step 8. Knowing β^p and $d^p(T)$, compute he new estimate $k^{p+1}(T)$ from Eq. (12) and go to step 1.

Results and Discussion

In order to examine the accuracy of the function estimation approach using the conjugate gradient method as applied to the analysis of the inverse problem previously described, we studied test cases by using simulated measured temperatures as the input data for the inverse analysis. The simulated temperature data were generated by solving the direct problem for a specified thermal conductivity. The temperatures calculated in this manner are considered exact measurements, T_{ex}, and

the simulated measured temperature data, Y, containing measurement errors, are determined as

$$Y = T_{ex} + \alpha\sigma \qquad (19)$$

where α is the error term and σ is the standard deviation of the measurements. For normally distributed errors, with zero mean and a 99% confidence level, α lies within the range

$$-2.576 < \alpha < 2.576 \qquad (20)$$

The values of α were randomly determined with the subroutine DRNNOR from the IMSL (1987).

To generate the simulated measurements, the direct problem given by Eqs. (1) was expressed in dimensionless form by introducing the following dimensionless variables:

$$\theta = \frac{T - T_0}{\dfrac{\phi_L}{k_0}L}; \Gamma = \frac{g(T)L}{\phi_L}; \tau = \frac{k_0 t}{L^2 C_0}; \eta = \frac{x}{L}; \Phi = \frac{q}{\phi_L} \qquad (21.\text{a-e})$$

and by taking the coefficients k(T) and C(T) as

$$k(T) = k_0 \kappa(\theta) \quad \text{and} \quad C(T) = C_0 \chi(\theta) \qquad (22)$$

where k_0 and C_0 are constants and have the units of k(T) and C(T), respectively; $\kappa(\theta)$ and $\chi(\theta)$ are dimensionless functions of θ; T_0 is the initial temperature in the medium which is assumed to be uniform; and ϕ_L is the heat flux applied at the boundary x=L, which is assumed to be constant.

For all test cases analyzed here, we considered $\sigma = 0$ (errorless measurements) and $\sigma = 0.01$ θ_{ma}, where θ_{ma} is the maximum temperature measured by the sensor. The sensor was located at $\eta = 0.8$ and, for sake of simplicity, we used $\Gamma(\theta) = 0$ and $\chi(\theta) = 1$.

Figure 1 shows the results for two different polynomial variations of the dimensionless thermal conductivity. Clearly, the agreement between the estimated and the exact thermal conductivities is very good, for both situations of errorless and inexact measurements, and such was the case for the other smooth functional forms tested.

Figure 2 shows similar results for a thermal conductivity with a triangular variation. A comparison of the exact thermal conductivity with the one estimated by using errorless measurements ($\sigma = 0$) indicates that the present function estimation approach can resolve sharp corners. The agreement between the exact solution an the results obtained by using measurements with random errors is good.

Figure 3 presents the results obtained for a step variation of the thermal conductivity. The curve obtained with errorless measurements ($\sigma = 0$) is in good agreement with the exact solution, although some oscillations are observed near the discontinuities. The results obtained by using measurements with random errors is also in good agreement with the exact functional form of the thermal conductivity.
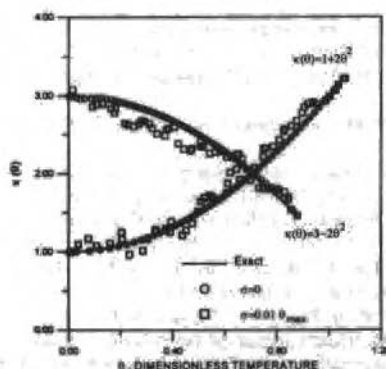

Fig. 1　Inverse solution with polynomial variation for the thermal conductivity
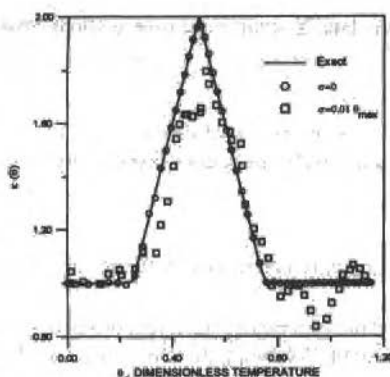
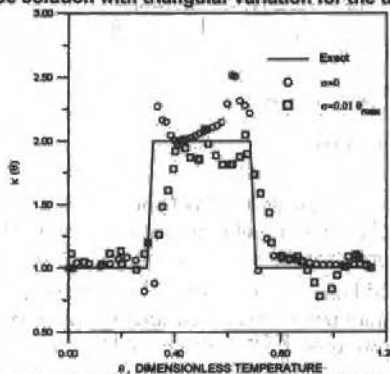Fig. 2   Inverse solution with triangular variation for the thermal conductivity

Fig. 3   Inverse solution with step variation for the thermal conductivity

Conclusions

The inverse analysis utilizing the conjugate gradient method of minimization with adjoint equation, provides an efficient approach for estimating the temperature dependence of thermal conductivity, with no prior information on the functional form of the unknown quantity.

Results obtained with test cases using simulated measurements with random errors indicate that the present approach is accurate, even for thermal conductivities with functional forms involving sharp corners and discontinuities.

References

Artyukhin, E.A., 1975, "Determination of Thermal Diffusivity from Experimental Data," J. Engr. Phys., Vol. 29, pp. 878-881.

Artyukhin, E.A., 1982, "Recovery of the Temperature Dependence of the Thermal Conductivity Coefficient from the Solution of the Inverse Problem," High Temp., Vol. 19, pp.698-702.

Artyukhin, E.A., and Nenarokomov, A.V., 1987, "Coefficient Inverse Heat-Conduction Problem," J.Engr. Phys., Vol. 53, pp. 1085-1090.

Goryachev, A.A., and Yudin, V.M., 1981, "Solution of the Inverse Coefficient Problem of Heat Conduction," J.Engr. Phys. Vol. 43, pp.1148-1154.

IMSL Library Edition 10.0, 1987, User's Manual Math Library, Houston, Texas.

Jarny, Y., Delaunay, D., and Bransier, J., 1986, "Identification of Nonlinear Thermal Properties by an Output Least Square Method," Proceedings, 8th International Heat Transfer Conference, pp. 1811-1816.

Jarny, Y., Ozisik, M.N., and Bardon, J.P., 1991, "A general Optimization Method using Adjoint Equation for Solving Multidimensional Inverse Heat Conduction," Int. J. Heat Mass Transfer, Vol. 34, pp. 2911-2929.

Mikhailov, V.V., 1989, "Arrangement of the Temperature Measurement Points and Conditionality of Inverse Thermal Conductivity Problem," J. Engr. Phys., Vol. 57, pp. 1369-1373.

Orlande, H.R.B., and M.N. Ozisik, 1993, "Determination of the Reaction Function in a Reaction-Difusion Parabolic Problem," Proceedings of First International Conference in Inverse Problems in Engineering: Theory and Practice, pp. 117-124, Palm Coast, Fl.

Hidrodinâmica em Tubos com Obstruções Curvilíneas

Hidrodynamics in Tubes with Curvilinear Obstructions

Luis Fernando G. Pires
Instituto de Projetos Especiais - CTEx
Av. das Américas, 28705
23020, Guaratiba - R.J.

Angela O. Nieckele
Pontifícia Universidade Católica do Rio de Janeiro
Departamento de Engenharia Mecânica
22453-900 - Rio de Janeiro

Abstract

A numerical study of the flow field in ducts with curvilinear obstruction was performed. A wide range of Reynolds was investigated. Velocity and pressure distribution were obtained by a finite volume method with non-orthogonal coordinate system. Comparision with available numerical and experimental results showed good agreement.
Keywords: Ducts, Curvilinear Obstruction, Finite Volume Method, Non-Orthogonal Coordinate System, Flow Field.

Resumo

Para obter maiores informações sobre escoamentos em tubulações com restrições curvilíneas, foi realizada uma análise numérica do problema, visando obter os campos de velocidade e pressão e as dimensões da região de deslocamento. Para este trabalho utilizou-se uma metodologia de solução de escoamentos em geometrias complexas, numa formulação incompressível e bidimensional. As equações de conservação foram discretizadas com o emprego da técnica de volumes finitos em coordenadas não ortogonais. Os resultados obtidos foram comparados com valores numéricos e experimentais existentes apresentando boa concordância.
Palavras chave: Tubulações, Restrições Curvilíneas, Volumes Finitos, Coordenadas Não Ortogonais, Campo de Velocidades.

Introdução

A análise de escoamentos em tubulações com restrições é de grande importância para áreas bem diversas, como a biomédica e a petrolífera. Nesta última, a existência de restrições, causadas principalmente por cordões de solda em tubos de pequeno diâmetro, provoca uma maior corrosão localizada logo após a restrição (Fisher, 1981). Já na área médica, a oclusão de artérias causada por placas escleróticas torna-se um dos maiores problemas do sistema circulatório. Neste caso, além de influir no próprio processo de crescimento da placa, os fatores hidrodinâmicos que surgem por causa da restrição, como a maior resistência ao fluxo sanguíneo e a variação da tensão de cisalhamento junto a parede arterial, estão associados a sérias disfunções do sistema circulatório (Wesolowski et al., 1965).

Para obter maiores informações sobre este processo, Young e Tsai (1973) realizaram um estudo experimental com o objetivo de determinar o ponto de separação e de recolamento do escoamento em função do tipo de restrição e do número de Reynolds. Também foi investigada a perda de pressão e a transição do escoamento de laminar para turbulento. A faixa do número de Reynolds investigada foi de 100 à 3000. Deshpande e Giddens (1980) realizaram experimentos para esta geometria com o número de Reynolds igual a 15000, apresentando o perfil de velocidade para diversas seções do tubo. Um estudo numérico com o objetivo básico de investigar o fenômeno em tubos soldados foi realizado por Rastogi (1984). Este empregou um método baseado em coordenadas ortogonais que se adaptam ao contorno, apresentando resultados para o caso turbulento, onde foi empregado o modelo $k - \varepsilon$. Karki e Patankar (1986) apresentam uma solução numérica com o emprego de coordenadas não ortogonais sendo os componentes covariantes utilizados como variáveis

dependentes. Este trabalho fornece somente alguns pontos referentes a dimensão da região de recirculação para o caso laminar. Desta forma pretende-se com este trabalho complementar a análise do problema, fornecendo dados numéricos não apresentados nos trabalhos citados.

O estudo teórico realizado utiliza a solução numérica das equações diferenciais de conservação de massa e quantidade de movimento em coordenadas generalizadas em situações axisimétricas. Os componentes contravariantes da velocidade são utilizados como variáveis dependentes da equação de conservação de quantidade de movimento.

Geometria do Problema e Malha Empregada

A Fig. 1 determina as principais dimensões da geometria estudada. Nesta, a restrição é definida por um cosseno da seguinte forma:

$$\frac{R}{R_0} = 1 - \frac{\delta}{2R_0}\left(1 + \cos\frac{\pi x}{X_0}\right) \tag{1}$$

para $-X_0 \leq x \leq X_0$, onde:

X_0 é a metade do comprimento da restrição;

δ é a altura da restrição;
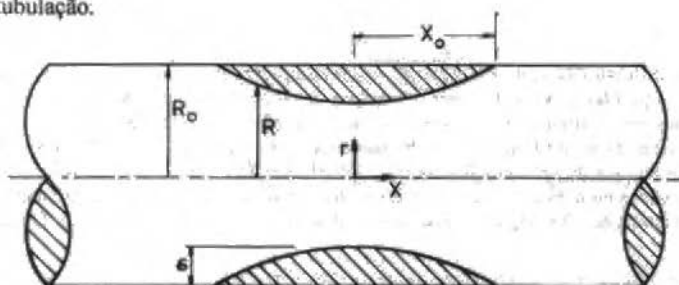
R_0 raio da tubulação.

Fig. 1   Geometria do problema

Foram analisadas quatro tipos de restrições como definidas na tabela abaixo:

Tab. 1   Parâmetros geométricos

Modelo	R_0 (mm)	δR_0	X_0/R_0
M1	9,5	1/3	4
M2	9,5	2/3	4
M3	9,5	2/3	2
M4	25,4	1/2	2

Desta forma o modelo M1 representa uma restrição suave e o modelo M3 representa uma restrição acentuada (89% de redução da área) num pequeno comprimento.

Fig. 2   Malha utilizada

O domínio computacional foi dividido em 40x12 pontos nodais com uma maior concentração de pontos na região do estrangulamento e um espaçamento maior na região de saída. A Fig. 2 apresenta parte da malha utilizada na região da restrição. Para a geração desta malha foi empregada uma técnica algébrica com controle do espaçamento das linhas.

Equações e Método de Solução

As equações que caracterizam o problema são:
continuidade

$$\nabla \cdot \vec{u} = 0 \qquad (2)$$

quantidade de movimento

$$\nabla \cdot (\rho (\vec{u}\vec{u})) = -\nabla p + \nabla \cdot \left(\mu_{eff}\left(\nabla \vec{u} + \left[\nabla \vec{u}\right]^{T}\right)\right) + S_{\vec{u}} \qquad (3)$$

onde μ_{ef} é chamada de viscosidade efetiva. Para regime laminar $\mu_{eff} = \mu$ e para regime turbulento $\mu_{eff} = \mu + \mu_t$, onde $\mu_t = C_\mu \rho k^2/\varepsilon \cdot C_\mu$ é uma constante empírica.

conservação da energia cinética turbulenta

$$\nabla \cdot (\rho \vec{u} k) = \nabla \cdot (\mu_t/Pr_k \nabla k) + G - \rho \varepsilon \qquad (4)$$

sendo G o termo de produção de energia cinética definido por:

$$G = \mu_t (\nabla \vec{u} + (\nabla \vec{u})^{T}) \nabla \vec{u} \qquad (5)$$

conservação da dissipação da energia cinética turbulenta

$$\nabla \cdot (\rho \vec{u} \varepsilon) = \nabla \cdot (\mu_t/Pr_\varepsilon \nabla \varepsilon) + C_1 \varepsilon/k G - C_2 \rho \varepsilon^2/k \qquad (6)$$

sendo Pr_g, Pr_k, C_1 e C_2 constantes empíricas do modelo. Os valores recomendados por Launder e Spalding (1974) são:

$$C\mu = 0,09 \quad C_1 = 1,44 \quad C_2 = 1,92 \quad Pr_g = 1,3 \quad Pr_k = 1,0$$

A metodologia desenvolvida primeiramente transforma a equação de conservação para uma variável genérica ϕ , para um sistema de coordenadas não ortogonais bi-dimensional (ξ, η), assumindo a simetria angular. Esta equação é posteriormente discretizada utilizando a técnica de volumes finitos, sendo o valor de ϕ nos pontos nodais obtido por interpolação, de acordo com o esquema "Power law" (Patankar, 1980). A expressão final pode ser escrita como:

$$a_p \phi_p = a_E \phi_E + a_W \phi_W + a_S \phi_S + a_N \phi_N + b \qquad (7)$$

onde a_E, a_W a_S , etc. representam a relação entre os coeficientes de difusão e convecção e b inclui todos os termos calculados explicitamente, inclusive os termos fonte e termos devido a não ortogonalidade da malha.

A equação de conservação de quantidade de movimento requer um tratamento diferenciado devido a presença do gradiente de pressão no termo fonte, além de outros fatores. Para a presente formulação, optou-se por utilizar uma malha deslocada para a velocidade e componentes contravariantes como variáveis dependentes destas equações. De modo a evitar o emprego da análise

tensorial e a manipulação dos diversos termos existentes nesta equação provenientes da curvatura e da não ortogonalidade da malha, foi empregada a abordagem do sistema de coordenada fixo localmente. Os detalhes deste desenvolvimento podem ser encontrados em Pires (1994). O acoplamento pressão-velocidade foi realizado pelo algoritmo SIMPLEC (VanDoormaal e Raithby, 1984). Para a solução do sistema algébrico resultante, foi utilizado o algoritmo TDMA linha a linha.

Condições de contorno

Para os cálculos utilizou-se um pequeno comprimento reto no início do domínio e, após a restrição, um comprimento reto maior para que a condição de contorno de saída de difusão desprezível pudesse ser empregada. Na entrada, para o caso laminar, utilizou-se um perfil desenvolvido parabólico. Para as paredes empregou-se o critério de não deslizamento e na linha central foi considerada a simetria do problema.

Para o caso turbulento, o perfil de velocidades na entrada foi medido por Deshpande e Giddens (1980), e pode ser representado pela lei da potência de 1/n, sendo o expoente "n" que caracteriza o perfil igual a 6,4. Os valores da energia cinética turbulenta e de sua dissipação na entrada foram calculadas segundo as expressões abaixo (Habib e Whitelaw, 1982):

$$k = 0,003 u_{max}^2 \quad e \quad \varepsilon = C_\mu k^{3/2}/0,03R_o \quad\quad (8)$$

O modelo de turbulência $k - \varepsilon$ só é válido no núcleo turbulento, onde $\mu_t \gg \mu$. Nas regiões próximas aos contornos sólidos, onde $\mu_t \ll \mu$ foi utilizada a lei da parede descrita por Patankar e Spalding, (1970). Assim, a velocidade paralela e imediatamente próxima à parede é calculada admitindo o perfil universal de velocidade. O valor da dissipação não é calculado nos pontos próximos a parede, mas obtidos pela hipótese de condição de equilíbrio entre a geração e a dissipação da energia cinética turbulenta (Pires, 1994).

Resultados

Apesar de escoamento se apresentar instável após a restrição e posteriormente turbulento para baixos números de Reynolds segundo Young e Tsai (1973), o presente trabalho utilizou o modelo laminar para Re até 2000 (onde o escoamento ainda é laminar na entrada).

A perda de pressão Δp através de uma obstrução de comprimento L é função da geometria e do número de Reynolds, $Re = 2\rho Ro\bar{u}/\mu$, onde $\bar{u}$ é a velocidade média. Os resultados obtidos para a perda de pressão adimensional em função do número de Reynolds estão apresentados na Fig. 3.

Nesta também são apresentados os resultados experimentais obtidos por Young e Tsai (1973). Para a comparação dos resultados, a distância entre os pontos de medida de pressão foi mantida igual a 32Ro. Pode-se observar que o comprimento da restrição altera muito pouco a perda de carga (casos M2 e M3). Por outro lado, a variação na área de restrição (casos M1 e M2) produz diferenças na perda de pressão de mais de dez vezes. O caso M4, com restrição intermediária, apresenta também queda de pressão intermediária.

A Fig. 4 ilustra a distribuição de pressão na parede ao longo da restrição, para Re=200. Observa-se que a pressão cai bruscamente na região de máxima restrição, sendo recuperada parcialmente após esta seção. Pode-se observar claramente que a queda de pressão é maior com o aumento da restrição.

A Fig. 5 ilustra o perfil de velocidades para o plano x/Xo = 0 para os casos M1, M2, M3 e M4 para o caso laminar (Re = 200). Pode-se observar para o caso M1 uma ligeira alteração do perfil parabólico. Porém, com o aumento da restrição verifica-se que o perfil de velocidade tende a ficar mais uniforme, com a velocidade máxima cada vez mais próxima da parede.
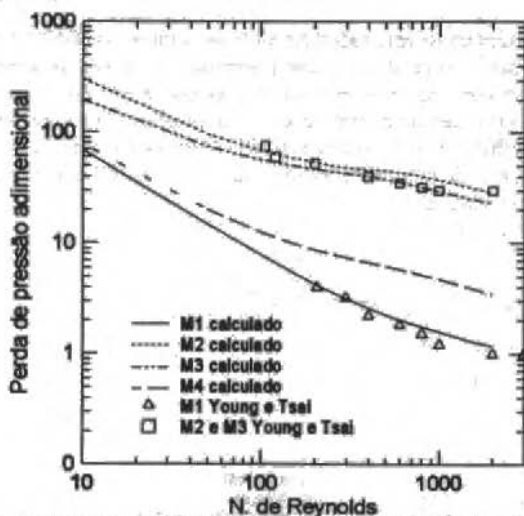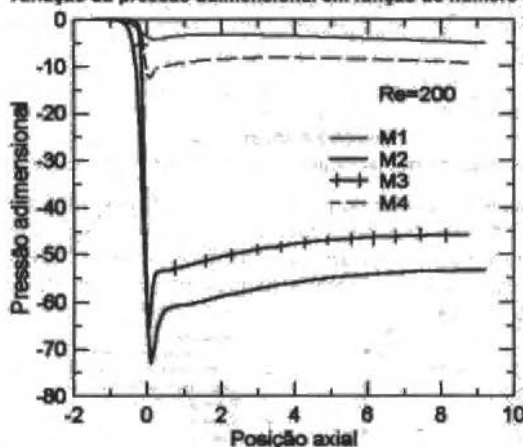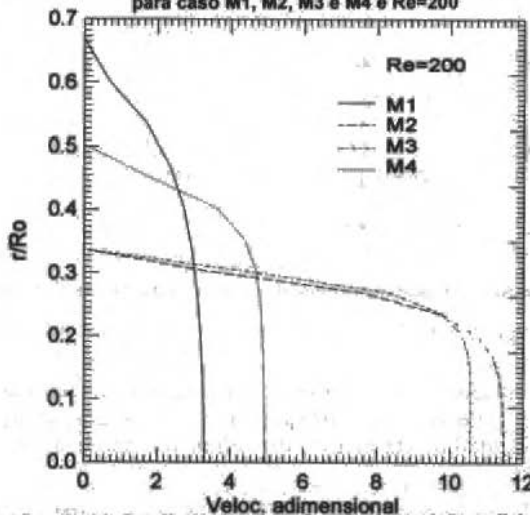
Fig. 3   Variação da pressão adimensional em função do número de Reynolds

Fig. 4   Variação da pressão adimensional na parede em função da posição,
para caso M1, M2, M3 e M4 e Re=200

Fig. 5   Variação da velocidade adimensional em função da posição radial para Re=200 (x/Xo = 0)

As Figs. 6 e 7 apresentam os resultados para o caso turbulento (Re = 15000) para a geometria M4. A variação da pressão adimensional na parede ilustrada na Fig. 6 apresenta um comportamento bem semelhante ao caso laminar. Observa-se uma boa concordância com o resultado numérico de Rastogi (1984), porém a recuperação de pressão prevista numericamente é muito maior que a medida experimentalmente por Deshpande e Giddens (1980). A falha na predição deste fenômeno está associada ao modelo k – ε, que de maneira geral não apresenta um bom desempenho na presença de grandes acelerações e de recirculações.
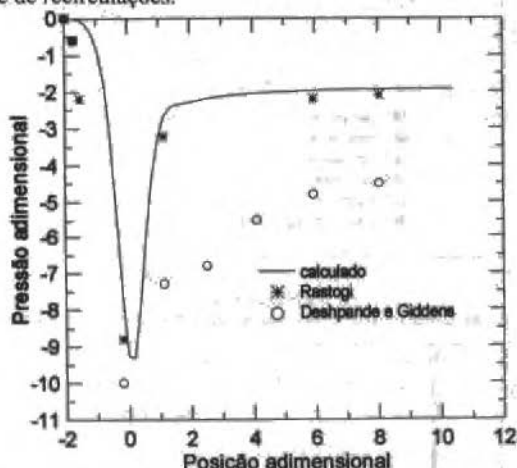
Fig. 6   Variação da pressão adimensional na parede em função da posição, para caso M4 e Re=15000

A Fig. 7 apresenta os resultados do perfil de velocidade para os planos x/Xo = 0, x/Xo = 2 e x/Xo = 11. Observa-se novamente uma boa concordância com os resultados numéricos de Rastogi (1984). Porém, para o plano x/Xo = 2, logo após a restrição, observa-se claramente, pelas velocidades negativas, uma região de recirculação muito maior do que o previsto numericamente.
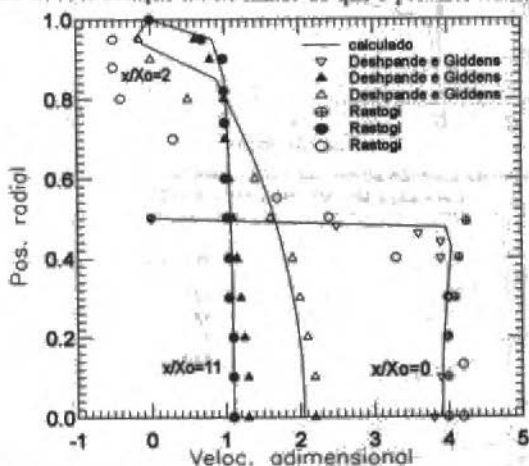

Fig. 7   Variação da velocidade adimensional em função da posição radial r/Ro

Afastado desta região, o modelo volta a apresentar bons resultados, como verificado para o plano x/Xo = 11.

Os presentes resultados corroboram as informações obtidas por Rastogi (1984) de que o modelo k – ε utilizado é incapaz de prever precisamente o comprimento da região de descolamento. Para a obtenção destes resultados, um modelo de turbulência capaz de prever a anisotropia do escoamento, deve ser usado.

Para a faixa laminar, o comprimento da recirculação foi bem capturado, como pode ser observado nas Figs. 8a e 8b, correspondentes aos modelos M2 e M3. Nestas figuras o comprimento da região de recirculação está como função do número de Reynolds. A distância horizontal entre dois pontos da curva fornece o comprimento da região de recirculação. Na Fig. 8a (caso M2) estão apresentados alguns pontos numéricos obtidos por Karki (1988) e Rastogi (1984) que apresentam boa concordância com os valores obtidos. Em relação aos dados experimentais, o comprimento da região de recirculação é ligeiramente subestimado.

Já para o modelo M3, apresentado na Fig. 8b, tem-se uma inversão da tendência observada para o modelo M2, isto é, o comprimento da região de recirculação foi superestimado. Assim, apesar da ligeira discrepância entre os resultados experimentais e os resultados numéricos, tem-se um bom resultado geral, o que fornece confiabilidade para os valores obtidos para o caso M4, para o qual não se tem dados experimentais.

Conclusões

Como mencionado na introdução, utilizou-se uma metodologia de cálculo empregando coordenadas não ortogonais que se adaptam ao contorno, em situação axi-simétrico. O estudo realizado cobriu uma larga faixa de escoamentos (número de Reynolds variando de 10 a 15000) de modo a complementar as informações de outros trabalhos. Sempre que disponíveis, dados experimentais ou numéricos foram realizados para validar estas informações. De maneira geral, pode-se afirmar que, no tocante a perda de carga, a variação da seção obstruída é muito mais importante que o comprimento desta região. Além disso, mesmo para o caso de pequena restrição (caso M1), a perda de carga é muitas vezes superior à existente num tubo sem obstrução. Já para a determinação das características da região de recirculação, tanto o comprimento como a porcentagem da seção reta obstruída são importantes. Para este caso, observou-se uma boa concordância com os dados experimentais na faixa laminar. Na faixa turbulenta, o comprimento da região de recirculação apresentou discrepância, devido à não adequação do modelo $k - \varepsilon$ à região de recirculação, uma vez que fora desta região os resultados foram bons.
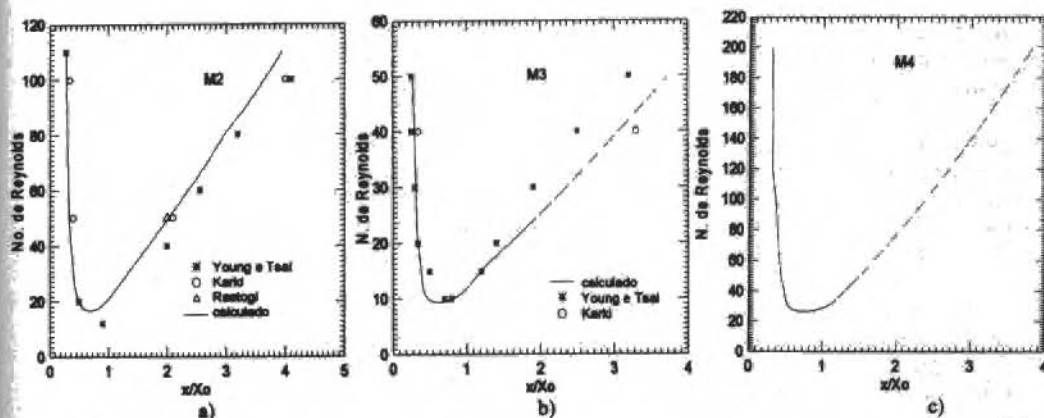

Fig. 8   Dimensão da região de descolamento para geometria M2, M3 e M4

Referências

Deshpande, M.D., and Giddens, D.P., 1980, "Turbulence Measurements in a Constricted Tube", J. Fluid Mechanics, Vol. 97, Part 1, pp.65-89.

Fisher, H.E., 1981, "Pipeline Operators Learning To Meet Offshore Challenges", Pipeline Industry, Abril pp. 69-72.

Habib, M.A., and Whitelaw, J.H., 1982, "The Calculation of Turbulent Flow in Wide-Angle Diffusers", Numerical Heat Transfer, Vol. 5, pp. 145-164,.

Karki, K.C., and Patankar, S.V., 1988, "Solution of Some Two-Dimensional Incompressible Flow Problems Using a Curvilinear Coordinate System Based Calculation Procedure", Numerical Heat Transfer, Vol. 14, pp. 309-323,.

Launder, B.E., and Spalding, D.B., 1972, "Mathematical Models of Turbulence", Academic Press, London,.

Launder, B.E., and Spalding, D.B., 1974, "The Numerical Computation of Turbulent Flows", Comp. Methods in App. Mechanics and Engineering, Vol. 3, pp. 269-289,.

Patankar, S.V., and Spalding, D.B., 1970, Heat and Mass Transfer in Boundary Layers, Intertex Books, London,.

Patankar, S.V., 1980, Numerical Heat Transfer and Fluid Flow, Hemisphere,.

Pires, L.F.G., 1994, "Um Método Numérico para Solução de Escoamentos Utilizando Componentes Contravariantes em Coordenadas não Ortogonais", Dissertaçãosão de Doutorado, PUC-RJ.

Rastogi, A.K., 1984, "Hydrodynamics in Tubes Perturbed by Curvilinear Obstructions", J. Fluids Engineering, Vol.106, pp. 22-269, Sept.

VanDoormaal, J.P., and Raithby, G.D., 1984, "Enhancements of the SIMPLE Method for Prediction Incompressible Fluid Flows", Numerical Heat Transfer, Vol. 7, pp. 147-163.

Young, D.F., and Tsai, F.Y., 1973, "Flow Characteristics in Models of Arterial Stenosis-I. Steady Flow", J. Biomechanics, Vol. 6, pp. 395-410.

Wesolowski, S.A., Fries, C.C., Sabina, A.M., and Sawyer, P.N., 1965, "Biophysical Mechanisms in Vascular Homeostasis and Intravascular Thrombosis", pp. 145-157, Appleton-Century-Croft, New York.

A Finite Volume Method Using Voronoi Grids for the Solution of Miscible Displacement in Porous Media

Clóvis Raimundo Maliska
Clóvis Raimundo Maliska Júnior
SINMEC - Computational Fluid Dynamics Laboratory
Mechanical Engineering Department - UFSC. - P.O. Box 476
88040-900 - Florianopolis - SC - Brazil

Abstract

The present work describes a numerical methodology for the solution of miscible displacement in porous media using unstructured Voronoi discretization. The Voronoi diagrams are an attractive alternative for approximating flow problems due to its construction, which forces grid points to be aligned with the normal of the control volume surfaces. The control volume approach is used and an hybrid scheme is employed as the interpolation function for the solution of a tracer injection in a single-phase flow in a five-spot arrangement. The numerical results are compared with the ones obtained with boundary-fitted grids and experimentally.
Keywords: Miscible Displacement, Porous Media, Finite Volume Method, Voronoi Grids

Introduction

The solution of miscible displacement in porous media is of great interest in petroleum engineering in the determination of the tracer flow in petroleum reservoirs. The injection of tracers is used to study the behaviour of the petroleum reservoirs, specially concerning with the preference of the flow in the porous rock. Usually small amounts of a tracer is injected in the water phase and the time for the tracer to reach the production wells is monitored. The previous analysis of the tracer concentration in the single-phase flow through the porous rock helps considerably the engineers to set up the experimental procedure.

Since small amounts are normally injected, the tracer pulse, in the numerical prediction, may be smeared by excessive numerical diffusion, prediction a shorter time for the breakthrough of the tracer. Therefore, one of the key questions is to have numerical algorithms which do not introduce excessive artificial diffusion.

The traditional methods in petroleum engineering, as reported by Aziz and Settari (1979), employ, in general, cartesian discretization. This coordinate system has the disadvantage of not conforming the reservoir boundaries, which are always of irregular shape. To by-pass this difficulty recent efforts are being made towards the development of methodologies which uses boundary-fitted grids, as reported in Roson (1989), Sharpe and Anderson (1991) and Maliska et alli (1991, 1992, 1993).

Another route which is also receiving attention, for by-passing the limitations of the cartesian discretization, is the use of unstructured grids. The construction of unstructured grids can be performed in different ways. Baliga and Patankar (1983), Raw and Schneider (1986), among others, uses to construct the control volume by joining the centroid and the median of the triangle side by a straight line. Forsyth (1989), Fung et alli (1991, 1993), Santos et alli (1991), have used this type of grid in petroleum reservoir simulation.

If the construction is done such that the line joining two grid points is normal to the control volume surface, the resulting control volume is called a Voronoi discretization. This type of discretization was used in several branches of physics and recently applied in petroleum reservoir engineering, as reported by Heinemann and Brand (1988), Heinemann et alli (1989, 1991), Palagi (1990, 1992) and Marcondes (1993).

This paper presents a numerical methodology for the solution of miscible displacement in porous media using Voronoi discretization. The control volume concept is employed and an hybrid scheme is used to interpolate the concentration at the control volume interfaces. The Voronoi diagrams are generated using the algorithm developed in Maliska Jr. (1993). The results obtained are compared with the ones obtained using boundary-fitted grids and experimentally.

The Problem Under Analysis

Consider a petroleum reservoir with a given porosity and volume where, through the injection well, is maintained a steady single phase flow. To this flow a tracer is added, with a given concentration, and one is interested in predicting the concentration distribution of the tracer along the reservoir, specially closed to the production wells. The phase here considered may be flowing together with other phases but, for the purpose of this work, this is immaterial. At the time t equals zero one starts to inject the tracer with a fixed concentration. The tracer and the fluid of the phase are miscible and, therefore, forms a single phase homogeneous mixture.

Governing Equations

The problem under analysis is the single phase flow in a porous media. Starting from the mass conservation given by

$$\frac{\partial}{\partial t}(\rho\phi) + \frac{\partial}{\partial x}(\rho u) + \frac{\partial}{\partial y}(\rho v) = \bar{q} \qquad (1)$$

where u and v are the cartesian velocity components, ρ the density and ϕ the porosity of the medium, combined with the Darcy's equation

$$\vec{V} = -\frac{k}{\mu}\nabla P \qquad (2)$$

one obtains the mass conservation equation written in terms of pressure as

$$\nabla \cdot (\nabla P) = \frac{1}{\alpha^*}\frac{\partial P}{\partial t} - \frac{\mu}{k}\bar{q} \qquad (3)$$

where $\bar{q}$ is the mass flow rate per unity of volume and α^* is given by

$$\alpha^* = \frac{k}{\mu\phi c_t} \qquad (4)$$

where μ is the viscosity, k the absolute permeability and c_t the compressibility coefficient.

In the present work all cases where run considering c_t equal to zero, but the term involving α^* in Eq. (3) is retained only for advancing the solution to steady state. To obtain the equation which governs the transient concentration of the tracer one needs to perform the mass conservation of the tracer. The resulting equation is

$$\frac{\partial}{\partial t}(\phi C) + \nabla \cdot (J + \vec{V}C) = \bar{q}C_i \qquad (5)$$

where J is given by

$$J = -\phi D\nabla C \qquad (6)$$

and C_i is the concentration at the injection well and D is the diffusion coefficient, given by

$$D = \alpha|\vec{V}| \qquad (7)$$

where $\vec{V}$ is the magnitude of the velocity vector normal to the control volume surface and α is the dispersion coefficient.

Discretized Equations

Equations (3) and (5) must be solved in an unstructured Voronoi grid as shown in Fig. 1. The control volume approach is used, whereby the conservation equations are integrated in the control volume P shown in Fig. 1. The most interesting feature of the Voronoi diagram for fluid flow problems, is the fact that the line joining the grid point P and the neighbouring grid point i is normal do the control volume surface and the intersection is exactly its mind point. This simplifies considerably all procedures which calculates fluxes along the normal.
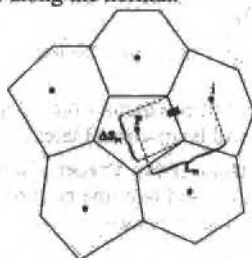
Fig. 1 Elemental control volume and its neighbours

Pressure Equation. The integration of Eq. (3) over time and space reads

$$\int_{V,t} \nabla \cdot (\nabla P) \, dV dt = \frac{1}{\alpha^*} \int_{V,t} \frac{\partial P}{\partial t} dV dt - \int_{V,t} \frac{\mu}{k} \bar{q} dV dt \qquad (8)$$

Using the divergence theorem one obtains

$$\int_{A,t} (\nabla P \cdot \hat{n}) \, dA dt = \frac{1}{\alpha^*} \int_{V,t} \frac{\partial P}{\partial t} dV dt - \int_{V,t} \frac{\mu}{k} \bar{q} dV dt \qquad (9)$$

Integrating Eq. (9) the algebraic equation for the control volume P is determined as

$$\sum_{i = interfaces} \{ (\nabla P \cdot \hat{n})_{Pi} \Delta S_{Pi} \} = \frac{1}{\alpha^*} (P_P^{n+1} - P_P^n) \frac{\Delta V}{\Delta t} - \frac{\mu}{k} \bar{q} \Delta V \qquad (10)$$

where the summation is performed for all interfaces of the control volume P. The subindex Pi denotes all information needed at the interface and related to the connection of control volume P and its neighbour i. Using Eq. (2) it is easy to show that the velocity normal to the control volume surface, aligned with the grid points, is given by

$$\frac{\partial P}{\partial \hat{n}}\bigg|_{Pi} \Delta S_{Pi} = -V_{Pi} \frac{\mu}{k} \qquad (11)$$

which is exactly the i term of the left hand side of Eq. (10). Discretizing Eq. (11) it reads

$$\frac{(P_i - P_p)}{L_{Pi}} \Delta S_{Pi} = -V_{Pi} \frac{\mu}{k} \qquad (12)$$

Using the Eq. (12) and Eq. (10) one obtains the discretized equation for the control volume P as

$$P_p^{n+1}\left(\frac{1}{\alpha^*}\frac{\Delta V}{\Delta t}+\sum_i\frac{\Delta S_{Pi}}{L_{Pi}}\right)=\sum_i P_i^{n+1}\frac{\Delta S_{Pi}}{L_{Pi}}+\frac{\Delta V P_p^n}{\alpha^*\Delta t}+\frac{\mu}{k}\bar{q}\Delta V \tag{13}$$

or

$$A_p P_p^{n+1}=\sum_i A_i P_i^{n+1}+B \tag{14}$$

where

$$A_p=\sum_i A_i+\frac{1}{\alpha^*}\frac{\Delta V}{\Delta t};\ A_i=\frac{\Delta S_{Pi}}{L_{Pi}} \tag{15}$$

Equation (14) is a linear system of equations which originates matrices which are not of fixed band. The solver for this linear system will be discussed later.

Equation for the Concentration of the Tracer. To obtain the discretized equation for the concentration, Eq. (5) is integrated in time and over the control volume shown in Fig. 1. Again using the divergence theorem the integrated equation results

$$\left[(\phi C)_P^{n+1}-(\phi C)_P^n\right]\frac{\Delta V}{\Delta t}+\sum_i\left(\frac{\phi D}{L}\right)_{Pi}(C_P-C_i)^{n+1}\Delta S_{Pi}$$

$$=-\sum_i(V_{Pi}C_{Pi})^{n+1}\Delta S_{Pi}+\bar{q}\Delta V C_P^{n+1} \tag{16}$$

where C_{Pi} represents the concentration at the interface of control volumes P and i. As can be seen by Eq. (16) the diffusive terms were approximated using central differences. For the convective terms one needs to interpolate the value of C_{Pi} at the interfaces from the values at the grid nodes P and i. To interpolate the concentration at the interfaces the WUDS of Raithby and Torrance (1974) is used. This scheme is widely employed with structure grids and its extension to this type of grid is straightforward. Therefore, the C_{Pi} at the interface is calculated by

$$C_{Pi}=\left(\frac{1}{2}+\alpha_{Pi}\right)C_P+\left(\frac{1}{2}-\alpha_{Pi}\right)C_i \tag{17}$$

where the α_p is obtained by

$$\alpha_{Pi}=\frac{Pe^2}{10+2Pe^2}$$

where the local Peclet number is given by

$$Pe=\frac{V_{Pi}L_{Pi}}{D_{Pi}} \tag{19}$$

It is to be noted that in spite of α_p to result always positive from Eq. (18), its sign is the same as the sign of the velocity. Therefore, considering again Fig. 1 it can be seen that when α_p tends to -0.5 (mass flow entering the volume), the C_{Pi} will be equal to C_i, that is an upwind scheme is employed. If mass leaves the control volume C_{Pi} will be equal to C_P. For other values of α C_{Pi} will depend on both C_p and C_i, that is, an hybrid scheme. It is worthwhile to mention that the interpolation function given by Eq. (17) is onedimensional and, therefore, even being hybrid, will case numerical diffusion. It is expected, however, less numerical diffusion than when this interpolation is applied to

cartesian or boundary-fitted grids. The explanation is that with unstructured grids one has randomly distributed interfaces with a larger number of neighbouring volumes, contributing for a better influence of these elements on the value of the function at the interface. The onedimensional interpolation function applied to unstructured grids would resemble the skew schemes applied to structured grids. Introducing Eq. (17) into Eq. (16) one obtains

$$
C_P^{n+1}\left[\frac{\phi\Delta V}{\Delta t} + \sum_i\left[\left(\frac{\phi D}{L}\right)_{Pi} + V_{Pi}\left(\frac{1}{2}+\alpha_{Pi}\right)\right]\Delta S_{Pi}\right] =
$$
$$
\sum_i\left[\left(\frac{\phi D}{L}\right)_{Pi} - V_{Pi}\left(\frac{1}{2}-\alpha_{Pi}\right)\right]\Delta S_{Pi}C_i^{n+1} + (\phi C)_P^n\frac{\Delta V}{\Delta t} + \bar{q}\Delta V C_P^{n+1} \tag{20}
$$

Introducing the mass conservation equation given by

$$
-\sum_i (V\Delta S)_{Pi} + \bar{q}\Delta V = 0 \tag{21}
$$

into the brackets which multiplies C_P^{n+1}, one obtains

$$
C_P^{n+1}\left[\frac{\phi\Delta V}{\Delta t} + \bar{q}\Delta V + \sum_i\left[\left(\frac{\phi D}{L}\right)_{Pi} - V_{Pi}\left(\frac{1}{2}-\alpha_{Pi}\right)\right]\Delta S_{Pi}\right] =
$$
$$
\sum_i\left[\left(\frac{\phi D}{L}\right)_{Pi} - V_{Pi}\left(\frac{1}{2}-\alpha_{Pi}\right)\right]\Delta S_{Pi}C_i^{n+1} + (\phi C)_P^n\frac{\Delta V}{\Delta t} + \bar{q}\Delta V C_P^{n+1} \tag{22}
$$

It is to be noted that the last term in the right hand side of Eq. (22) exists only in the injection and in the production wells. For the injection wells the value of C_P^{n+1} is known and will be added to the independent vector of the linear system. For the production wells it is unknown and, therefore, will join the A_P term, cancelling with the same value introduced by Eq. (21).

The resulting equation is

$$
A_i C_P^{n+1} = \sum_i A_i C_i^{n+1} + B \tag{23}
$$

with the following coefficients

$$
A_i = \left[\left(\frac{\phi D}{L}\right)_{Pi} - V_{Pi}\left(\frac{1}{2}-\alpha_{Pi}\right)\right]\Delta S_{Pi} \tag{24}
$$

$$
A_p = \sum A_i + \phi\frac{\Delta V}{\Delta t} + \bar{q}\Delta V \tag{25}
$$

$$
B = (\phi C)_P^n\frac{\Delta V}{\Delta t} + \bar{q}\Delta V C_p^{n+1} \tag{26}
$$

It is recalled that the last terms in Eqs. (25) and (26) are always zero, except for the injection wells.

Numerical Procedure

Since we are dealing with the injection of small amounts of tracer one is considering that it does not alter the viscosity of the phase. With this assumption the flow equation, Eq. (14), is decoupled from Eq. (23). The problem under consideration in this work is the injection of a tracer in a five-spot

pattern, as shown in Fig. 3. This geometry is chosen because numerical and experimental results are available. Of course, the methodology herein presented is general and can be applied to arbitrary reservoirs. An illustrative example of this situation will be shown when the results are reported.

For the solution of the linear system of equations the NS-ADI (Non-Structured Alternating Direction Implicit) method of Maliska Jr. and Bezerra (1994) is employed. The idea of the method is to have the same flexibility of the tridiagonal algorithms, extensively used for structure grids. To accomplish this the domain is swept along lines, solving a unidimensional problem for that volumes which were cut by the sweeping line. Figure 2 shows the dashed volumes which will enter the calculation for the sweeping line $A - A$. Actually the problem is solved along the zig-zag line shown in the Fig. 2 where a tridiagonal matrix is generated. The key question in this method is the algorithm for sweeping the domain, since no control volumes can be left behind during the sweeping. At the same time the sweeping step can not be too short since too many control volumes will be repeated, influencing considerably the convergence rate. These and other details of the solver can be found in Maliska Jr. and Bezerra (1994).
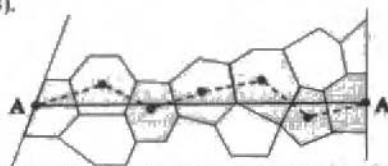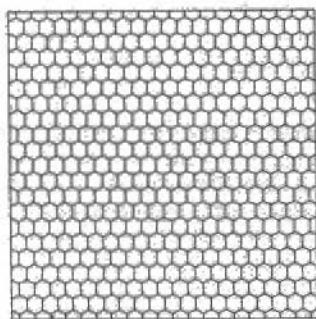

Fig. 2   Sweeping for the NS-ADI method

Fig. 3   Voronoi discretization employed

Numerical Results

Figure 3 shows the type of the Voronoi discretization used for the solution of the miscible displacement of tracers in a five-spot configuration, as depicted in Fig. 3. Grids with 431,946 and 1661 control volumes were used. These results were obtained with a very small time step. They are not reported here but the solution with 1661 volumes is already independent of the grid size and, therefore, all remaining results were run using this grid.
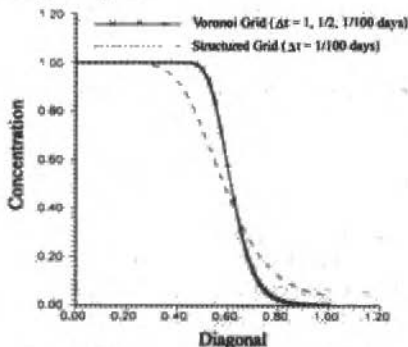

Fig. 4   Concentration along the diagonal

Figure 4 depict the concentration profiles along the diagonal for the time when 0.5 porous volume were injected. The profiles were obtained for Peclet number equal to 100, defined by

$$Pe = \frac{VL}{D\phi} \qquad (27)$$

and for different time steps. For example, the time step 1/2 means that the time step of 1 day (86400 s) was subdivided in 2 smaller time steps. It is clear that the solution using Voronoi grids shows much less numerical diffusion than the solution obtained with the boundary-fitted grid. Recalling Eq. (7) one sees that the Peclet number can be modified by altering the dispersivity, since the velocity is cancelled in the Peclet number due to its appearance in the diffusion coefficient.
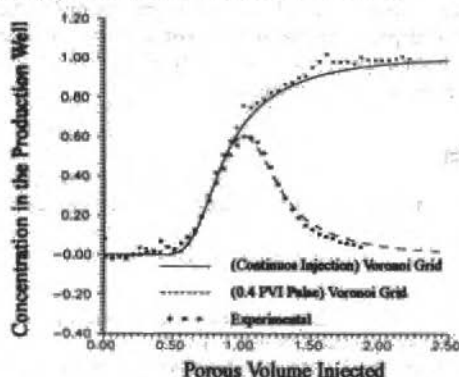
Fig. 5   Concentration at the production well

As a final application of the model the numerical results of the present work are compared with the ones reported by Santos et al (1992). Table 1 gives the data of the reservoir used in the experimental and numerical works. Figure 5 shows the tracer concentration at the production well for continuous injection and for a pulse of the tracer corresponding to 0.4 injected porous volume. Both results are very good.

Table 1   Data used in the simulation and experiment

	Simulation	Experiment
Dimension (m)	300 x 300	0.15 x 0.15
Permeability	200	519
Porosity (%)	20	17.75
Injected flow rate (m^3/s)	500	0.0041166
Dispersivity (m)	7.5	0.00115

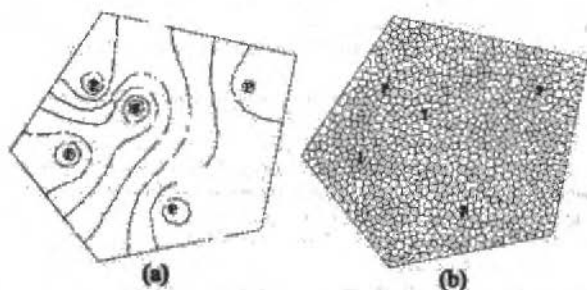(a)   (b)

Fig. 6   A general example - (a) Pressure field and (b) unstructure grid employed

Figure 6 shows the unstructured grid employed and the pressure field for two injection and tree production wells in an arbitrary reservoir, with the only goal of demonstrating the generally of the numerical model. A problem with any number of wells with any kind of boundary conditions in irregular shape reservoirs can be solved with the methodology described in this paper.

Conclusions

The use of unstructured grids, in conjunction with finite volume formulations, for the solution of fluid flow problems is becoming a very attractive alternative. Its flexibility in generating the grid with volumes with different sizes and shapes is useful for the situation where pontual sources exists, like the wells in petroleum reservoir simulation. The nature of the Voronoi diagrams facilitates the application of conservation laws, since all normals to the control volume surfaces are aligned with the grid points. The miscible displacement in a five-spot configuration was solved and the numerical results agreed very well with the experimental ones. The finite volume formulation developed is clean and general, allowing extension to more complex problems.

Acknowledgements

References

Baliga, B.R., and Patankar, S.V., 1983, " A Control-Volume Finite Element Method for Two-Dimensional Fluid-Flow and Heat Transfer", Numerical Heat Transfer, 6, pp. 245-261.

Fung, L.S.K., Buchaman, W.L., and Ravi Sharma, 1993, "Hybrid-CFFE Method for Flexible Grid Reservoir Simulation", Paper SPE 25266 presented in 12th Symposium on Reservoir Simulation, New Orleans, Feb. 28 - March 3.

Heinemann, Z.E., and Brand, C.W., 1988, "Gridding Construction for Reservoir Simulation", Paper presented in 1th Forum on Reservoir Simulation, Alpbach, Austria, Sep. 12-16.

Heinemann, Z.E., Gerken, G., and Hantelmann, G., 1983, "Using Grid Refinement in a Multiple-Application Reservoir Simulator", Paper SPE 12225 presented in 11th Symposium on Reservoir Simulation, San Francisco, Nov. 16-18.

Maliska, C.R., Silva, A.F.C., Marcondes, F., Lopes, M.N., and Cunha, A.R., 1991, "Numerical Solution of the Single-Phase Flow with a Tracer" (in portuguese), Report prepared to: CENPES/PETROBRAS S.A., Part I, September.

Maliska, C.R., Silva, A.F.C., Juca, P.C.S., Cunha, A.R., and Lopes, M.N., 1992, "Numerical Solution of the Two-Phase Oil/Water Flow" (in portuguese), Reporte prepared to: CENPES/PETROBRAS S.A., Part II, June.

Maliska, C.R., Silva, A.F.C., Juca, P.C.S., Cunha, A.R., and Livramento, M.A., 1993, "Development of a Three-Dimensional Black-oil Simulator Using Boundary-Fitted Coordinates" (in portuguese), Report prepared to: CENPES/PETROBRAS S.A., Part I, April.

Maliska Jr., C.R., 1993, "A Robust Voronoi Diagram Generator for Discretizing Irregular Domains" (in portuguese), XIV CILAMCE, São Paulo, S.P., December.

Maliska Jr., C.R., and Bezerra, L.H., 1994, "Solution of Linear Systems obtained in the Numerical Solution of Engineering Problems using Voronoi Diagrams" (in portuguese), Submitted for publications in the XVII CNMAC, Vitoria, Espirito Santo.

Marcondes, F., 1993, "Numerical Simulation of Petroleum Reservoir using Voronoi Meshes" (in portuguese), Ph.D. Proposal, Mechanical Engineering Department, UFSC.

Palagi, C., 1992, "Generation and Application of Voronoi Grid to Model Flow in Heterogeneous Reservoirs", Ph.D. Thesis, Stanford University, Satnford, May.

Raithby, G.D., and Torrance, K.E., 1967, "Upstream-weighted Differency Schemes and Their Application to Elliptic Problems Involving Fluif Flow", Computer and Fluids, 2, pp. 12-26.

Raw, M.J. and Schneider, G.E., 1986, "A Skewed Positive Influence Coefficient Upwinding Procedure for Control-Volume-Based Finite Element Convection-Diffusion Computation", Numer. Heat Transfer, 9(1), pp. 1-26.

Rozon, B.J., 1989, "A Generalized Finite Volume Discretization Method for Reservoir Simulation", Paper SPE 18414, 10th SPE Symposium on Reservoir Simulation, pp. 71-84.

Santos, R.L.A., Pedrosa Jr., O.A., and Correa, A.C.F., 1992, "An Efficient Finite-Volume Approach for Modelling Miscible Displacement", II Latin-American Petroleum Engineering Conference, Caracas, Venezuela, March.

Sharpe, H.N., and Anderson, D.A., 1991, "Orthogonal Curvilinear Grid Generation with Preset Internal Boundaries for Reservoir Simulation", Paper SPE 21235 presented in 11th SPE Symposium on Reservoir Simulation, Anaheim, Feb. 17-20.

Two-Dimensional Two-Phase Petroleum Reservoir Simulation Using Boundary-Fitted Grids

A. R. Cunha,

C. R. Maliska,

A. F. C. Silva,

M. A. Livramento

SINMEC - Computational Fluid Dynamics Laboratory

Mechanical Engineering Department - UFSC - P. O. Box 476 Cep: 88040-900 - Florianópolis - SC - Brazil.

Abstract

The present work introduces a numerical method, using boundary-fitted grids, for simulating petroleum reservoirs. Boundary-fitted meshes have the capability of conforming the irregular boundary of the reservoir, allowing better application of boundary conditions and facilitating the specification of geological faults. To assess the methodology, the well known five-spot problem is used, where comparisons using curvilinear, cartesian diagonal and parallel grids are done. To demonstrate the ability of the model, a reservoir of irregular shape, with 2 injection and 6 production wells, is simulated.

Keywords: Petroleum Reservoirs Simulation, Boundary-Fitted Grids

Introduction

The numerical simulation of petroleum reservoirs is of great importance in petroleum engineering because full experimental simulation in laboratory is impossible. The prediction of the flow of oil, gas and water in the porous rock may help very important technical and economical decisions about the reservoir, like the estimation of oil production, estimation of production time, etc. Nowadays the numerical methods which are embodied in commercial simulators are based on cartesian discretization. The irregular shape of the reservoir and the geological faults are better represented if a flexible coordinate system is used. Moreover, the application of boundary conditions are also easier with the aid of boundary-conforming coordinate systems

Concerning with the use of boundary-fitted coordinates, and other flexible grids, efforts have been recently done in the petroleum engineering area. Roson (1989), Sharpe and Anderson (1991), Forsyth (1991) and Maliska (1990, 1992, 1993), among others, have dedicated to the development of numerical methods using strucutured boundary-fitted grids.

The present paper is a report in one the topics under analysis in a more general research program to develop numerical methods, using flexible grids, for petroleum reservoir simulation. The black-oil model is employed considering the oil and water phases in a two-dimensional framework. For testing purposes the well known five-spot problem is solved with the aim of evaluating the effects of the grid orientation when using curvilinear coordinate systems. To demonstrated the ability of the model in dealing with irregular shape reservoirs, it is simulated the oil/water flow in a reservoir with 2 injection and 6 production wells.

Mathematical Model

Consider the flow of oil and water in a porous media with porosity. The equations which will form the mathematical model are obtained realizing a mass conservation balance for each component. In this case one has oil and water components and the oil and water phases. Neglecting body forces and the capillarity pressure one obtain the conservation equation for the water and the oil as

$$\nabla \cdot [\lambda_\omega \nabla P] = \frac{\partial}{\partial t}\left[\phi \frac{S_\omega}{B_\omega}\right] + \bar{q}_\omega \qquad (1)$$

$$\nabla \cdot [\lambda_o \nabla P] = \frac{\partial}{\partial t}\left[\phi \frac{S_o}{B_o}\right] + \bar{q}_o \tag{2}$$

where the equations represent a volumetric conservation, since both equations were divided by a standard density, giving rise to the volume formation factor B_ω and B_o. The unknowns of the equations are the saturation of water and oil and the pressure. The closing equations is the conservation of the global mass, given by.

$$S_\omega + S_o = 1 \tag{3}$$

where λ_ω and λ_o are the mobility, given by

$$\lambda_\alpha = \frac{KK_{r\alpha}}{B_\alpha \mu_\alpha} \tag{4}$$

Where k and $k_{r\alpha}$ are the absolute and relative permeability, respectively.

Equations (1), (2) and (3) need to be solved for the unknowns pressure and saturation of water and oil. There are two well known methods for solving this problem. The first one, the IMPES method, solves the pressure implicitly and the saturations explicitly. The way to do that is to discretize Eq. (1) and Eq. (2) for S_ω and S_o, keeping the pressure implicit, and summing the equation up, obeying Eq. (3). The resulting equation is an equation for pressure. Having pressure calculated, the saturations can be found explicitly.

The other alternative is to replace S_o in Eq. (2) by $1 - S_\omega$ and solve Eqs. (1) and (2) for pressure and water saturation in a simultaneous fashion using, normally, Newton's iteration. We have solved the problem with both methods but with emphasis, when testing the numerical algorithm, in the IMPES method and, therefore, it is the model described here.

Pressure Equation: Eq. (1) or Eq. (2). written in a generalized curvilinear coordinate system has the form

$$\frac{\partial}{\partial \xi}\left[D_{1c}\frac{\partial P}{\partial \xi} + D_{2c}\frac{\partial P}{\partial \eta}\right] + \frac{\partial}{\partial \eta}\left[D_{3c}\frac{\partial P}{\partial \eta} + D_{4c}\frac{\partial P}{\partial \xi}\right] = \frac{1}{J}\frac{\partial}{\partial t}\left(\phi \frac{S_c}{B_c}\right) + \frac{\bar{q}_c}{J} \tag{5}$$

where the subindex c means water or oil, and the coefficients can be found in Maliska et al (1992). The already introduced relative permeability $k_{r\alpha}$, as a function of saturation, is given by

$$k_{r\omega} = \frac{S_\omega}{[M(1 - S_\omega) + S_\omega]} \tag{6}$$

and k_r by

$$k_{ro} = 1 - k_{r\omega} \tag{7}$$

where M is the mobility ratio.

Approximate Equations

Integrating Eq. (5) in time and in the control volume shown in Fig. 1, one obtains

$$\frac{\Delta V}{J\Delta t}\left[\left(\frac{\phi S_c}{B_c}\right) - \left(\frac{\phi S_c}{B_c}\right)^0\right] + \frac{S^c \Delta V}{J} = \left[D_{1c}\frac{\partial P}{\partial \xi} + D_{2c}\frac{\partial P}{\partial \eta}\right]_e \Delta\eta - \left[D_{1c}\frac{\partial P}{\partial \xi} + D_{2c}\frac{\partial P}{\partial \eta}\right]_\omega \Delta\eta +$$

$$\left[D_{3c} \frac{\partial P}{\partial \eta} + D_{4c} \frac{\partial P}{\partial \xi} \right]_n \Delta\xi - \left[D_{3c} \frac{\partial P}{\partial \eta} + D_{4c} \frac{\partial P}{\partial \xi} \right]_s \Delta\xi \qquad (8)$$

The derivatives are approximated numerically using a central difference scheme, and the final discretized equation for S_c is

$$S_c = \frac{B_c J \Delta t}{\phi \Delta V} \{ -A_p^c P_p \} + \frac{B_c J \Delta t}{\phi \Delta V} \{ \sum A_{NB}^c P_{NB} \} + \hat{S}^c \qquad (9)$$

where the coefficients can be found in Maliska et al. (1992).
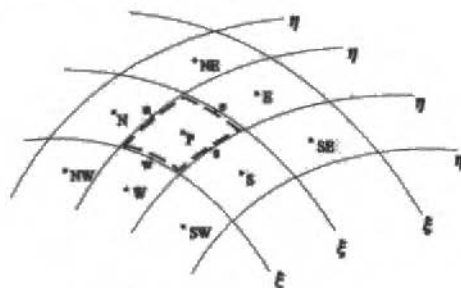
Fig. 1 Elemental control volume

As already stated, the equation for pressure is obtained by summing the saturation of water and oil, resulting in.

$$A_p P_p = A_E P_E + A_W P_W + A_N P_N + A_S P_S + A_{NE} P_{NE} +$$
$$A_{NW} P_{NW} + A_{SE} P_{SE} + A_{SW} P_{SW} \quad \hat{S} \qquad (10)$$

The control volume method requires the permeabilities to be calculated at the interfaces of the control volumes. A interpolation function is then needed, since they are stored at the center of the control volume. In this work an upwind scheme is used, setting which volume is the donor cell according if mass enters or leaves the control volume.

In the IMPES method the mobility λ and the volume formation factor B are calculated with the water saturation from the previous iteration level. When iteration is performed, inside the time level, to updated the mobility and the volume formation factor, the method is called here SEQUENTIAL, because the equation system is solved implicitly but in sequential way. It is clear that the IMPES procedure is embodied in the more general sequential formulation. The iterative procedure is:

1. Set initial pressure and saturation of the reservoir.

2. Calculate B_c and λ_c.

3. Calculate the pressure field through Eq.(10). The MSI (Schneider and Zedan, 1981) is used to solve the linear system.

4. Using the pressure field calculate the saturation of water and oil.

5. If convergence was not reached recycle from item 2.

6. Set $t = t + \Delta t$ and cycle back to item 2, repeating up to the desired time level.

Numerical Results

Before presenting the results obtained for a reservoir of complex geometry it is important to analyse the behaviour of the method in the solution of a known problem. The widely used two dimensional two-phase test problem is the five-spot pattern, reported by Yanosik and McCracken (1978), where the imiscible flow with unfavorable mobilities and the piston-type displacement are solved using cartesian parallel and diagonal grids. Despite the fact that the pyston-type problem have been also solved, only the results for the imiscible displacement will be reported. Figure 2 shows half of the curvilinear and the cartesian parallel grids employed in this work.
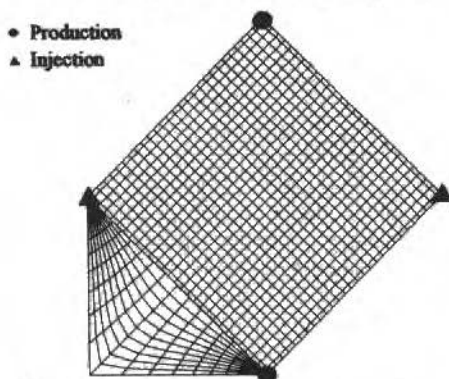
Fig. 2   Curvilinear and cartesian parallel grids

The data used for the simulation is reported in Yanosik and McCracken (1978) and in Maliska et al (1993) and, therefore, will not be reproduced here. Figure 3 shows the water saturation isolines after 0.32 porous volume injected (PVI) for the cartesian diagonal and curvilinear grids.

Figure 4 shows the results obtained in the present work with the curvilinear grid and the parallel grid (a), and the results of Yanosik and McCracken (1978), using diagonal and parallel grids, with a 5 point stencil and a two-point upstream scheme for evaluating the permeability at the interfaces.
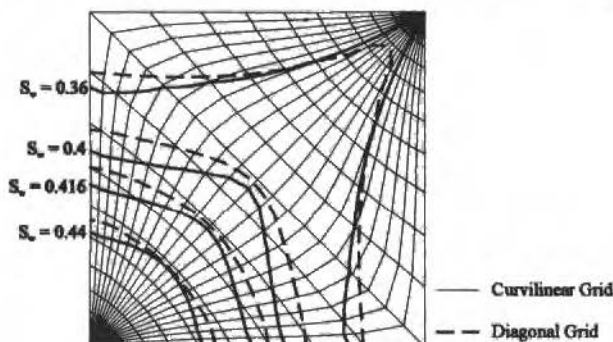
Fig. 3   Iso-saturation lines for 0.32 PVI. Diagonal and curvilinear grids

It was expected that the curvilinear grid would present similar results as the ones obtained wit the parallel grid, since along the diagonal these grids are similar. This, in fact, does not happens, as can be confirmed through Fig. 4(a), where these results are shown. This can be explained by the fact that only along the line joining the wells the parallel grid is similar to the curvilinear one. For the rest of the domain, where flows the large percentage of matter, the grid is, in fact, skewed to the flow. The results of Yanosik and McCracken (1978), Fig. 4(b), are for a two-point upstream for calculating the permeabilities. This is the reason why results agree well.

The diagonal grid, by its turn, is largely aligned with the flow, except at the diagonal. This may be the reason why the diagonal grid shows closer agreement with the curvilinear than the parallel grid, as can be seen in Fig. 3. Figure 5 shows the results of the present work using cartesian diagonal

and parallel grids. The results, of course, are not in agreement, showing the existence of grid orientation effects. The effects, however, in this work, are less pronounced than in the work of Yanosik and McCracken (1978) (curves not shown here). Not considering the fact that Yanosik and McCracken (1978) use half control volume at the boundaries, the grids used in this paper and in their work are the same.

The reason for having less pronounced grid orientation effects in this work may be attributed to the way the conservation equations are obtained. In the present work, component conservation are enforced at control volume levels, even for the control volumes at the boundaries. It is not sure that the same approach is used in Yanosik and McCracken (1978).

As a final result of the five-spot configuration, Fig. 6 shows the porous volume of oil recovered as a function of water porous volume injected, for the curvilinear grid of the present work and for the cartesian grid of Yanosik and McCracken (1978), where a 9 points scheme is used. The results agree well. It is important to point out that, in spite of using 9 points in the curvilinear grid scheme, it can not to be said that this is a 9-point scheme, since the diagonal neighbours enter the equation through the cross-derivatives, and not through the interpolation function, which is, in essence, the responsible for altering the grid orientation effects.
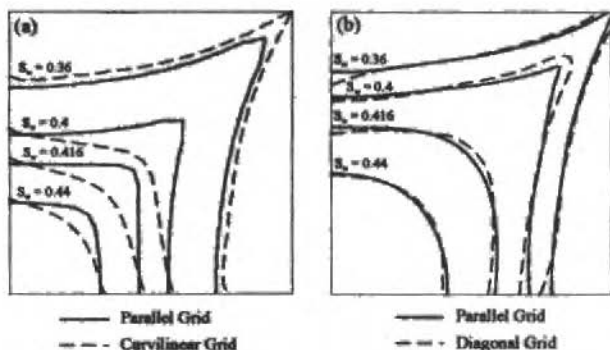
Fig. 4   Results for 0.32 PVI. Present work-curvilinear and cartesian parallel grids (a) and Yanosik and McCracken - parallel and diagonal grids (b)

As on overall evaluation of the above results one can say that the curvilinear grid suffer much less of grid orientation effects than the cartesian grids. For other coordinate systems, it is necessary to employ more elaborate (like 9 points) schemes in order to obtain results with the same quality as the ones obtained with the curvilinear grid. It must be pointed out, however, that the five-spot configuration is a naturally adequate configuration for the curvilinear grid used. Not always will be possible to find a curvilinear grid which fits so well with the flow direction as in this case
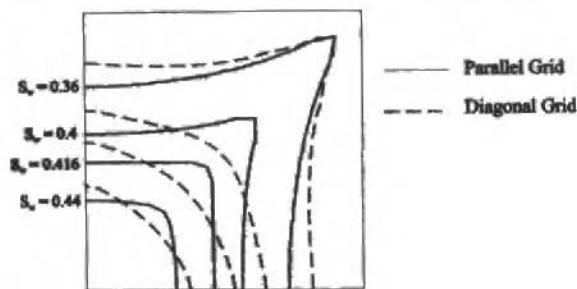

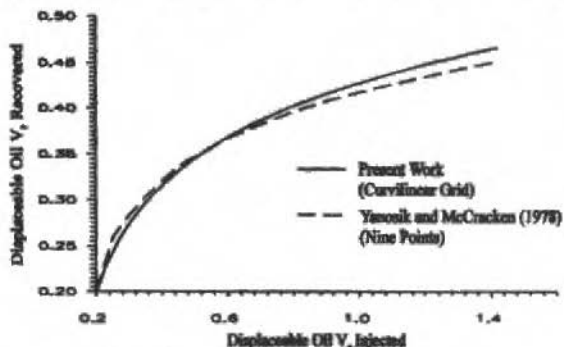Fig. 5   Results for diagonal and parallel grids

Fig. 6   Porous volume of recovered oil

To conclude the presentation of the results two-phase flow of oil and water was simulated for the reservoir shown in Fig. 7, where the curvilinear grid used the location of the injection and production wells and the geological fault are also shown. Figure 8 shows the iso-concetration after 0.05 and 0.10 porous volume injected for the two injection wells, while Fig. 9 depicts the pressure variation with time for the production wells. Inspecting Fig. 8 one sees that there is no possibility of flow through the fault, which forces the flow to go around the fault in order to reach the other region of the reservoir.
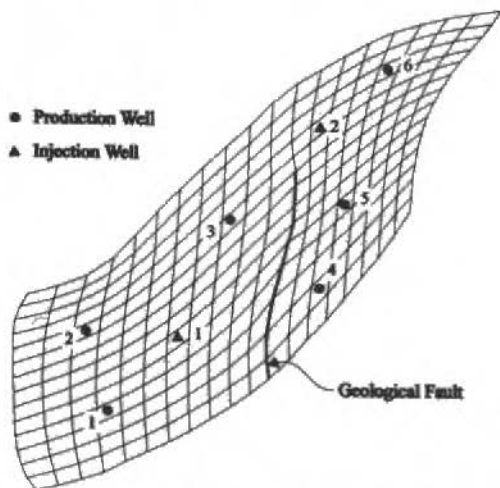
Fig. 7   Curvilinear grid for the irregular reservoir

0.05 PVI   0.10 PVI
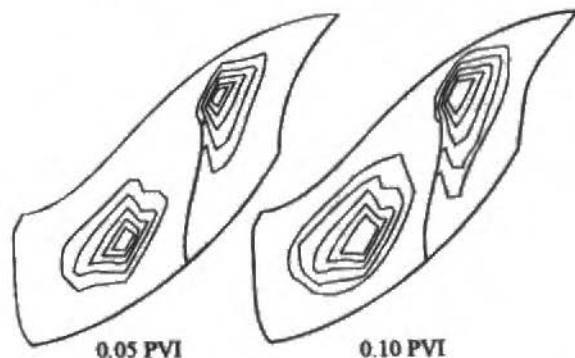
Fig. 8   Iso-saturation after 0.05 and 0.10 PVI
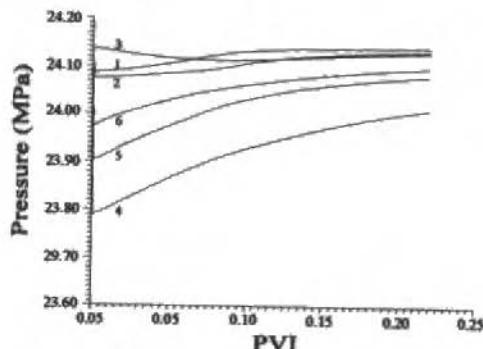
Fig. 9　Pressure at the production wells

Conclusions

The simulation of the two-dimensional two-phase flow in a petroleum reservoir was realized using boundary-fitted curvilinear grids. The results demonstrated that the model performs well, helps in alleviating the grid orientation effects and are suitable for simulating petroleum reservoirs of arbitrary shape. Geological faults can be also easily modelled using this type of grid. The use of boundary-fitted grids is a new topic of research in petroleum reservoir simulation and the results encourages further developments. Currently the model is being extended to admit the gas phase in order to simulate the complete black-oil model.

References

Forsyth, P. A.,1989, "A Control Volume Finite Element Method for Local Mesh Refinement", Paper SPE 18415, 10th SPE Symposium on Reservoir Simulation, pp. 85-96.

Maliska, C. R. Silva, A. F. C., Marcondes F., Lopes M. N., and Cunha, A. R., 1991, "Numerical Solution of the Single-Phase Flow with a Tracer "(in Portuguese), Report prepared to: CENPES/PETROBRAS S.A., Part I.

Maliska, C. R., Silva A. F. C., Jucá P. C. S., Cunha, A. R., and Lopes M. N., 1992, "Numerical Solution of the Two-Phase Oil/Water Flow" (in Portuguese), Report prepared to: CENPES/PETROBRAS S. A., Part II.

Maliska, C. R., Silva A. F. C. Jucá, P. C. S., Cunha A. R., and Livramento, M. A., 1993, "Development of a Three-Dimensional Black-oil Simulator Using Boundary-Fitted Coordinates" (in Portuguese), Report prepared to: CENPES/PETROBRAS S. A., Part I.

Rozon, B. J., 1989, "A Generalized Finite Volume Discretization Method for Reservoir Simulation", Paper SPE 18414, 10th SPE Symposium on Reservoir Simulation, pp. 71-84.

Schneider, G. E. and Zedan, M., 1981, "A Modified Strongly Implicit Procedure for the Numerical Solution of Field Problems", Numerical Heat Transfer, Vol. 4, pp. 1-19.

Sharpe, H. N., and Anderson, D. A., 1991, "Orthogonal Curvilinear Grid Generation with Preset Internal Symposium of Reservoir Simulation, pp. 17-20.

Yanosik, J. L., and McCracker, T. A., 1978, "A Nine-Point Finite Difference Reservoir Simulator for Realistic Prediction of Unfavorable Mobility Ratio Displacements", SPE Journal, Vol.18, pp. 253-262.

Análise Experimental de Trocadores de Calor Tubo Capilar-Linha de Sucção Utilizando HFC - 134a

An Experimental Analysis of Capillary Tube-Suction Line with HFC-134a

Roberto de Aguiar Peixoto
IPT - Instituto de Pesquisas Tecnológicas do Est. de S. Paulo S.A
Universidade de São Paulo - Dep. Engenharia Mecânica
Pregrag Hrnak
Frank Johnson
John Meyers
Air Conditioning and Refrigeration Center - ACRC, University of Illinois U.C.

Abstract

Expansion devices are one of the four major components of vapor compression refrigeration systems and small systems use capillary tube as this device. Today, a capillary tube-suction line heat exchanger geometry (ct-sl hx) is used in almost all household refrigerators. Capillary tube-suction line heat exchangers were tested in this work with refrigerant HFC-134a that has emerged as the primary condidate for CFC-12 replacing.
Keywords: Capillary Tube-Suction Line Heat Exchanger, Refrigerant HFC-134a

Resumo

Este trabalho apresenta levantamentos experimentais em trocadores de calor tubo capilar-linha de sucção com o refrigerante HFC-134a, principal candidato à substituição do CFC-12 em refrigeradores domésticos. A instalação experimental, construída para testes de tubos capilares adiabáticos e trocadores de calor tubo capilar-linha de sucção, utiliza uma bomba, ao invés de compressor. Os valores de vazão mássica e temperatura medidas foram comparados com os resultados previstos por um modelo para simulação numérica previamente desenvolvido.
Palavras Chave: Trocador de Calor Tubo Capilar-Linha de Sucção, Refrigerante HFC-134a

Introdução

Dispositivos de expansão, junto com o compressor e os trocadores de calor (evaporador e condensador) são os componentes básicos de sistemas de refrigeração por compressão de vapor. Sistemas selados com compressores herméticos e com capacidade de refrigeração até 35 kW (Ashrae, 1988), usam um tubo de pequeno diâmetro (0,5 a 2,0 mm) e grande comprimento (1 a 6 m), chamado de tubo capilar, como dispositivo de expansão. Exemplos destes últimos sistemas são os refrigeradores domésticos e as unidades compactas de ar condicionado. As principais vantagens destes dispositivo de expansão de geometria fixa, comparado com uma válvula de regulagem de pressão, são seu baixo custo e a equalização de pressão proporcionada quando o sistema está desligado, o que reduz o torque de partida do compressor.

Nos refrigeradores domésticos, uma parte do comprimento do tubo capilar é colocada em contato com a linha de sucção do compressor formado um trocador de calor em contracorrente denominado trocador de calor tubo capilar-linha de sucção. Esta alternativa proporciona um aumento da capacidade de refrigeração devido à diminuição do título de vapor do refrigerante na entrada do evaporador (Pereira et al., 1988).

Devido a uma ironia da história, os CFCs que foram desenvolvidos para substituir outros fluidos refrigerantes considerados tóxicos, deverão ser eliminados, em função do seu impacto sobre o meio ambiente, em um curto prazo de tempo, conforme estabelecido no Protocolo de Montreal. Vários setores industrias serão afetados, principalmente o de refrigeração e ar condicionado que deverá gerar, nos próximos anos, alternativas à utilização de CFCs.

Neste trabalho foi analisado experimentalmente o desempenho de trocadores de calor tubo capilar-linha de sucção utilizando o fluido refrigerante HFC-134a, tido como o mais provável substituto do CFC-12 em refrigeradores domésticos.

Levantamentos Experimentais Prévios

A grande maioria das unidades experimentais relatadas na literatura aberta, foi construída utilizando o ciclo de refrigeração por compressão de vapor para a análise de tubos capilares adiabáticos (sem troca de calor com a linha de sucção). Algumas modificações em relação a um ciclo padrão, tais como o uso de dois compressores em paralelo e válvulas de "by pass", foram introduzidas com o objetivo de controlar independentemente as variáveis que afetam o escoamento no inferior do tubo capilar. No caso de tubos capilares adiabáticos estas variáveis são pressão de entrada e saída e temperatura ou título de entrada no tubo capilar.

Em função da interdependência destas variáveis, mesmo com as transformações realizadas, nem sempre é possível o seu ajuste independente, além disso, existe a dificuldade de obtenção do regime permanente desejado para as condições de teste (Kuehl e Godschimdt, 1991). Um aspecto positivo desta alternativa é a sua facilidade de montagem e operação devido à utilização de equipamentos padrões, de produção seriada, da indústria de refrigeração.

Uma alternativa ao ciclo de compressão de vapor, utilizada em algumas investigações experimentais, foi o uso de processo descontínuo tipo "blow-down". Nesta configuração, a seção de teste ou tubo capilar a ser ensaiado é colocado entre dois reservatórios, um de "alta" e um de "baixa" pressão e o refrigerante escoa através do tubo capilar durante um determinado período definido pela capacidade dos reservatórios. Exemplos desta alternativa envolvem desde simples sistemas construídos, na época em que os CFCs eram baratos e não estavam associados a danos ao meio ambiente, conectando-se uma extremidade do tubo capilar na saída do próprio reservatório utilizado para armazenamento de refrigerante e a outra aberta para a atmosfera (Whitesel, 1957), quanto sistemas "fechados" nos quais o refrigerante armazenado no reservatório de "baixa" pressão, após a expansão através do tubo capilar, é retornado novamente ao reservatório de "alta" pressão (Mikol, 1963, Pate, 1982, Bittle, 1993). Esta opção de instalação experimental tem a vantagem de permitir o adequado controle das variáveis envolvidas no processo, principalmente da pressão de entrada no tubo capilar, mas apresenta a desvantagem do alto valor da carga de refrigerante a ser utilizada, devido à sua característica de processo descontínuo, e de exigir uma instalação mais complexa no caso da simulação do trocador de calor tubo capilar-linha de sucção para o controle de escoamento de vapor de refrigerante à baixa temperatura que resfria o tubo capilar.

Unidade Experimental Construída

No presente trabalho, a concepção utilizada na unidade experimental desenvolvida foi reproduzir as vantagens de um ciclo de compressão de vapor padrão, com operação contínua, sem as suas desvantagens principais mencionadas acima. Com o objetivo de obter escoamento de refrigerante puro ou misturas controladas de refrigerante e óleo, é utilizada uma bomba, ao invés de compressor, para movimentação e pressurização de refrigerante.

Como, ao contrário do que ocorre um compressor onde o refrigerante é comprimido na fase gasosa, o refrigerante tem que estar na fase líquida na entrada da bomba, a instalação foi projetada de forma a prover esta condição através de sistemas auxiliares, assim o refrigerante, após a saída do tubo capilar, é condensado e subresfriado antes da entrada da bomba.

A unidade experimental foi construída no ACRC (Air Conditioning and Refrigeration Center, University of Illinois at Urbana-Champaign, USA.), e simula as condições operacionais encontradas na prática por tubos capilares adiabáticos e por trocadores de calor tubo capilar-linha de sucção. A unidade é constituída de três sistemas.

Sistema principal: O sistema principal é formado pelo circuito de refrigerante a ser testado como fluido de trabalho envolvendo a seção de teste, a bomba e o acumulador de refrigerante líquido que simula o evaporador, e a instrumentação para medição de vazão, pressão e temperatura. Envolve também os subsistemas de aquecimento, utilizados no controle do subresfriamento na entrada do tubo

capilar, no reservatório para evitar oscilações na pressão do refrigerante na saída da bomba, e no acumulador para a evaporação e superaquecimento do refrigerante no acumulador da linha de sucção. A seção de teste foi dotada de visores de vidro que permitem uma observação visual do escoamento a montante e a jusante do turbo capilar. Um esquema do sistema principal pode ser visto na Fig. 1.
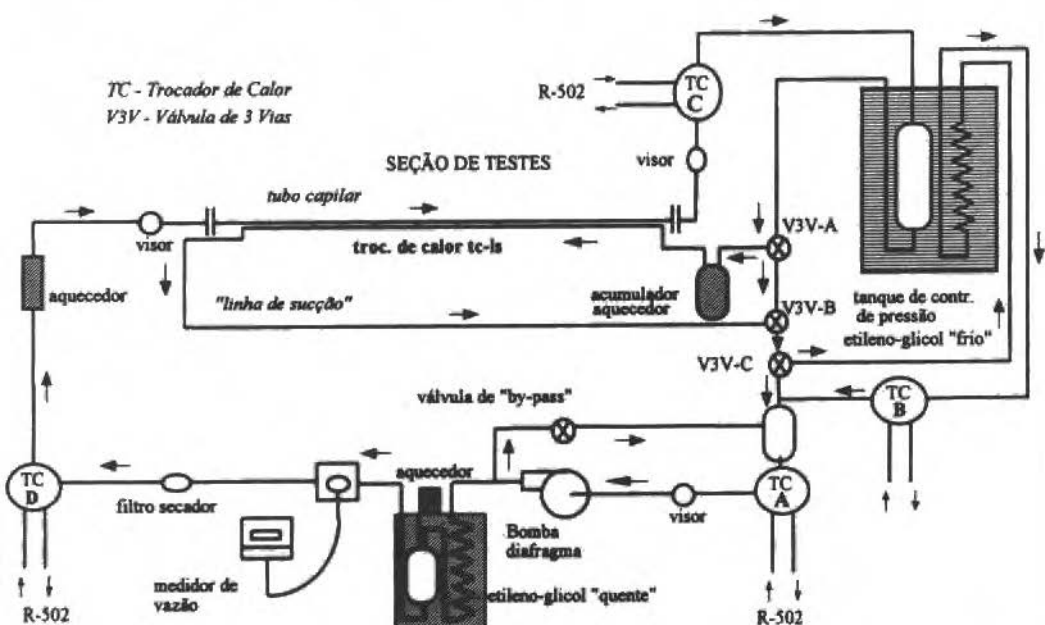

Fig. 1   Unidade experimental construída para teste de tubos capilares adiabáticos e não-adiabáticos (tc tc-ls)

       O refrigerante após a seção de teste é condensado e resfriado a pressão constante no trocador de calor TC-C e no tanque de controle de pressão, descrito na seção seguinte. A válvula de três vias colocada após o tanque, V3V-A, permite que o refrigerante líquido tanto possa ir para o trocador de calor TC-A, localizado antes da bomba, quanto para o acumulador-aquecedor. Esta configuração possibilita o teste de tubos capilares adiabáticos ou de trocadores de calor tubo capilar-linha de sucção. No caso de teste de trocadores de calor tubo capilar-linha de sucção, o refrigerante se dirige ao acumulador aquecido por uma resistência elétrica, onde evapora e escoa para o trocador de calor tc-ls, resfriando o tubo capilar. Para ser condensado e subresfriado, o vapor superaquecido na saída da linha de sucção é enviado ao trocador de calor TC-C diretamente ou, dependendo do valor do subresfriamento necessário na entrada da bomba, passa pelo reservatório de etileno-glicol antes de se dirigior ao trocador de calor TC-A. Este processo é controlado através das válvulas de três vias V3V-B e V3V-C. Após a bomba, o refrigerante passa pelo medidor de vazão e entra novamente no tubo capilar fechando o ciclo. O controle de vazão e pressão do refrigerante é feito através de uma válvula de "by-pass" localizada entre a saída da bomba e o trocador de calor TC-A.

       Circuito de etileno-glicol: O segundo sistema é formado por um circuito de etileno-glicol contendo um tanque de refrigerante, um reservatório de etileno-glicol, uma bomba e dois trocadores de calor coaxiais com R-502. A função do reservatório de etileno-glicol resfriado à baixa temperatura é a condensação do refrigerante, controle da pressão na saída do tubo capilar e a condensação do vapor de refrigerante após a linha de sucção. O sistema foi projetado para ter uma mistura líquido-vapor de refrigerante superaquecido no tanque, de forma que a pressão é controlada através de temperatura. Isto é feito através da troca de calor com o etileno-glicol à baixa temperatura, auxiliado pelo trocador de calor localizado antes do tanque (TC-C) que possibilita a obtenção de temperaturas mais baixas. O

resfriamento do etileno-glicol é feito utilizando uma bomba para circulá-lo através do trocador de calor com R-502 (TC-B) e o controle da sua temperatura é auxiliado por uma resistência elétrica colocada na linha entre a bomba e o reservatório.

Sistema de refrigeração com R-502: O terceiro sistema é formado por um circuito de refrigeração por compressão de vapor, utilizando R-502 como fluido de trabalho, envolvendo compressor, válvula de expansão, condensador e três evaporadores. Através destes evaporadores, que são os trocadores de calor TC-A TC-B e TC-C mencionado anteriormente, este circuito fornece a carga de resfriamento necessário para: a) resfriamento do etileno-glicol, b) subresfriamento do refrigerante líquido na saída do tanque de controle de pressão e antes da bomba, c) auxiliar a condençasão e controle da pressão do refrigerante na saída do tubo capilar.

O valor da carga de refrigeração fornecida pelo sistema de R-502 é controlado através da válvula de expansão, localizada antes do trocador de calor TC-A e utilizando-se um dispositivo de controle da rotação do compressor através da variação de freqüência da alimentação. Uma funcão adicional do sistema de refrigeração R-502 é aquecer o refrigerante antes da entrada do tubo capilar de forma a auxiliar o controle do subresfriamento. Isto é feito utilizando-se um "by-pass" na saída do compressor que devia uma parte de vapor R-502 a alta temperatura para um trocador de calor coaxial colocado antes da seção de teste.

Instrumentação: Foi utilizada para a medição da vazão mássica do refrigerante escoando no interior do tubo capilar um medidor por força de Coriolis com precisão de 0,4%

Para a medida da pressão manométrica do refrigerante na entrada e saída do tubo capilar, foram empregados transdutores de pressão capacitivos. A pressão atmosférica no local dos ensaios foi obtida através de um barômetro de mercúrio e corrigida para compensar efeitos de temperatura e gravidade do local. A precisão das medidas de pressão é de ±0.04 bar.

Termo pares tipo T (cobre-constantan) foram utilizados para a medição das temperaturas na seção de teste e em outros pontos da unidade experimental, com precisão de ±0,2C.

Levantamento Experimentais Realizados

Visando a caracterização experimental do desempenho de trocadores de calor de tubo capilar-linha de sucção com o refrigerante HFC-134a, foram realizados levantamentos experimentais em dois trocadores de calor, um composto de tubos laterais e outro de tubos concêntricos, com as características geométricas apresentadas na Fig. 2.

Foi medido o diâmetro interno médio do tubo para cada um do trocadores de calor. O método utilizado foi a determinação do volume interno do tubo capilar através do seu enchimento com um fluido de massa específica conhecida. Para evitar erros de medição devido à existência de "vazios" no interior do tubo capilar foi utilizado o álcool isopropil 70% que tem um baixo valor de tensão superficial. A medição da massa de álcool no tubo capilar foi realizada utilizando uma balança com leitura de 0,01 g de fundo de escala. O valor encontrado para o diâmetro médio do tubo capilar foi de 0,813 mm, dentro, portanto, da tolerância de 0,025 mm estabelecida pelo fabricante do tubo.

As unidades testadas foram isoladas termicamente utilizando material apropriado para tabulações de refrigeração constituído por elastômero com coduvidade térmica igual a 0,043 W/m K. A espessura do isolamento utilizada foi de 50 mm.

Para o trocador de calor constituído por tubos laterais, além da medição da vazão de refrigerante pressão de entrada e pressão no reservatório de saída, foram medidas as temperaturas de parede ao longo do tubo capilar e a temperatura do refrigerante na linha de sucção, na entrada do trocador de calor. Foram medidas as temperaturas na parede do tubo capilar, devido à impossibilidade do uso de técnicas convencionais para a medição da temperatura do fluido refrigerante em função do pequeno diâmetro do tubo capilar. Considerando o alto valor do coeficiente de transferência de calor convectivo do refrigerante, na faixa de 8000 W/m2. K, a temperatura de parede é muito próximo da temperatura do refrigerante. Os cabos dos termopares foram conectados à parede do tubo usando um adesivo a base de epóxi metálico ("aluminum-epoxy").

Antes da fixação, o local do termopar no tubo foi limpo com acetona e o cabo do termopar foi enrolado no tubo várias vazes, de forma a evitar condução axial de calor, neste cabo, anulando o efeito aleta que influenciaria as medidas.

Para o trocador de calor constituído por tubos concêntricos, foram medidas as temperaturas de parede do tubo capilar nas regiões de entrada e saída do trocador de calor .
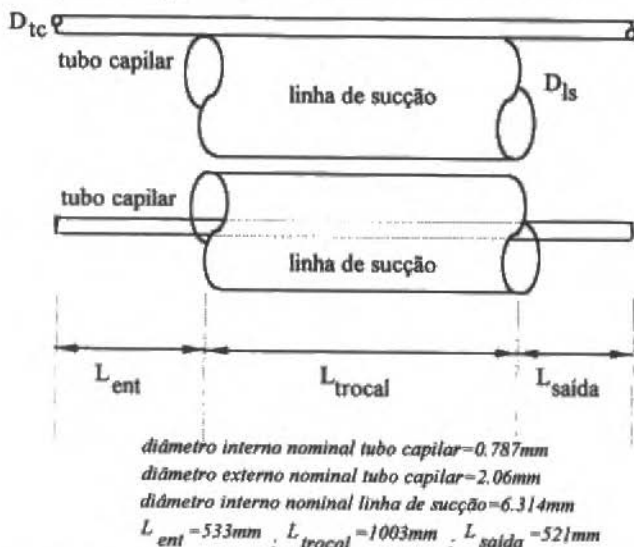

diâmetro interno nominal tubo capilar=0.787mm
diâmetro externo nominal tubo capilar=2.06mm
diâmetro interno nominal linha de sucção=6.314mm
$L_{ent} = 533mm$; $L_{trocal} = 1003mm$; $L_{saída} = 521mm$

Fig. 2   Trocadores de calor tubo capilar-linha de sucção testados

Resultados Obtidos

Um dos objetivos da realização dos levantamentos experimentais descritos no presente trabalho foi a validação de um modelo de simulação numérica de trocadores de calor tubo capilar-linha de sucção apresentado pelos autores em trabalho prévio (Peixoto e Silvares 1993).

Os resultados obtidos nos levantamentos experimentais realizados foram, basicamente, a vazão mássica de fluido refrigerante escoando no tubo capilar, para determinadas condições de entrada e saída no tubo capilar e linha de sucção, e o perfil de temperatura conforme descrito no item anterior. A seguir são mostrados alguns dos resultados experimentais obtidos e das comparações com os valores previstos pelo modelo matemático de simulação, sendo que o conjunto completo dos dados experimentais obtidos é apresentado em Peixoto(1994).
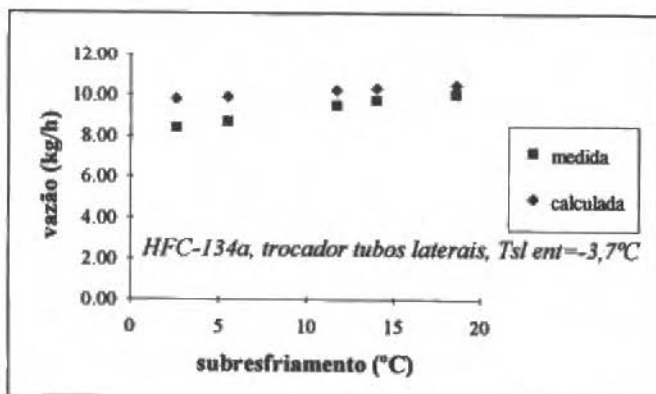
Fig. 3   Comparação da vazão mássica calculada pelo modelo com a vazão mássica medida (Pent=1400 KPa)
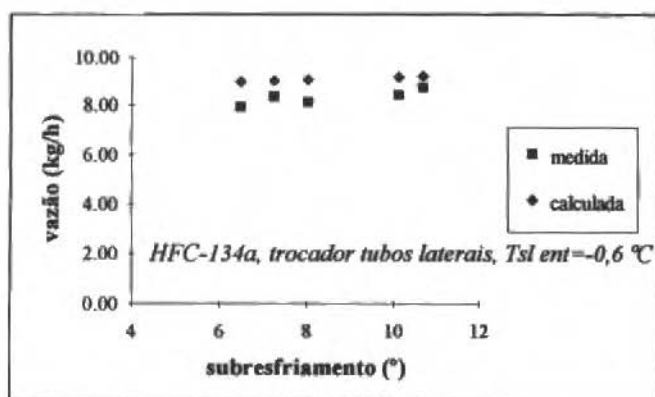
Fig. 4 Comparação da vazão mássica calculada pelo modelo
com a vazão mássica medida (Pent=1250 KPa)
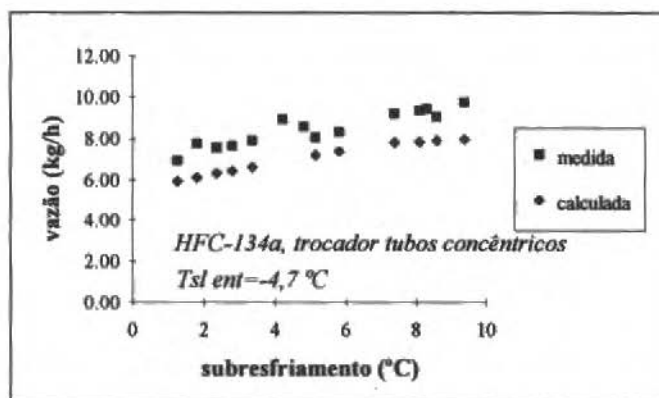
Fig. 5 Comparação da vazão mássica calculada pelo modelo
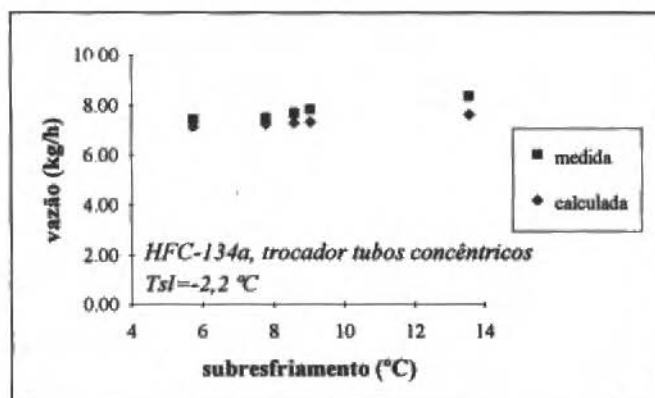com a vazão mássica medida (Pent=1150 KPa)

Fig. 6 Comparação da vazão mássica calculada pelo modelo
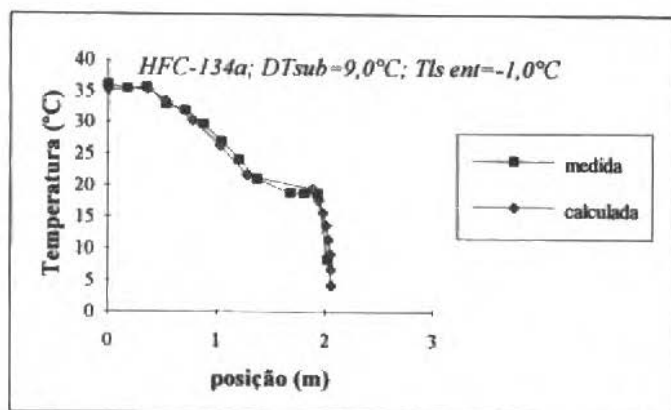com a vazão mássica (Pent=1060 KPa)

Fig. 7 Comparação entre o perfil de temperatura da parede do tubo capilar medido e calculado pelo modelo matemático (trocador de calor tubos laterais Pent=1150KPa)

Conclusões

Conforme pode ter observado nas figuras apresentadas os valores de vazão mássica calculados pelo modelo para a configuração trocador de calor tubos laterais, na maioria dos casos são maiores que os valores medidos. A diferença média e a diferença máxima, entre os valores medidos e os calculados, são de 8,0% e 15,9% respectivamente. Para o trocador de calor constituído por tubos concêntricos, o comportamento dos valores calculados pelo modelo matemático é o inverso. Os valores de vazão calculados são menores que os valores medidos. Para esta configuração do trocador de calor, a diferença média e a diferença máxima, entre os valores medidos e os calculados, são de 9,7% e 20,0%, respectivamente.

As diferenças existentes entre os valores medidos experimentalmente e calculados pelo modelo estão relacionadas com as hipóteses adotadas na formulação do modelo. Estudos teóricos e levantamentos experimentais adicionais estão em realização para a validação do modelo numa faixa mais ampla de parâmetros operacionais e geométricos e para o aumento da sua precisão.

Agradecimentos

Referências

Ashrae Handbook Equipment, Ch. 19, 1988.
Dudley, J.C., 1962, "A Photographic Study of the Two-Phase Flow of Freon in Small Bore Tubes," M. S Thesis, University of Wisconsin, Madison, WI, USA.
Bittle, R. R., Stephenson, W. R., and Pate, M. B., 1993, "An Experimental Evaluation of Capillary Tube-Suction Line Heat Exchanger Performance with HEC-152a", Submitted to ASHRAE Transactions.
Kuehl, S. J., and Goldschimdt, V. W, 1991, "Modelling of Steady Flows of R-22 Through Capillary Tubes". ASHRAE Transactions, vol. 96, part 1, pp. 139-148.
Pate, M. B., 1982, "A Theoretical and Experimental Analysis of Capillary Tubo-Suction Line Heat Exchangers" PhD Thesis, Purdue University.
Peixoto, R. A., and Silvares, O. M., 1993, "Analysis of the Capillary Tube-Suction Line Heat Exchangers Used in Refrigeration Systems", Anais do XIII COBEM, Brasília, pp. 769-772.
Peixoto, R. A., 1994, "Análise Teórico-Experimental do Escoamento do Refrigerante HFC-134a em Trocadores de Calor Tubo Capilar-Linha de Sucção Utilizados em Sistemas de Refrigeração. "Tese de doutoramento, Universidade de São Paulo, SP, Brasil.
Pereira, R. H., et al., 1987, "Influência de Transferência de Calor em Tubos Capilares e Linhas de Sucção sobre o Desempenho de um Refrigerador Doméstico," Anais do IX COBEM, Florianópolis, pp 355-357.
Whitesel, H. A., 1957, "Capillary Two-Phase Flow", Refr. Eng., Vol. 65,n 4, pp 42-44 e 98-99.

Vaporization of Dilating Non-Ideal Binary Droplets with Radiation Absorption

P. L. C. Lage
C. M. Hackenberg
Programa de Engenharia Química, COPPE
Universidade Federal do Rio de Janeiro, C.P. 68502
21945-970, Rio de Janeiro, Brazil

R. H. Rangel
Department of Mechanical and Aerospace Engineering
University of California at Irvine, Irvine CA 92717-3975, USA

Abstract

A recently developed liquid vaporization model for multicomponent droplets has been enhanced in order to study the effect of thermal radiation absorption in binary droplet vaporization. The possible coupling between radiation absorption and droplet microexplosion is also investigated. The results show that radiation absorption can influence droplet vaporization in combustion environments and might explain some experimental findings on microexplosion phenomena. The vaporization model including radiantion absorption also predicts the experimentally-observed sparkle at the end of droplet combustion (flash vaporization).
Keywords: Vaporization, Multicomponent Droplets, Droplet Microexplosion, Thermal Radiation Absorption

Introduction

The explosive vaporization of multicomponent mixtures has been predicted theoretically (Law, 1978) and confirmed experimentally (Lasheras et al, 1980, Wang and Law, 1985, Wang et al., 1894) for a low Reynolds number droplet. Recently, the vaporization and microexplosion of burning methanol-dodecanol mixture droplets has been observed at low gravity conditions (Yang et al., 1990), which eliminates buoyancy effects. There is agreement among experimental and numerical investigators that the basic causes of microexplosion are the different rates of thermal and mass diffusion and the volatility differential between the mixture components. The predicted trends of necessary volatility differentials and influence of concetration and pressure have been verified by experiments (Lasheras et al., 1980, Wang and Law, 1985, Wang et al., 1984). However, the radial positions at which bubbles are formed are murch closer to the droplet center than the conventional diffusive model predicts (Wang et al., 1984). Another interesting observation is the fact that alcohol-alkane mixtures undergo explosive vaporization only if the alcohol is the more volatile component (Wang and Law, 1985). This might be explained by the non-ideality of the liquid mixtures, since non-ideal mixture tend to present a lower nucleation temperature than that obtained by the molar-weighted average of the pure component nuclueation temperatures. Another interesting experimental fact is that, when no disruptive burning occurs, the combustion of pure substance or mixture droplets ends with a weak sparkle. This was believed to be caused by the microexplosion of the very small droplets due to the presence of heavy impurities in the fuels (Wang and Law, 1985, Wang et al., 1984). Recent simulation results (Lage et al., 1993) indicate that microexplosion is a result of flash vaporization which does not require the presence of impurities in a binary droplet in order to occur.

Recently, a diffusive liquid vaporization model for multicomponent droplet vaporization has been developed (Lage et al., 1993). It includes: spatially and time dependent density, the interdiffusion term in the energy equation, variable properties, and non-ideal phase equilibrium. This model predicts a faster vaporization than that predicted by the conventional diffusive model (Law, 1978). This is mainly due to the presence of a radial velocitv caused by the thermal expansion of the droplet. This model is also able to predict the weak sparkle at the end of the combustion of a multicomponent droplet (Lage et al., 1993). Another vaporization model that includes spatially variable density and especific heat of liquid-phase is the one recently developed by Megaridis (1993) for a convective environment. The inclusion of these property variations also promotes a faster droplet vaporization, caused mainly by the thermal expansion, as has been anticipated by Lage et al.(1993).

The influence of radiation absorption in monocomponent droplet vaporization has been extensively analyzed (Lage and Rangel, 1993b, Park and Armstrong, 1989, Tuntomo, 1990). A criterion has been proposed to determine the influence of thermal radiation absorption in droplet vaporization (Lage and Rangel, 1993b). However, the interaction between radiation absorption and microexplosion phenomena in multicomponent droplet vaporization is not well understood.

Is this work, the diffusive model previously developed is improved by the addition of radiation absorption effects. The new model is used to verify the importance of thermal radiation absorption in multicomponent droplet vaporization. Using this model, the possible interaction between droplet microexplosion and radiation absorption in multicomponent droplet vaporizartion. Using this model, the possible interaction between droplet microexplosion and radiation absorption is analyzed. The non-ideal behavior of the liquid mixture is considered both in the phase equilibrium at the surface and in the superheating temperature calculation.

Vaporization Model

The diffuse vaporization model is fully described in a previous paper (Lage et al., 1993). It solves the mass species, and energy conservation equations for the binary droplet, including physical property variations with temperature and concentration and the non-ideal equilibrium at the droplet surface. Here, this model is extended to include radiation absorption inside the droplet. For the stagnant droplets considered here, the gas-phase model is the film theory (Bird et al., 1960). The non-ideal equilibrium at the droplet surface is calculated using the liquid-mixture activity coefficients determined by Wilson's equation (Ohe, 1989).

The absorption of thermal radiation can be calculated by electromagnetic theory if the irradiation characteristics and the mixture optical properties are known (Lage and Rangel, 1993a, Mackowski, 1990). However, the irradiation characteristics (intensity and angular distribution) and the mixture optical properties are often unknown. Thus, some assumptions have to be introduced. Previous results for monocomponent droplet vaporization (Lage and Rangel, 1993b) have shown that the radiation absorption may be approximated by a uniform source term inside the droplet. Using this hypothesis, only one parameter, the droplet absortivity α_R, is needed in the analysis. Thus, it seems convenient to use a parametric study to analyse the influence of radiation absorption in the vaporization process. The parametric study was carried out by choosing the droplet absortivity in the range obtained in previous works (Lage and Rangel, 1993a, 1993b) at conditions similar to those prevailing in combustion environments. Further details of the analysis are given elsewhere (Lage, 1992, Lage et al., 1993).

Superheating-Limit Calculation

The homogeneous nucleation theory is used to determine the kinetic limit of superheating of a liquid in the absence of any surface or solid matter (active sites). Sripov (1974) gives a description of the several existent theories for nucleation. Several authors have exetended the homogeneous nucleation theory to multicomponent mixtures (Avedisian and Glassman, 1981, Blander et al., 1971, Holden and Katz, 1978, Pinnes and Mueller, 1979). The calculation of the kinetic limit of superheating given here closely follows that given by Avedisian and Glassman (1981). Two modifications have been introduced: (1) the partial molar volume of each component is calculated by correlations based on experimental values of the molar volume of the pure substance, since it is known that the Peng - Robinson equation of state does not give accurate liquid volumes, and (2) a pseudo-critical temperature is used in the Gibbs number definition instead of the mixture temperature, following the findings of Lienhard and Karimi (1981) and Biney et al. (1986). Thus, the kinetic rate of nucleus formation, J, is given by

$$J = NBexp(Gb) \qquad (1)$$

where N is the number density of liquid molecules, B is the evaporation rate constant and Gb is the Gibbs number, as given respectively by

$$N \cong \frac{N_{A\upsilon}}{\upsilon} \qquad (2)$$

$$B = \frac{8P\sigma^2}{(P-P^L)^2} \left(\frac{2\pi}{R_g T}\right)^{1/2} N_{A\upsilon} \sum_{i=1}^{n} \frac{y_i}{M_i^{1/2}} \qquad (3)$$

$$Gb = \frac{16\pi\sigma^3}{3k_B T_{cm}(P-P^L)^2} \qquad (4)$$

where, $N_{A\upsilon}$ is the Avogadro number, υ is the molar volume, R_g is the gas constant, k_B is the Boltzmann constant, subscript i indicates each species, y_i is the gas molar fraction, M_i is the molecular weight, σ is the mixture surface tension, P^L is the liquid-phase pressure, $T_{cm} = \sum_{i=1}^{n} y_i T_{ci}$ is the mixture pseudo-critical temperature and $P = \sum_{i=1}^{n} P_i$ is the mixture pressure, for the partial pressure of each component, P_i, given by

$$P \cong y_{ie} P_e \exp\left[\frac{\bar{v}_i^L}{R_g T}(P^L - P_e)\right] \qquad (5)$$

where P_e is the pressure and y_{ie} is the vapor composition at a plane vapor-liquid surface at equilibrium. The phase equilibrium was calculated using the Wilson's equation for the liquid phase activity coefficients and the Peng-Robinson equation for the vapor phase fugacities. Equation (5) corrects for the partial pressure inside the bubble, assuming that the partial molar volume is pressure independent and that the vapor phase fugacities inside the bubble are the same as those for the vapor-liquid equilibrium through a plane surface (Avedisian and Glassman, 1981). Once the process is specified, the nucleation rate is estimated and the superheating limit is calculated by the above equations.

Numerical Solution

The control-volume method (Patankar, 1980) was used to discretize in space the partial differential equations of the vaporization model. The resulting system of ordinary differential equations are numerically integrated using DAWRS (Differential-Algebraic Wave form Relaxation Solver) (Secchi et al., 1991). The DAWRS algorithm automatically controls the precision in the time integration, while the number of control volumes were varied until converged results for temperature and concentration were obtained. The results shown below are, at least, 1% accurate. Analysis of convergence characteristics of this method is given in a previous work (Lage et all., 1993).

Results and Discussion

A heptane-methanol mixture, for which an almost complete set of data is available from different sources (Gallant, 1968, Melhem et al., 1989, Ohe, 1989, Reid et al., 1987, Vargaftik, 1975), was chosen. Moreover, this mixture is highly non-ideal and it resembles the methanol-gasoline mixture, due to its similar physical properties. In the following, computational results will be shown for the vaporization of droplets with an initial radius of $50 \, \mu m$, initial temperature of 300 K and initial heptane mass fraction of 0.5, in a stagnant environment at 800 K and 10 atm. The reference temperature, T_r, is 400 K and the reference properties are the initial mixture properties. The incident thermal radiation is assumed to be isotropic and with the Planck's distribution at 2000k. This temperature is as high temperature (comparing to the environment temperature) to be used as a reference blackbody temperature in a combustion environment. However, it was chosen to intensify the amount of energy absorbed by the droplet in order to verify if there is any coupling between radiation absorption and droplet microexplosion. It should be noted that the mixture analyzed has a small volatility differential, and it should undergo explosive vaporization only at severe conditions.

The phase equilibrium diagram of the n-heptane-methanol mixture at 10 atm is shown in Fig. 1. It has been calculated by using the Wilson's equation for the liquid-phase activities and the Peng-Robinson equation for the gas phase fugacities (Melhem et al., 1989, Ohe, 1989). This mixture shows an azeotropic point at a heptane molar fraction of about 0.26.

From the vaporization results given in Figs. 2 and 3, the droplet lifetime for the 50 μm - droplets considered here is about 20 ms (which corresponds to $\tau = \alpha_o^t / R_o^2 \sim 1$, where the subscript o indicates the initial conditions). The time available for homogeneous nucleation, t_n, should be two orders of magnitude lower to insure nucleation during the period of time where the droplet is at a high temperature. Thus, t_n is of the order of 0.2 ms. An error in this order of magnitude analysis is not too important, because the superheating limit is quite insensible to the J value used in its calculation. Using the droplet volume, the nucleation rate may be estimated by $J \sim 3 / (t_n 4\pi R^3)$ and the value $J \sim 10^{10} cm^{-3} s^{-1}$ is thus obtained. The superheating limit predicted for this mixture at 10 atm using the above value of J is also shown in Fig. 1. From this figure, it is clear that microexplosion is very unlikely in the n-heptane-methanol mixture at these conditions. This conclusion is supported by the fact that the maximum temperature in the phase equilibrium diagram (n-heptane boiling point) is only 8K above the minimum value of the superheating ig limit. It is worthy noting that there is a minimum in the kinetic superheating limit which is near the azeotropic point of the mixture. This kind of non-ideal behavior might be responsible for the larger tendency to microexplosion shown by non-ideal mixtures.
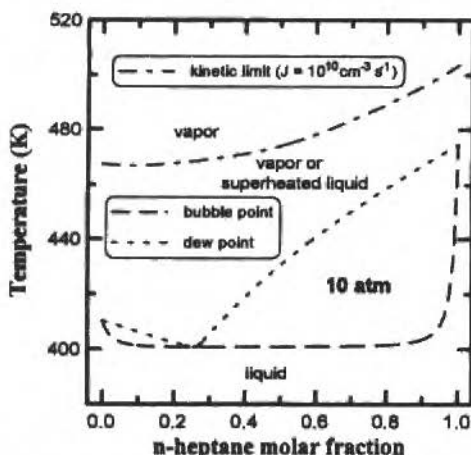
Fig. 1 Phase-equilibrium diagram of the n-heptane-methanol mixture at 10 atm, including the kinetic superheating limit

Figures 2 to 6 show the simulation results for droplet vaporization with radiation vaporization, considering droplet absorptance values of 0, 0.10, 0.25, 0.50. Figure. 2 shows the time variation of the dimensionless droplet radius, $\beta = R/R_o$. It is clear that radiation absorption is quite important in the vaporization process in this case. Although this is not always true, the importance of radiation absorption in droplet vaporization should be verified through the criterion proposed by Lage and Rangel (1993b). Figure. 3 shows the time variation of the droplet surface and center temperatures, $\Theta = (T - T_o)/(T_r - T_o)$ (and the subscript s indicates surface values). For all cases with radiation absorption, the center temperature exceeds the surface temperature after the fast transient surface heating. Thus, the maximum temperature location changes from the surface to the droplet center during the droplet vaporization. This can be easily seen in Fig. 4, where the temperature profile during vaporization is shown for the $\alpha_R = 0.25$ case. This behavior can explain the experimental fact that microexplosion usually begins nearer the surface than the radial position predicted by the conventional diffusive vaporization model (Law, 1978). Figure. 5 shows the mass fraction concentrations, Y, of n-heptane at the center and surface of the droplet. From Figs. 3 and 5, it can be seen that the droplet center, while still at the initial composition, reaches a temperature of about 450K ($\alpha_R = 0.25$ and 0.50). Although this temperature is much higher than the mixture boiling point at Y = 0.5, it is well below the minimum value of the superheating limit. Thus, microexplosion will not occur under these conditions, at least, through homogeneous nucleation.
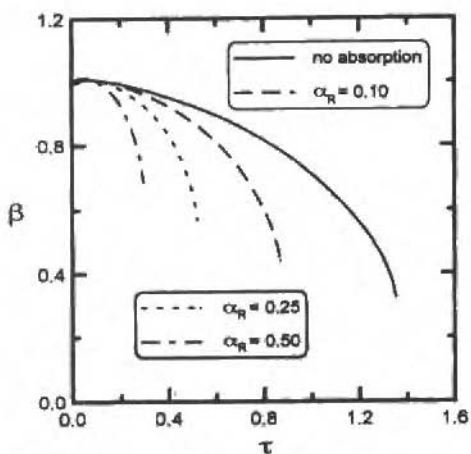
Fig. 2   Vaporization of an n-heptane-methanol droplet: dimensionless radius
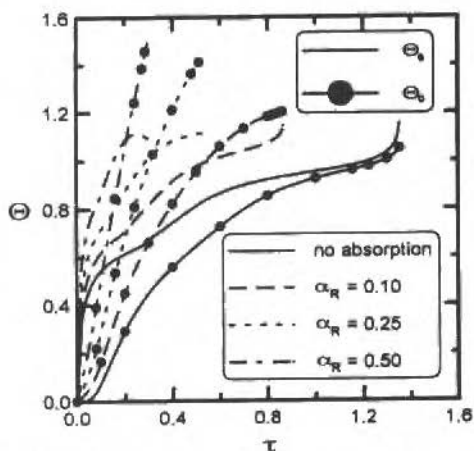

Fig. 3   Vaporization of an n-heptane-methanol droplet: dimensionless center and surface temperature
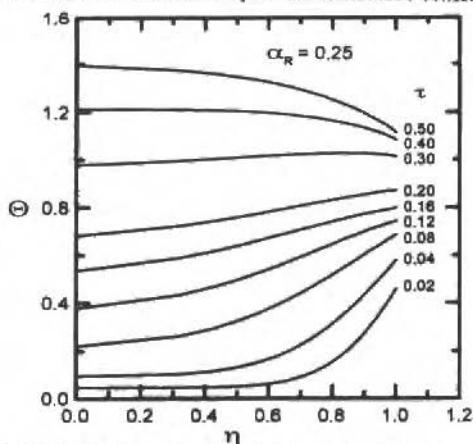

Fig. 4   Vaporization of an n-heptane-methanol droplet: time variation of
the temperature profile $(\eta = r/R(t))$
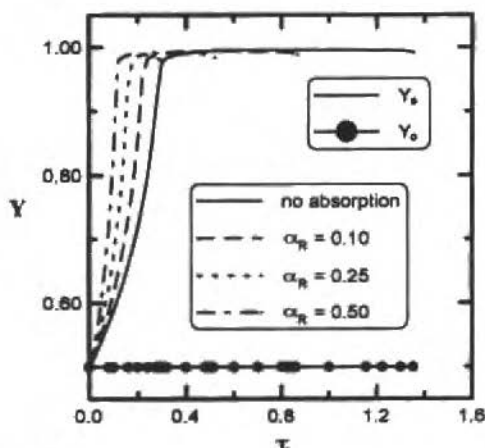
Fig. 5 Vaporization of an n-heptane-methanol droplet: surface and center n-heptane mass fraction

Figure 6 shows the time variation of the droplet vaporization rate, $\dot{m}$. There is a sharp increase of this rate at the end of the droplet lifetime in all cases. This is the beginning of the flash vaporization process (Lage et al., 1993), when the surface temperature reaches its bubble point, which is also larger than the bubble point of all the mixture inside the droplet. Thus, the droplet vaporizes almost instantaneously. This phenomenon is believed to cause the weak sparkle at the end of the combustion of a multicomponent droplet (Lage et al., 1993). It should be noted that an increase in the irradiation intensity or in the droplet absorptance does note necessarily cause microexplosion. This is due to the occurrence of flash vaporization before the droplet interior reaches the superheating temperature. Thus, in order to mocroexplosion occurs, there must exist a sufficiently large volatility differential, even when radiation is absorbed by the droplet. This conclusion is not valid for very large irradiation intensities (lasers), because the droplet surface is not at equilibrium and, thus, the model used is not applicable.
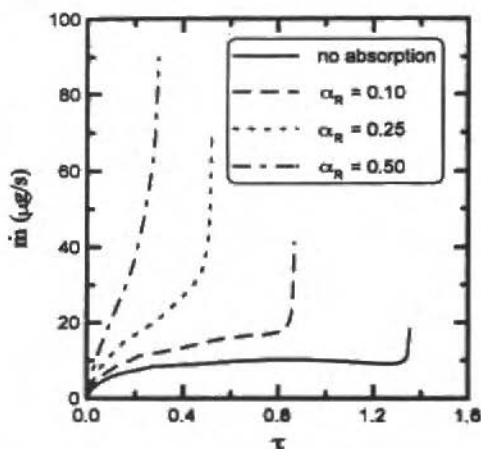
Fig. 6 Vaporization of an n-heptane methanol droplet: vaporization rate

Conclusions

A recently developed liquid vaporization model for multicomponent droplets (Lage et al., 1993) has been used in this work to study the effect of thermal radiation absorption in binary droplet vaporization.

The possible coupling between radiation absorption and droplet microexplosion is also investigated. From this analysis, the following conclusions can be drawn:

- Although the model does not predict a microexplosion of the methanol-heptane droplet, in the conditions analyzed, the temperature increase in the droplet center due to radiation absorption could have led to heterogeneous nucleation in the presence of a nucleation site (a solid impurity). Moreover, in the case of other mixtures with large volatility differentials, the radiation -induced increase of the droplet temperature may reach the superheating limit being decisive for the occurrence of microexplosion through homogeneous nucleation. Thus, the importance of radiation absorption by the vaporizing droplets in a combustion environment should always be assessed, especially for multicomponent droplets.

- The absorption of radiation changes the position of the maximum temperature from the surface to the center of the droplet during vaporization. This may explain the experimental fact that bubble initiation preceding microexplosion usually occurs near the droplet center.

- For the irradiation intensities prevailing in combustion environments, the increase in the radiation absorbed by the droplet does not necessarily promote microexplosion (even for very high irradiation temperature and droplet absortivity). In the cases analyzed, flash vaporization occurs before the droplet reaches the superheating temperature. Thus, even when there is a substantial amount of radiation absorbed by the droplet, a sufficiently large volatility differential is still essential for the occurrence of microexplosion of a multicomponent droplet.

It is believed that the complete understanding of the microexplosion phenomenon necessarily goes through a detailed examination of the non-ideal behavior of the fuel r 'xture and the consideration of thermal radiation heat transfer to the droplet.

Achowledgements

References

Avedisian, C. T., and Glassman, I., 1981, "High Pressure Homogeneous Nucleation of Bubbles within Superheated Binary Liquid Mixture", J. Heat Transfer Vol. 103, pp 272-280.

Biney, P. O., Dong, W. G., and Lienhard, J. H.,1986, "Use of a Cubic Equation to Predict Surface Tension and Spinoidal Limits", J. Heat Transfer, Vol. 108, pp. 405-410.

Bird, R. B., Steward, W. E., and Lightfoot, E. N., 1960, Transport Phenomena. John Wiley & Sons, New York.

Blander, M., Hengstenberg, D., and Katz, J. L., 1971, "Bubble nucleation in n-pentane, n-hexane, n-pentane + hexadecane Mixtures, and Water", J. Phys. Chem. Vol. 75, pp 3613-3618.

Gallant, R. W., 1968, Physical Properties of Hydrocarbons, Vol. 1. Gulf Publishing Company Houston, Texas.

Holden, B. S., and Katz, J. L., 1978, "The Homogeneous Nucleation of Bubbles in Superheated Binary Liquid, Mixtures", AIChE J. Vol. 24 pp. 260-267.

Lage, P. L. C., 1992, "Vaporization of Multicomponent Droplets in Convective and Radiative Fields", (in Portuguese) D. Sc. thesis, COPPE/UFRJ, Rio de Janeiro, Brazil.

Lage, P. L. C., and Rangel , R. H., 1993a, "Total Thermal Radiation Absorption by a Single Spherical Droplet", J. Thermophysics Heat Transfer, Vol. 7, pp. 101-109.

Lage, P. L. C., and Rangel, R. H., 1993b, "Single Droplet Vaporization Including Thermal Radiation Absorption", J. Thermophysics Heat Transfer Vol. 7, pp. 502-509.

Lage, P. L., Rangel, R. H., and Hackenberg, C. M., 1993 "Non-ideal Vaporization of a Dilating Binary Droplet with Variable Properties", Int. J. Heat Mass Transfer, Vol. 36, pp. 3731-3741.,.

Lacheras, J. C. Fernandes-Pello, A. C., and Dryer, F. L.,1980, "Experimental Observations on the Disruptive Combustion of Free Droplets of Multicomponent Fuels", Combust. Sci Technol. Vol. 22, pp. 195-209.

Law, C. K., 1978, "Internal Boiling and Superheating in Vaporizing Multicomponent Droplets", AIChE J., Vol. 24, pp. 626-632.

Lienhard, J. H., and Karimi, A.,1981, "Homogeneous Nucleation and the Spinoidal Line", J. Heat Transfer, Vol. 103, pp. 61-64.

Mackowski, D. W., Altenkirch, R. A., and Mengüç, M. P., 1990, "Internal Absorption Cross Sections in a Stratified Sphere", Appl. Optics, Vol. 29, pp. 1551-1559.

Megaridis, C. M., 1993, "Liquid-Phase Variable Property Effects in Multicomponent Droplet Convective Evaporation", Combust. Sci. Technol., Vol. 92, pp. 291-311.

Melhem, G. A., Saini, R., and Goodwin, B. M.,1989, "A Modified Peng Robinson Equation of State", Fluid Phase Equil., Vol. 47, pp. 189-237.

Ohe, S., 1989, Vapor-Liquid Equilibrium Data, Elsevier, Amsterdam.

Park, B. S., and Armstrong, R. L., 1989, "Laser Droplet Heating: Fast and Slow Heating Regimes", Appl. Optics, Vol. 28, pp. 3671-3680.

Patankar, S. V., 1980, Numerical Heat Transfer and Fluid Flow, McGraw-Hill, New York.

Pinnes, E. L., and Mueller, W. K., 1979, "Homogeneous Vapor Nucleation and Superheat Limits of Liquid Mixtures", J. Heat Transfer, Vol. 101, pp. 617-621.

Reid, R C., Prausnitz, J. M., and Poling, B. E., 1987, The Properties of Gases and Liquids, McGraw-Hill, New York. 4th edition.

Secchi, A. R., Morari, M., and Biscaia Jr., E. C., 1991, "DAWRS: A Differential-Algebraic System Solver by the Waveform Relaxation Method", in Sixth Distributed Memory Computing Conference (DMCC6), Portland, Oregon, Apr.

Sripov, V. P., 1974, Metastable Liquids, John Wiley & Sons, New York.

Tuntomo, A., 1990, "Transport Phenomena in a Small Particle with Internal Radiant Absorption", Ph. D. thesis, university of California at Berkeley.

Vargaftik, N. B., 1975, Tables on the Thermophysical Properties of Liquids and Gases, Hemisphere, New York 2nd edition.

Wang, C.H., and Law, C.K., "Microexplosion of Fuel Droplet Under High Pressure", Combust. Flame Vol., 59, pp. 53-62, 1985.

Wang, C. H., Liu, X. Q., and Law, C K., 1984, "Combustion and Microexplosion of Freely Falling Multicomponent Droplets", Combust. Flame, Vol. 56, pp. 175-197.

Yang, J. C., Jackson, G. S., And Avedisian, C. T., 1990, "Combustion of Unsupported Methanol/Dodecanal Mixture Droplets at Low Gravity", Twenty-Third Symp. (Int.) Combustion, The Combustion, pp. 1619-1625.

Adiabatic Evaporation Waves

J. R. Simões Moreira*
J. E. Shepherd
Graduate Aeronautical Laboratory, California Institute of Technology, Pasadena, CA
*Also Escola Politécnica da USP, Sao Paulo, SP

Abstract

Experimental results on adiabatic evaporation of superheated dodecane are presented. Saturated dodecane was suddenly exposed to a low pressure environment by rupturing a diaphragm. An evaporation wave started at the liquid free surface and propagated into the metastable liquid. Pressure and temperature traces as well as velocity of propagation of the disturbance are reported for several experimental conditions.
Keywords: Adiabatic Evaporation, Superheated Dodecane

Introduction

When a pressurized liquid is abruptly exposed to a low pressure environment, the fluid pressure may be reduced far below saturation without immediate boiling. After a brief time delay, the depressurization process is followed by rapid evaporation of the metastable liquid. The explosive character of this process has been the cause of some industrial accidents (Reid, 1976 and 1983). Under certain conditions, the liquid will evaporate in a wave-like process, that is, an interface or wave moves into the undisturbed metastable liquid and a two-phase mixture is observed downstream of the wave front. This type of liquid-vapor phase transition has been observed in our experiments and by others (Tener, 1962, Grolmes and Fauske, 1974, Chaves in Thompson et al. 1987; and Hill, 1991). This phenomenon seems to be dependent on several factors, such as the nature of the substance, degree of superheat, condition of the container walls and depressurization time scale. Highly superheated liquids (near or at the spinodal) can show explosive features and Shepherd (1981) has shown that an evaporation wave process can occur on a smaller scale within superheated droplets (see also Shepherd and Sturtevant, 1982). Moderate superheating, appreciably less than the superheat limit, can give rise either to evaporation waves, as analyzed in this paper, or to evaporation due to heterogeneous nucleation at the container walls. Finally, at very low superheats, ordinary boiling occurs.

This paper reports experiments carried out with saturated dodecane at temperatures ranging from 180°C to 300°C. As discussed in our previous work (Simões Moreira et al., 1993), the choice of dodecane is related to the theoretical possibility of obtaining a complete evaporation wave in one-dimensional experiments. This is because of the high specific heat of a substance such as dodecane, which displays retrograde behavior. A detailed discussion is given in Simões Moreira (1994). Evaporation waves are essentially adiabatic phase transition processes, and the latent heat is supplied from the energy stored in the metastable liquid. Other terms used to designate this phenomenon are boiling discontinuities or boiling shocks (Labuntsov and Avdeev, 1981 and 1982), boiling front propagation, BFP (Das et al., 1987) or flash boiling by others. Applications of this phenomenon include fuel injection systems, loss-of-coolant accidents in nuclear plants, power industry and chemical plants as well as any other systems where rapid decompression can occur.

Experimental Setup

A schematic diagram of our facility can be seen in Fig. 1. The test liquid was contained in a glass tube, whose dimensions were 340 mm long by 15 mm diam. Glass was chosen because its surface was smooth enough to suppress undesirable heterogeneous nucleation and it also it also made photographic documentation of the phenomenon possible. Circulation of hot air in a square glass jacket partially enclosing the cell was used to heat the system to the desired temperature. The source of hot air was two "heat guns", modified to have the power input controlled by independent rheostats. To ensure the uniformity of the initial temperature, a thermocouple was traversed within the test cell, and the heat supply was adjusted as necessary. A diaphragm (made out of kapton in most experiments and aluminum in a few cases) closed the top part of the cell and served to isolate the test liquid from a low-

pressure chamber. Each experiment consisted in discharging about 50 cm^3 of liquid dodecane. The experiment began by piercing the diaphragm, which quickly exposed the slightly compressed liquid to the low pressure reservoir (0.227m^3). This was accomplished by using an arrow with sharp knife blades (four) driven by a compressed air piston actuated by a solenoid valve. The blades were at a shallow angle to the horizontal (5°) so that the total piercing time of the diaphragm was in the order of a few milliseconds. Substantial efforts were made to suppress nucleation at the bottom of the cell. The solution consisted in cooling the bottom portion of the test cell and allowing it to protrude below the heated section.

Pressure transducers were located at the bottom of the cell and near the cell exit. The bottom transducer was mounted flush with the flange. The exit transducer was mounted remotely in a small aluminum block and water cooled to prevent thermal damage. The exit pressure signal was transmitted through a small steel tube from the test cell to the pressure transducer. Exit temperatures were abtained using a T-type thermocouple with a bead of diameter 0.6 mm. Signals were amplified and then recorded using a personal computer. We obtained simultaneous still photographs using two cameras and a short-duration (0.5 µs) light source. One camera imaged a front view of the test cell and the other was oriented at 30° to the evaporation wave plane. The light triggering signal came from a photosensor that was illuminated by a laser beam passing through the test cell. As soon as the evaporation wave passed by, it blocked off the beam causing the photosensor circuit to generate an electrical pulse, which then triggered the light source. Motion pictures with a framing rate of 3000 s^{-1} were also obtained.
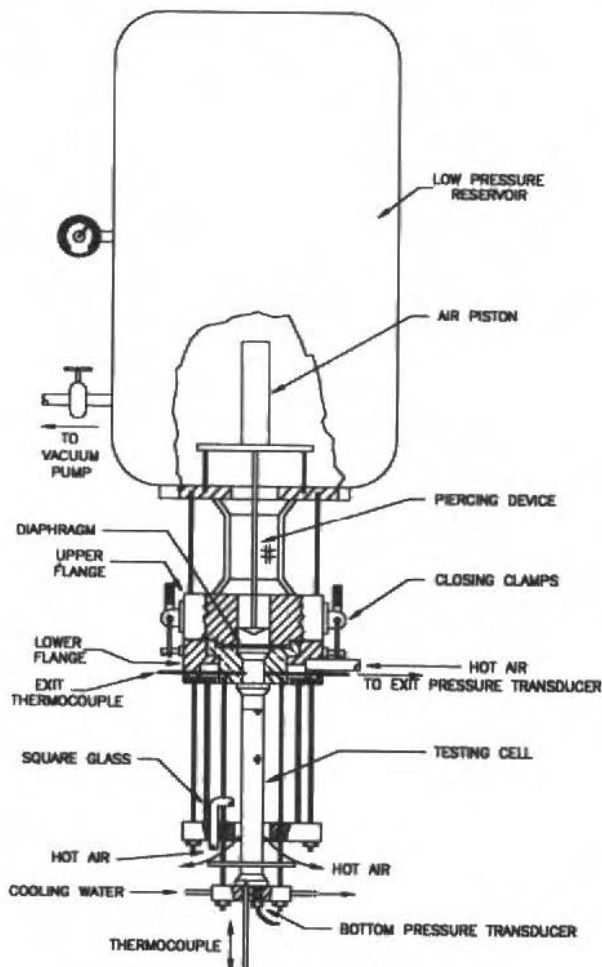
Fig. 1 Diagram of the experimental setup

These films revealed details of the development of the evaporation wave and enabled accurate measurements of the wave speed.

A typical run started by degassing the fluid at room temperature. Then the test cell was filled, the diaphragm installed and a second low-pressure degassing process would take place while the system was being heated up. After boiling for some time, then the glass cell was pressurized with cover gas (N_2). Pressure was controlled inside the test cell so that the liquid was slightly above the vapor pressure. The reservoir was evacuated and brought up to the desired pressure with N_2. Once the test condition was reached the photographic system (high-speed motion or still pictures) and the data acquisition were set up. The triggering signal for the data acquisition was either from the high-speed camera, or from the diaphragm piercing system. The total data acquisition time was in the range of 200-500 ms, depending on the experiment and the sampling rate (of the order of 1 KHz).More details on the experimental setup can be found in Simões Moreira (1994).

Results and Analysis

Development of the metastable state. Two events on different time scales occurred after the diaphragm burst. At the very beginning, the process of depressurization occurred via the propagation of rarefaction waves in the vapor above and within the liquid. Several reflections might occur over a period of milliseconds before a uniform pressure was established in the liquid. It is reasonable to assume that this part of the process occurred isentropically. The metastable liquid temperature changes could not be measured and were estimated to be less than 0.01 °C during decompression. Simultaneously, the evaporation wave started at the initial liquid free surface. It appeared that the evaporation wave dynamics dictated the degree of metastablility the fluid reached and the metastable pressure as well. In other words, if no evaporation occurred at all, rarefaction and compression acoustic waves would propagate in the liquid until the liquid pressure equaled the reservoir pressure. On the other hand, if there was an evaporation front, the pressure jump across the front, and at the exit of the test cell determined the maximum degree of superheat in the liquid.

Development and propagation of the wave. We carried out one set of experiments at constant temperature (230°C) and variable reservoir or back pressure, P_R. The general observations are as follow:

- $1,2 \leq P_R \leq 1,3$ bar. At low superheats, i. e., back pressures close to the saturation pressure (1.387 bar), a wave did not start. Nucleation started at the interface of the free surface and the glass tube and then the nucleation sites moved randomly down the tube wall.

- $0,7 \leq P_R \leq 1,1$ bar. As the back pressure was decreased, an evaporation wave appeared to start, but nucleation usually occurred somewhere upstream in the liquid. Usually, a single slug-flow-type bubble grew until it filled the tube and expelled the liquid above it. At $P_R = 0.7$ bar, it was possible to observe a stable evaporation wave initially but nucleation disrupted the process eventually.

- $P_R \leq 0,6$ bar Lower back pressure resulted in the consistent formation of evaporation. Waves started promptly and propagated with a characteristic velocity. No nucleation upstream was observed.

- $P_R \leq 0,3$ bar. Beyond a certain point, the exit pressure would be independent of the reservoir pressure. The evaporation wave properties were then insensitive to the back pressure. The evaporation wave properties were then insensitive to the back pressure. We believe that this was due to the two-phase flow reaching a choking condition.

Table 1 summarizes the experimental observations: P_R is the reservoir pressure; P_E is exit pressure; P_B is the pressure at the bottom of the test cell. Wave velocities were computed by analyzing the recorded video images from a CCD camera used for this set of experiments. The saturation pressure of dodecane at 230°C is 1.387 bar.

The trend of these results is in agreement with the earlier experiments of Grolmes and Fauske (1974) and Hill (1991). There was a noticeable threshold, at which an evaporation wave could be formed and sustained. It is interesting to note that at higher degrees of superheat, no nucleation in the upstream metastable liquid was observed during the tests. That seems puzzling, since at very low

degrees of superheat (P_R near the saturation pressure) nucleation occurred consistently. This is simply due to the time required for nucleation to occur. At low degrees of superheat, the metastable fluid remained in the test cell for a long period of time, enabling heterogeneous nucleation to occur. On the other hand, if an evaporation wave promptly started, the metastable liquid remained in the test cell for a shorter period of time and heterogeneous nucleation upstream of the wave did not play any role.

Table 1   Back pressure variation experiment (T=230 °C - Psat = 1.387 bar)

P (bar)	P (bar)	P (bar)	Vel (cm/s)	Observations
1.3-0.8	1.3-0.8	1.3-0.8	-	Train of bubbles/unsta ble wave
0.7	0.700	0.702	8.1	ev. wave + slug flow bubble
0.6	0.62	0.66	29.0	threshold for evap. wave
0.5	0.54	0.62	39.4	evap. wave
0.4	0.41	0.61	45.3	evap. wave
0.3	0.37	0.60	47.2	evap. wave
0.2	0.46	0.61	45.7	evap. wave
0.1	0.44	0.61	46.5	evap. wave
0.0	0.37	0.59	47.2	evap. wave

Pressure and Temperature Traces: Figure. 2 presents typical pressure and temperature traces obtained in our experiments. The ones show nare for a 230°C temperature test. Notice that the signals are steady after the diaphragm rupture event, which is indicated by an arrow. Is most experiments the signals dropped sharply after diaphragm burst, however in some cases the exit pressure drop was slower due to evaporation of condensed liquid in the line. The bottom pressure signal was low-pass filtered (f_c = 100 Hz) to reduce the effect of the vibration caused by the impact of the air piston on the structure. The temperature records showed that the exit temperature (185C) was very near the saturation temperature corresponding to the two-phase mixture pressure (T_{sat} = 177°C).
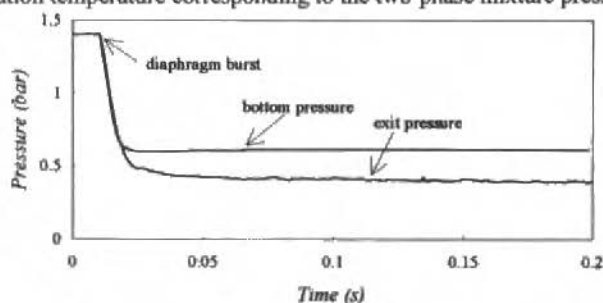
(a)
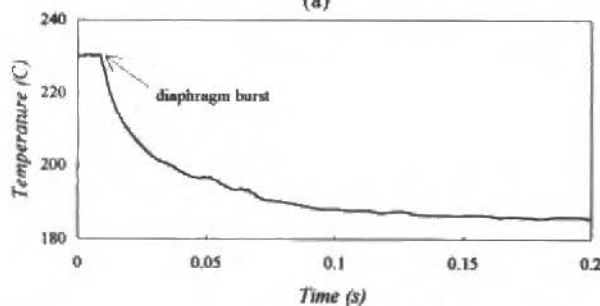
(b)

Fig. 2   Typical pressure (a) and temperature (b) records obtained in our experiments. T_{test} = 230°C; P_R = 1 mbar

Evaporation wave in progress: Figure. 3a shows an oblique view (at 30°) photograph of an evaporation wave in progress in metastable liquid at 216°C. A front view of another wave at 230°C can be seen in Fig. 3b. The wave moves from top to bottom. The evaporation front is highly disturbed. The nature of disturbance in not clear be described as either a layer of vapor bubbles or a scalloped surface. Fluctuations of this front are obvious in the high-speed motion pictures. If one assigns an average plane to the front, a normal vector to this plane fluctuates about the axial direction. In our experiments, it was always possible to identify an average propagation velocity (Fig. 4). A relaxation zone was visible in some experiments similar to the darker zone behind the wave in Fig. 3b, but not in all of them. We interpret these darker regions as being finer droplets that were scattering the rear illumination. Analyses of the motion pictures revealed that sometimes jet-like structures of very fine droplets would come out the wave zone at high speed. The downstream region can be characterized by there distinct parts. (1) - streaks of low speed liquid flowing along the cell walls.(2) - vapor flowing in the core zone. (3) - fine droplets flowing in the high speed core zone In the terminology of two-phase flows, the closest classification would be annular flow with entrainment.

two-phase region

(a)

evaporation wave

metastable liquid

two-phase region

(b)

evaporation wave

metastable liquid
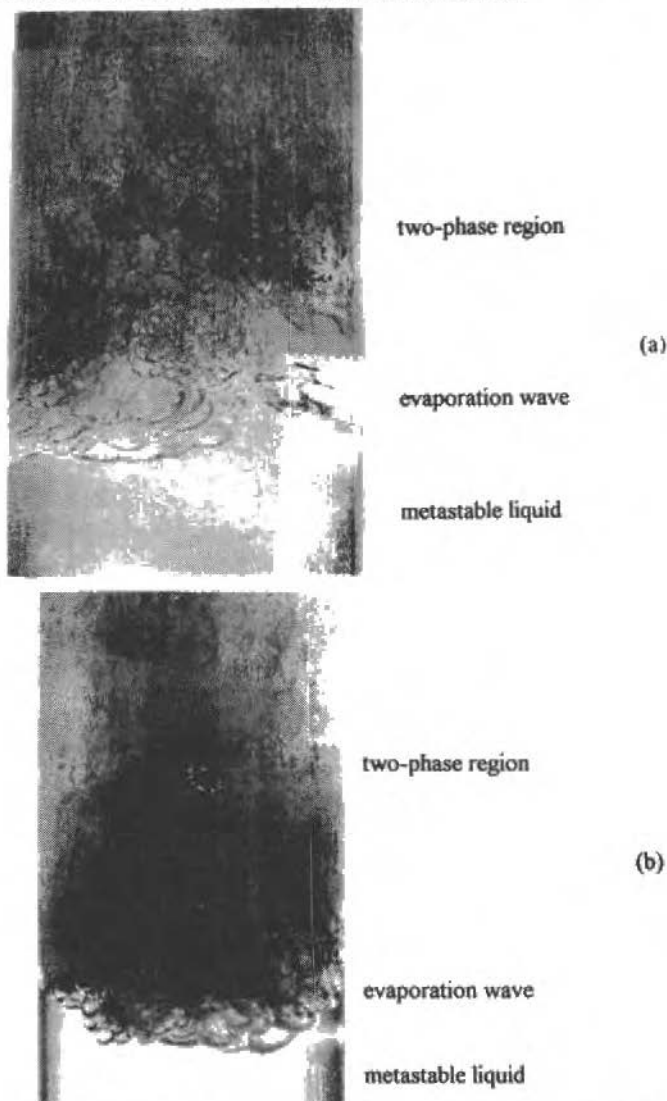
Fig. 3   Photographs of evaporation waves in progress (a) - 30°C view, T_{test} = 216°C. (b) - front view; T_{test} = 230° P_R = 1 mbar

Summary of experimental results: Table 2 presents a summary of our experimental results. The temperature range was from 180°C to 300°C at nearly 20°C steps. The saturation properties were calculated using the Lee-Kesler (1975) equation-of-state (see details in Simões Moreira, 1994). Wave speeds were obtained from high-speed motion pictures using the method of least squares to determine wave speed from position vs. time data. The time reference for the motion pictures was obtained from 10 ms timing light marks on the film. The results are shown on Fig. 4.

P_B and P_E represent an average of the pressure signals over the time of interest. T_E was taken as the exit temperature at the end of the steady phase of the wave. The last values for T_E are missing because no steady temperature was reached in these two experiments. Even at the highest test temperature of 300°C, the downstream state was a liquid vapor mixture. We anticipated from our previous study (Simões Moreira et al, 1993) that a single phase (vapor) downstream state might be reached under these conditions, but we were not able to observe this since a sufficiently low pressure was not obtained in the superheated liquid. We estimate that the highest quality (mass fraction of vapor) achieved in these experiments was above 90% at an initial temperature of 300°C.

Table. 2 Summary of experimental results.

T_{test} (°C)	P_{sat} (bar)	P_B (bar)	P_E (bar	T_E (°C)	Vel. (cm/s)
180	0.39	0.24	0.18	155	25.3
200	0.67	0.33	0.22	165	30.9
216	1.00	0.44	0.28	176	39.0
230	1.39	0.59	0.37	186	47.2
250	2.11	0.83	0.52	200	64.8
270	3.11	1.19	0.73	210	83.7
290	4.44	1.91	1.16	-	138.1
300	5.25	2.12	1.32	-	157.8
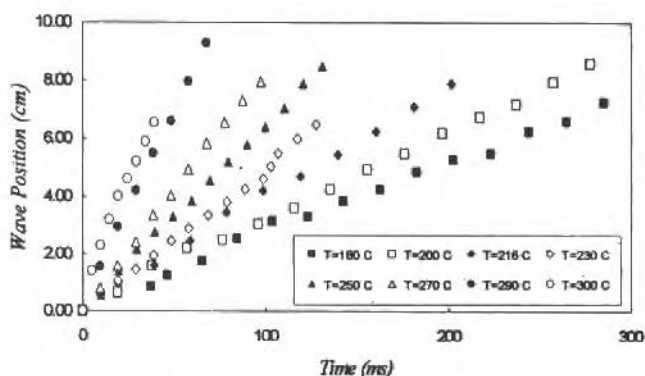
Fig. 4   Wave position as function of time (from high-speed motion pictures)

Conclusions

We have observed adiabatic evaporation waves in dodecane over a wide range of temperatures. The experiments agreed with the results of previous authors in the sense that the wave behaved as a front moving at nearly constant speed into the metastable liquid. Still and motion pictures showed that the front was a highly disturbed zone of transition from liquid to two-phase mixture. The propagation speed depended in a systematic fashion on the metastable liquid temperature and the degree of metastabiliIy. In all cases, the flow downstream of the evaporation wave was a two-phase mixture. A model of evaporation waves has been previously developed (Shepherd et al., 1990, Simões Moreira et al., 1993 and Simões Moreira, 1994) and can be applied to the problem. A future

publication will analyse in depth these results, including a modification of the simple evaporation wave theory to include a more realistic treatment of the two-phase flow downstream of the wave, including slip between phases.

Acknowledgments

References

Das, P. K., Bhat, G. S., and Arakeri, V. H., 1987, "Investigations on the Propagation of Rapid Depressurization of Subcooled Liquid" International Journal of Heat and Mass Transfer, Vol. 6, pp. 975-84.

Grolmes, M. A., and Fauske, H. K., 1974, "Axial Propagation of Free Surface Boiling into Superheated Liquids in Vertical Tubes"-5th International Heat Transfer Conf. Tokyo, Vol,. IV, pp. 30-34.

Hill, L. G., 1991" An Experimental Study of Evaporation Waves in a Superheated liquid - PhD Thesis, California Institute of Technology.

Labuntsov, D. A., and Avdeev, A. A.,1981, "Theory of Boiling Discontinuity", Teplofizika Vysokikh Temperatur, Vol., 19, N°. 3, pp. 552-56.

Labuntsov, D. A., and Avdeev, A. A., 1982, "Mechanism of Flow Blockage Involving Shock Boiling of Liquid", Teplofizika Vysokikh Temperatur, Vol. 20, No. 1, pp 88-95.

Lee, B. I., and Kesler, M. G., 1975, "A Generalized Thermodynamic Correlation Based on Three-Parameter Corresponding States", AIChE Journal, Vol. 21, No. 3, pp. 510-27.

Reid, R. C., 1976, "Superheated Liquids", American Scientist, Vol. 64, pp. 146-56.

Reid, R. C.,1983, "Rapid Phase Transition from Liquid to Vapor", Advances in Chemical Engineering, Vol. 12, pp. 105-208.

Shepherd, J. E., 1981, "Dynamics of Vapor Explosions: Rapid Evaporation and Instability of Droplets Exploding at the Superheat Limit", PhD Thesis, California Institute of Technology.

Shepherd, J. E., and Sturtevant, B., 1982, "Rapid Evaporation at the Superheat Limit", Journal of Fluid Mechanics, Vol. 121, pp. 379-402.

Shepherd, J. E., McCahan. S., and Cho, J., 1990, "Evaporation Wave Model for Superheated Liquids", Adiabatic Waves in Liquid-Vapor System, G. E. Meyer and P. A. Thompson eds., Springer-Verlag, pp. 3-12.

Simões Moreira, J. R., McCahan. S., and Shepherd, J. E., 1993, "Complete Evaporation Waves" ASME Fluid Engineering Conference, paper # 93-FE-7, Washington, D. C., June 20-24.

Simões Moreira, J. R., 1994, Adiabatic Evaporation Waves, PhD Thesis, Rensselaer Polytechnic Institute, NY.

Terner, E., 1962, "Shock-Tube Experiments Involving Phase Changes", Industrial & Engineering Chemistry Process Design and Development, Vol. 1, No. 1.

Thompson, P. A., Chaves, H., Meyer, G. E., Kim. Y.G., and Speckmann, H. D., 1987, "Wave Splitting in a Fluid of Large Heat Capacity", Journal of Fluid Mechanics, Vol. 185, pp. 385-414.

Abstracts

The roll-up process of vortex wakes generated by wings (with a straight trailing edge) is computed, with the aid of two and three-dimensional vortex-in-cell methods. Results and computational effort of the two approaches are compared, and the accuracy of traditional assumptions made to allow the solution of the problem in the two-dimensional domain is investigated.
Keywords: Wing Vortex Roll-Up, Vortex-in-Cell Method

There has been carried out a work consisting in the application of the System Theory and the Exergy Analysis Method, including Thermoeconomic Techniques, to the industrial processes in the Basque Country (Spain). In this analysis, the irreversibilities in each basic operation have been quantified and the energetic and exergetic efficiencies have been evaluated. The exergetic costs have been also calculated for every energy and material flow, as well as their corresponding economic costs. Besides, there is intended to value the effects on the consumption of energy and materials when new technologies are introduced.
The basic aims of this study are, on the one hand, to develop a system of strategic planning in the field of energetic technologies and, on the other hand, to define a strategy plan for equipments, processes, technologies and areas (industrial, services and residential sectors), consuming energy and/or materials, referred to the Basque Country as a framework. The above-mentioned study has been applied, as an example, to the green glass manufacturing area.
Keywords: Energetic Analysis, Thermoeconomic Analysis, Industrial Processes, Green Glass Manufacturing

The first attempt to apply a previously developed computer program to simulate a pressurized fluidized-bed gasifier for wood is described. The experimental tests were reported by the Institute of Gas Technology (U.S.A.), which developed the process and the equipment. Among the overall and internal characteristics of the equipment operation obtained by simulation, the paper illustrates various aspects of temperature, composition, particle size distribution profiles throughout the bed and freeboard. The average deviations between these values are relatively small and allow the use of the program to call attention over possible improvements in the process.
Keywords:Fluidized-Bed Raactors , Biomass, Pressurized Gasification

A computational program to evaluate nonequilibrium reactive flows of combustion products through convergent-divergent nozzle is developed. The basic assumptions are: two reactive systems [(H_2 and F_2) and (H_2 and O_2)] and bidimensional flow. The results compare well to theoretical and experimental data from the literature.
Keywords: Nonequilibrium Reactive Flows, Convergent-Divergent Nozzles, Method of Characteristics.

The influence of radiative changes between the flame and the forest material, at ground level, is given by integral models deriving from the radiosity balance between an emitting volume and the receiving surface. Thus, the heat transfer can be described by a convolution integral where the flame influence is quantified by a Green function that describes the heat exchange decay by the distance from the flame. From this approach, the formulation of an

integro-differential model is proposed and numerically implemented by a Monte Carlo Integration / Explicit Euler propagation coupled method.

Keywords: Forest Fires, Radiative Heat Transfer, Monte Carlo Integration

Orlande, H. R. B., and Ozisik, M. N., 1994, "Inverse Heat Conduction Problem for the Estimation of the Temperature Dependence of Thermal Conductivity", RBCM - J. of the Braz. Soc. Mechanical Sciences, Vol. 16, no.4, pp. 400-406.

In this paper we use the Conjugate Gradient Method with Adjoint Equation in order to estimate the temperature dependence of thermal conductivity. The accuracy of this method of inverse analysis is verified by using simulated measurements as the input data for the inverse problem. Functional forms containing sharp corners and discontinuities are generally very difficult to recover by an inverse analysis. The present approach is capable of handling such situations quite readily and accurately.

Keywords: Thermal Conductivity, Inverse Heat Conduction, Temperature Dependence

Pires, L. F. G., and Nieckele, A. O., 1994, "Hidrodynamics in Tubes with Curvilinear Obstructions", RBCM - J. of the Braz. Soc. Mechanical Sciences, Vol. 16, no.4, pp. 407-414.

A numerical study of the flow field in ducts with curvilinear obstruction was performed. A wide range of Reynolds was investigated. Velocity and pressure distribution were obtained by a finite volume method with non-orthogonal coordinate system. Comparision with available numerical and experimental results showed good agreement.

Keywords: Ducts, Curvilinear Obstruction, Finite Volume Method, Non-Orthogonal Coordinate System, Flow Field.

Maliska, C.R., and Maliska Jr., C.R., 1994, "A Finite Volume Method Using Voronoi Grids for the Solution of Miscible Displacement in Porous Media", RBCM - J. of the Braz. Soc. Mechanical Sciences, Vol. 16, no.4, pp. 415-422.

The present work describes a numerical methodology for the solution of miscible displacement in porous media using unstructured Voronoi discretization. The Voronoi diagrams are an attractive alternative for approximating flow problems due to its construction, which forces grid points to be aligned with the normal of the control volume surfaces. The control volume approach is used and an hybrid scheme is employed as the interpolation function for the solution of a tracer injection in a single-phase flow in a five-spot arrangement. The numerical results are compared with the ones obtained with boundary-fitted grids and experimentally.

Keywords: Miscible Displacement, Porous Media, Finite Volume Method, Voronoi Grids

Cunha, A. R., Maliska, C. R., Silva, A. F. C., and Livramento, M. A., 1994, "Two-Dimensional Two-Phase Petroleum Reservoir Simulation Using Boundary-Fitted Grids", RBCM - J. of the Braz. Soc. Mechanical Sciences, Vol. 16, no.4, pp. 423-429.

The present work introduces a numerical method, using boundary-fitted grids, for simulating petroleum reservoirs. Boundary-fitted meshes have the capability of conforming the irregular boundary of the reservoir, allowing better application of boundary conditions and facilitating the specification of geological faults. To assess the methodology, the well known five-spot problem is used, where comparisons using curvilinear, cartesian diagonal and parallel grids are done. To demonstrate the ability of the model, a reservoir of irregular shape, with 2 injection and 6 production wells, is simulated.

Keywords: Petroleum Reservoirs Simulation, Boundary-Fitted Grids

Peixoto, R. A., Hrnak, P., Johnson, F., and Meyers, John, 1994, "An Experimental Analysis of Capillary Tube-Suction Line with HFC-134a", RBCM - J. of the Braz. Soc. Mechanical Sciences, Vol. 16, no.4, pp. 430-436 (In Portuguese).

Expansion devices are one of the four major components of vapor compression refrigeration systems and small systems use capillary tube as this device. Today, a capillary tube-suction line heat exchanger geometry (ct-sl hx) is used in almost all household refrigerators. Capillary tube-suction line heat exchangers were tested in this work with refrigerant HFC-134a that has emerged as the primary condidate for CFC-12 replacing.

Keywords: Capillary Tube-Suction Line Heat Exchanger, Refrigerant HFC-134a

Lage, P. L. C., Hackenberg, C. M., and Rangel, R. H., 1994, "Vaporization of Dilating Non-Ideal Binary Droplets with Radiation Absorption", BCM - J. of the Braz. Soc. Mechanical Sciences, Vol. 16, no.4, pp. 437-444.

A recently developed liquid vaporization model for multicomponent droplets has been enhanced in order to study the effect of thermal radiation absorption in binary droplet vaporization. The possible coupling between radiation absorption and droplet microexplosion is also investigated. The results show that radiation absorption can influence droplet vaporization in combustion environments and might explain some experimental findings on microexplosion phenomena. The vaporization model including radiantion absorption also predicts the experimentally-observed sparkle at the end of droplet combustion (flash vaporization).

Keywords: Vaporization, Multicomponent Droplets, Droplet Microexplosion, Thermal Radiation Absorption

Simões Moreira, J. R. and Shepherd J. E., 1994, "Adiabatic Evaporation Waves", RBCM - J. of the Braz. Soc. Mechanical Sciences, Vol. 16, no.4, pp. 445-451.

Experimental results on adiabatic evaporation of superheated dodecane are presented. Saturated dodecane was suddenly exposed to a low pressure environment by rupturing a diaphragm. An evaporation wave started at the liquid free surface and propagated into the metastable liquid. Pressure and temperature traces as well as velocity of propagation of the disturbance are reported for several experimental conditions.

Keywords: Adiabatic Evaporation, Superheated Dodecane

ENCIT 94 - 5ᵀᴴ BRAZILIAN THERMAL SCIENCES MEETING ISSUE
São Paulo, SP - December 7-9, 1994